

SUB-MEV GAMMA-RAY STUDY OF
ANOMALOUS X-RAY PULSAR
1E 1547.0–5408 WITH *Suzaku*

Tetsuya Yasuda

Department of Physics, Graduate School of Science, Saitama University
Shimo-Ohkubo, Sakura-ku, Saitama, 338-0870, Japan
yasuda@heal.phy.saitama-u.ac.jp

Thesis submitted to the Department of Physics,
Graduate School of Science and Engineering, Saitama University
in partial fulfillment of the requirements
for the degree of Doctor of Philosophy in physics

March 9, 2015

Contents

1	Introduction	11
2	Review	13
2.1	Physical Parameters in Rotation Powered Pulsars	14
2.2	Overview of AXPs and SGRs	17
2.3	Persistent X-ray Emission from AXPs and SGRs	19
2.3.1	Time Variation	19
2.3.2	Energy Spectra	20
2.4	Burst Emission from AXPs and SGRs	22
2.4.1	Giant Flare	23
2.4.2	Intermediate Flare	24
2.4.3	Short burst	25
2.5	Magnetars Hypothesis	27
2.5.1	Magnetized Neutron Star Model	28
2.5.2	Interesting Phenomena in Strong Magnetic Field	29
2.5.3	Alternative Models for AXPs and SGRs	30
2.6	Target Object; AXP 1E 1547.0–5408	30
2.6.1	Overview of AXP 1E 1547.0–5408	30
2.6.2	Activity on 2008 October and 2009 January	31
2.7	Scope of Present Thesis	32
3	Instrumentation	33
3.1	<i>Suzaku</i> Wide-band All-sky Monitor	33
3.1.1	Overview	33

3.1.2	Electronics for WAM	36
3.1.3	Energy Calibreation	38
3.1.4	Generating Energy Response Matrix	39
3.2	Other Instruments	39
3.2.1	<i>Swift</i> Burst Alert Telescope	39
3.2.2	<i>Swift</i> X-ray Telescope	40
3.2.3	<i>Fermi</i> Gamma-ray Burst Monitor	42
3.2.4	<i>INTEGRAL</i> Anti-Coincidence System	43
4	Observation and Data Reductioin	45
4.1	Observation of Bursts from AXP 1E 1547.0–5408 with WAM	45
4.2	Observations with Other Instruments	48
4.2.1	Observation with <i>Swift</i> BAT and XRT	48
4.2.2	Observation with <i>Fermi</i> GBM	50
4.2.3	Observation with <i>INTEGRAL</i> ACS	50
5	Analysis and Results	55
5.1	Temporal Analysis	56
5.1.1	Burst Detections with the WAM	56
5.1.2	Search for WAM Bursts Simultaneously Detected with Other Instru- ments	56
5.1.3	Estimation of Incident Angles of Bursts by the WAM	57
5.1.4	Correlation Searches from WAM Selected Bursts	61
5.2	Preparations for Spectral Analysis	64
5.2.1	Response Matrixes Generation	64
5.2.2	Data Selection	65
5.2.3	Development of Pile-up Simulator	65
5.3	Spectral Analysis	67
5.3.1	Individual Spectral Fitting	67
5.3.2	Results on Bright Bursts	70
	06:45:13 burst	71
	06:48:04 burst	71

<i>CONTENTS</i>	5
6 Discussion	75
6.1 Summary of Observational Results	75
6.2 Burst Statistics, Intensity Distribution	76
6.3 Burst Energetics	77
6.3.1 Estimation of Entire Radiated Energy in Sub-MeV Range	77
6.3.2 Comparison of the BB Parameters with Other Observations	78
6.3.3 Estimation of Surface Magnetic Field Strength to Enclose the BB Plasma	78
6.3.4 Fluence for the Light Echoes	80
6.4 Origin of the Hard X-ray Component	81
6.5 Possible Interpretation of the Radiation Origin	84
7 Conclusion	87
A Detail of Pile-up Simulator Performance	95
A.1 Demonstration of Pile-up Simulator	95
A.2 Verification with Bright Solar Flares	97
B All Detected Events	99
C Spectral Parameters	113

List of Figures

2.1	$P-\dot{P}$ diagram.	16
2.2	Relation of calculated spin down luminosity versus observed X-ray luminosity diagram.	18
2.3	Long-term X-ray light curve of AXP 1E 1547.0–5408.	19
2.4	Phase-dependent spectral feature and a sample of phase resolved spectrum (from Tiengo et al. (2013))	21
2.5	<i>Suzaku</i> view of eight AXPs and SGRs $\nu F\nu$ spectra from Enoto et al. (2010b) (Rea & Esposito 2011)).	22
2.6	Characteristic energy spectra of high-energy burst phenomena (Woods & Thompson 2006).	23
2.7	<i>Swift</i> -BAT light curve of 2004 December 27 giant flare from SGR 1806–20	24
2.8	Light curves of intermediate flares.	26
2.9	<i>Suzaku</i> spectra of the summed 31 short bursts from SGR 0501+4516, fitted jointly with a 2BB+PL model (Nakagawa et al. 2011).	26
2.10	Twisted magnetosphere and a pure dipole (Thompson et al. 2002)	28
2.11	Stable twisted-toroid field in a star (Braithwaite 2009)	29
3.1	Schematic view of <i>Suzaku</i> satellite and Geant4 3-D geometry.	34
3.2	Schematic view of the HXD detector.	35
3.3	Definition of incident angle of photons to the WAM.	35
3.4	Light curves of one of calm days of the WAM on 2009 January 20.	37
3.5	Overall signal-processing scheme of one WAM analog electronics unit taken from Yamaoka et al. (2009).	38
4.1	<i>Suzaku</i> /WAM-0 TRN light curves after dead-time correction on 2009 January 22.	46

4.2	Comparison of light curves of five instruments.	47
4.3	<i>Suzaku</i> WAM-0 BST light curves obtained in 2009 January 22.	49
5.1	Count rate histograms of the BAT, the XRT and the ACS.	58
5.2	Histogram of WAM-0/WAM-1 count rate ratio.	60
5.3	Time history of detected events by WAM-0	60
5.4	WAM-0 count rate histograms of detected events in 70–160 keV and in 160–330 keV.	61
5.5	Histograms and scatter plot of waiting time of detected events in 70–160 keV and in 160–330 keV.	62
5.6	Scatter diagrams of WAM-0 count rate.	63
5.7	Scatter plot between waiting time and hardness ration.	64
5.8	Summary of the pile-up simulator.	66
5.9	Definition of pulse shape in the pile-up simulator.	67
5.10	Scatter plot between the emission area and the temperature of acceptable BB fitting.	68
5.11	Sample spectra and acceptable models of the BB, the BB+OTTB, and the BB+PLE.	69
5.12	Sample $\nu F\nu$ spectrum of burst ID 424 with the best-fit BB+PLE model.	70
5.13	Temperature relation between the BB and the OTTB components in the BB+OTTB fitting.	71
5.14	Scatter plots of yielded parameters from BB+PLE fitting.	72
5.15	WAM-0 and ACS light curves represented by two components models.	73
6.1	Histograms of bolometric luminosities, and scatter plot between the emission area R^2 and the luminosity.	79
6.2	Relation between the bolometric BB luminosity and that of the hard X-ray PL component in the 1–300 keV energy range.	83
6.3	Schematic view of a possible interpretation	85
A.1	Demonstration of the pile-up simulator.	96
A.2	Relation between dead-time and count rate of results of the pile-up simulator and observed bright solar flares.	98

List of Tables

2.1	Comparison of the three giant flares referred from Mereghetti (2008)	25
3.1	Characteristics of <i>Suzaku</i> -WAM from Yamaoka et al. (2009)	36
3.2	Characteristics of <i>Swift</i> -BAT from Barthelmy et al. (2005)	40
3.3	Characteristics of <i>Swift</i> -XRT taken from Burrows et al. (2005)	41
4.1	Trigger Time of BST data from Terada et al. (2009a)	48
4.2	Observed data sets	52
B.1	Detected Events	99
C.1	Spectral parameters of acceptable BB fitting	113
C.2	Spectral parameters of acceptable OTTB fitting	116
C.3	Spectral parameters of acceptable PL fitting	118
C.4	Spectral parameters of acceptable BBBB fitting	121
C.5	Spectral parameters of acceptable BBOTTB fitting	121
C.6	Spectral parameters of acceptable BBPL fitting	122
C.7	Spectral parameters of acceptable BBPLE fitting	122

Chapter 1

Introduction

Neutron star is one of the suitable experimental sites to study exotic physics in strong gravity, magnetic and electric fields, since the discovery of a radio pulsar in 1967 ([Hewish et al. 1968](#)). Large numbers of pulsars, more than 1,500 objects, have been discovered so far ([Manchester et al. 2005](#)) with marked improvement of observational instruments and techniques. Although properties of classical pulsars, birth origin, emission mechanism, strength of magnetic field, and etc., are still not unresolved problems, further enigmatic class of pulsars exist, which cannot be understood by a standard framework of typical pulsars; they are called as anomalous X-ray pulsars (AXPs) and soft gamma repeaters (SGRs). The AXPs and SGRs are considered to be have hundred times stronger magnetic field than typical pulsars, and to be candidate of “magnetars”. However exact evidence of extreme magnetic field has not been revealed observationally. Since the observational properties of the two classes of pulsars and their phenomena enable us to possibly understand the fundamental physics there under the extra strong magnetic field strength, we performed to reveal them with the hard X-ray observation of a magnetar in this present thesis.

Interesting feature of magnetar is that estimated surface magnetic field of some ones are stronger than quantum critical field $B_Q = m_e^2 c^3 / \hbar e = 4.4 \times 10^{13}$ G at which the cyclotron energy equals the electron rest mass. In this field, exotic process of photon splitting and its inverse process of photon merging occurring are expected (e.g., [Thompson & Duncan 1995](#)). We consider no astronomical object to achieve these extreme field without magnetars, therefore they provide us only environment of the experiment the exotic phenomena. If the AXPs and SGRs really have the strong field like that of magnetars, aside from as described

physical interest above, many astrophysical problems are open. Because several phenomena are not explained completely by the typical framework of pulsars, why they have the extreme field, how did they born, what is the energy source of emission, what structure of magnetic field, and etc. By contraries, resolving the open problems is important to investigate whether the two classes of pulsars are really magnetars.

The aim of the present thesis is to take hint of energy source of magnetar phenomena and radiation mechanism, through measuring of emitted energy spectra, radiated energy, and those variation in sub-MeV energy band from a magnetar candidate, AXP 1E 1547.0–5408. The sub-MeV band observations have been reported only rare bright hard X-ray bursts, since persistent emission and typical bursts from AXPs and SGRs are too weak to measure exact brightness due to absence of sensitivity and effective area of hard X-ray detectors. In this thesis, we reported spectral analysis of individual hard X-ray bursts observed by *Suzaku* wide-band all-sky monitor, which has the largest effective area among currently working hard X-ray spectrometers in 0.3–6.2 MeV range on-board the astronomical satellite. We discuss energy source of the burst emission and its mechanism.

Chapter 2

Review

Contents

2.1	Physical Parameters in Rotation Powered Pulsars	14
2.2	Overview of AXPs and SGRs	17
2.3	Persistent X-ray Emission from AXPs and SGRs	19
2.3.1	Time Variation	19
2.3.2	Energy Spectra	20
2.4	Burst Emission from AXPs and SGRs	22
2.4.1	Giant Flare	23
2.4.2	Intermediate Flare	24
2.4.3	Short burst	25
2.5	Magnetars Hypothesis	27
2.5.1	Magnetized Neutron Star Model	28
2.5.2	Interesting Phenomena in Strong Magnetic Field	29
2.5.3	Alternative Models for AXPs and SGRs	30
2.6	Target Object; AXP 1E 1547.0–5408	30
2.6.1	Overview of AXP 1E 1547.0–5408	30
2.6.2	Activity on 2008 October and 2009 January	31
2.7	Scope of Present Thesis	32

In this chapter, we firstly introduce basic information of classical isolated neutron stars, i.e., rotation-powered pulsars in §2.1. In the following sections of §2.3 and §2.4, we summarize the observational properties of AXPs and SGBs, and show the current interpretations on physics mechanisms in the magnetar systems in §2.5. Then, we introduce a specific object which we observed in §2.6 and briefly summarize the purpose of this thesis in 2.7.

2.1 Physical Parameters in Rotation Powered Pulsars

Neutron star pulsars can be classified into two types of classes from the point of view in the emission mechanisms from the objects; accretion-powered pulsars and rotation-powered pulsars. The accretion-powered pulsars are considered to be in a binary system (a star plus a neutron star). The gravitational potential of the accretion gas onto the neutron star is converted into the high temperature plasma, which emits X-ray; i.e., accretion-powered pulsars emit high-energy photons whose energy source is the gravity. On the other hand, the rotation-powered pulsars are considered to be isolated neutron stars, where no energy input occurs to the system. The only energy source to drive high-energy photons from the system is the rotational energy of the magnetic field as described below.

Rotation energy E of a pulsar is estimated to be, assuming neutron star is spherical rigid-body,

$$E = \frac{1}{2}I\Omega^2 = 2\pi^2IP^{-2}, \quad (2.1)$$

where I , Ω and P are the moment of inertia, the angular velocity and spin period of the pulsar of $P = 2\pi/\Omega$, respectively. Rotation-power is defined by the loss rate of the rotation energy E as a spin-down luminosity, using time derivative of its period \dot{P} ,

$$\begin{aligned} L_s &= -\frac{dE}{dt} = 4\pi^2IP^{-3}\dot{P} \\ &= 4.3 \times 10^{35} \left(\frac{P}{1\text{ s}}\right)^{-3} \left(\frac{\dot{P}}{10^{-11}\text{ s s}^{-1}}\right) \text{ erg s}^{-1}, \end{aligned} \quad (2.2)$$

where I is assumed by neutron star mass of 1.4 times solar mass 2.79×10^{33} g and a radius of

10^6 cm. On the other hand, assuming dipole radiation and under the define of rotation axis along to e_z , a magnetic momentum is written by $\mathbf{m} = \frac{R^3 B}{2}(\sin \theta \cos \Omega t \cdot \mathbf{e}_x + \sin \theta \sin \Omega t \cdot \mathbf{e}_y + \cos \theta \cdot \mathbf{e}_z)$ in orthonormal coordinates, where R , B , θ and t are the star radius, the magnetic field strength, the angle between magnetic and rotation axes and the time, respectively. Then Larmor formula, which indicates radiated power from accelerated/decelerated charge, is shown by

$$\begin{aligned} P_{\text{rad}} &= \frac{2}{3c^3} |\ddot{\mathbf{m}}|^2 \\ &= \frac{R^6 B^2 \Omega^4 \sin^2 \theta}{6c^3}. \end{aligned} \quad (2.3)$$

Therefore from equations 2.2 and 2.3, the magnetic field strength on the star surface is derived from P and \dot{P} as

$$\begin{aligned} B &= \sqrt{\frac{3Ic^3}{2\pi^2 R^6 \sin^2 \theta} \cdot P \dot{P}} \\ &= 2.1 \times 10^{14} \left(\frac{P}{1 \text{ s}} \right)^{\frac{1}{2}} \left(\frac{\dot{P}}{10^{-1} \text{ s s}^{-1}} \right)^{\frac{1}{2}} \text{ Gauss}. \end{aligned} \quad (2.4)$$

In equation 2.4, since generally we have no way of knowing of the angle θ , $\sin \theta = 1$ is assigned. Therefore assuming the P_{rmrad} equals observed X-ray luminosity L_X , we can estimate the B values of neutron stars.

For any spin down models, such as the magnetic dipole systems described above, we can write

$$\dot{\Omega} = -k\Omega^n, \quad (2.5)$$

where k is a positive constant value and n is so call a breaking index. If electromagnetic torque is generated by dipole magnetic filed, the breaking index is $n = 3$. The breaking index is derived by differentiation of equation 2.3, generally written by $n = \Omega \ddot{\Omega} / \dot{\Omega}^2$. If the angular velocity follows the relation of equation 2.3, the characteristic age τ of the pulsar is given by

$$\tau = \frac{1}{1-n} \cdot \frac{\dot{\Omega}}{\Omega} \left[1 - \frac{\Omega}{\Omega_0^{n-1}} \right], \quad (2.6)$$

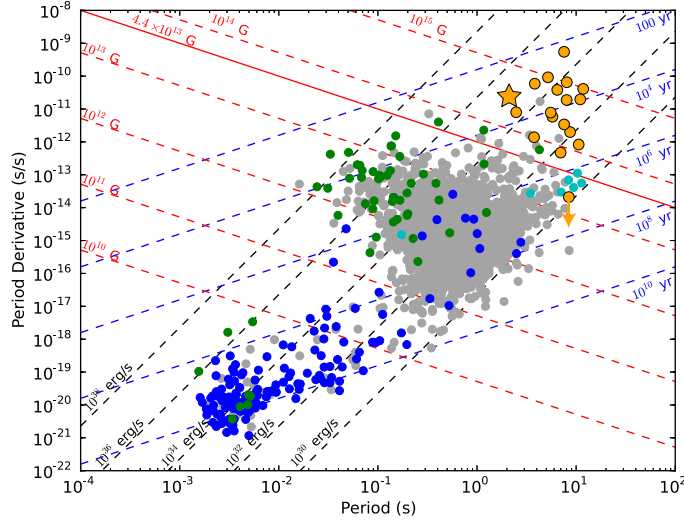


Figure 2.1: $P-\dot{P}$ diagram. Blue, gray, cyan, green and orange circulars are binary pulsars, isolated radio pulsars, X-ray isolated neutron stars, X-ray/gamma-ray emitting pulsars, and AXPs and SGRs. Orange star indicates AXP 1E 1547.0–5408. Black, red, and blue dashed lines indicate estimated level of L_s , B , and τ , respectively. Especially, red solid line represents B_Q .

where Ω_0 is the value at birth. Then let us consider the case of $n = 3$ and $\Omega_0 \gg \Omega$, we have

$$\begin{aligned} \tau &= \frac{\dot{\Omega}}{2\Omega} = \frac{P}{2\dot{P}} \\ &= 1.6 \left(\frac{P}{1\text{ s}} \right) \left(\frac{\dot{P}}{10^{-11} \text{ s s}^{-1}} \right)^{-1} \text{ kyr.} \end{aligned} \quad (2.7)$$

All of above derived parameters, as the spin-down luminosity L_s , the dipole magnetic field strength B and the characteristic age τ , are derived from observational rotation period P and its derivative \dot{P} , and they are useful indicator of radiation activity status of the isolated neutron stars. Figure 2.1 shows observed $P-\dot{P}$ distribution archived in Australia Telescope National Facility pulsar catalog ¹ and McGill magnetar catalog ².

¹<http://www.atnf.csiro.au/research/pulsar/psrcat>

²<http://www.physics.mcgill.ca/pulsar/magnetar/main.html>

2.2 Overview of AXPs and SGRs

In the last three-decade, Soft Gamma Repeaters (SGRs) or Anomalous X-ray Pulsars (AXPs; for reviews, see [Kaspi 2007](#); [Mereghetti 2008](#); [Rea & Esposito 2011](#); [Woods & Thompson 2006](#)) have been discovered as candidate of magnetars. The SGRs are observed as flaring sources with the duration in the range from a few milliseconds to several hundred seconds, and AXPs are as continuous X-ray emitting sources with absent radio emission and slow rotation periods. Thus, initially SGRs and AXPs were interpreted as a subtype of classical gamma ray burst (GRB) ([Mazets et al. 1979](#)) and a peculiar X-ray binary ([Fahlman & Gregory 1981](#)). At least 26 objects are defined as SGRs, AXPs, or their candidates ([Olausen & Kaspi 2014](#)), which commonly have following observational properties ([Mereghetti 2008](#)),

- (1) spin period in the 2–12 s range.
- (2) in some case, association with supernova remnants.
- (3) lack of evidence of binary companions.
- (4) luminosity larger than the spin-down power.
- (5) suddenly bright flare emissions and transient outbursts.

so the two classes are considered to have similar birth origin, radiation mechanism, magnetic structure and strength.

Figure 2.1 shows $P-\dot{P}$ diagram. Rotation period P and the derivative \dot{P} is enormously useful tool to characterize the neutron stars for ordinary pulsars. For AXPs and SGRs, (1) those observed rotation periods are relatively slow (2–12 s) and the derivative are large ($10^{-13} - -10^{-9}$ s/s), which suggest two or three orders of stronger magnetic field ($\sim 10^{14}$ – 10^{15} G) and younger characteristic age (~ 100 – $10,000$ yr) than typical radio pulsars ([Olausen & Kaspi 2014](#)). Especially, almost estimated magnetic fields are beyond the critical value of electron B_Q . (2) Some supernova remnants (SNRs) associate with magnetars (e.g., 1E 2259+586 with SNR CTB 109, CXOU J171405.7–381031 with SNR CTB 378, 1E 1841–045 with SNR Kes 73), and they are located in the low Galactic latitudes ([Olausen & Kaspi 2014](#)). Ages of three SNRs are estimated by X-ray observations with different method than $P-\dot{P}$ estimation, and these ages are also young; 4.3 kyr (Kes 73), 220 kyr (CTB 109), and 1.9 kyr (N49) ([Sasaki et al. 2004](#); [Vink & Kuiper 2006](#)). According to [Kumar et al. \(2014\)](#), SNR Kes 73 associated with AXP 1E 1841–045 is observed deeply with *Chandra* and *XMM-Newton*, and its progenitor is estimated as massive $> 20 M_{\odot}$ measuring

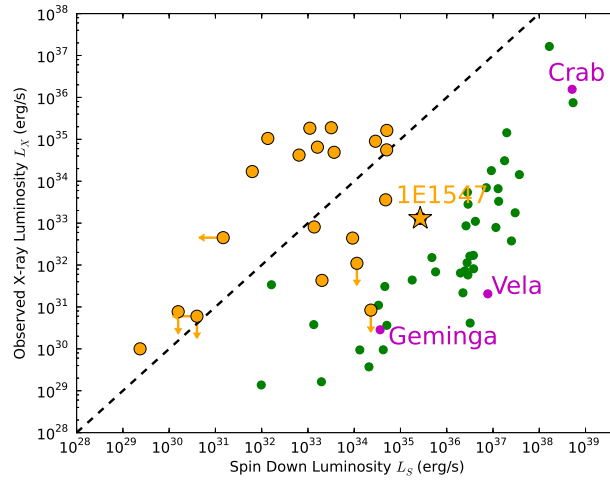


Figure 2.2: Relation of calculated spin down luminosity versus observed X-ray luminosity diagram. Plotted data are taken from ATNF pulsar archive and McGill magnetar archive. Green and magenta circulars are X-ray/gamma-ray emitting pulsars and famous pulsars such as Crab, Geminga and Vela pulsars. Orange points are AXPs and SGRs, and star mark is AXP 1E 1547.0–5408. The dashed line represents that the spin down luminosity is the same as the observed X-ray luminosity.

abundance. Nicholl et al. (2013) suggested a possibility that supernovae of magnetar progenitors show super-luminous slow-fading. In addition, (3) companion star has not been discovered to date. These properties therefore are good benchmarks that magnetars are young and isolated neutron stars.

Highly important feature is that (4) observed X-ray luminosities of some AXPs and SGRs are much larger than their rotational energy losses (Olausen & Kaspi 2014). Figure 2.2 shows a comparison between observed X-ray luminosity L_X and the rotation-energy L_S . As described above, since they have no binary system, these X-ray radiation energy sources cannot be explained by accretion from binary star or the rotation power. Therefore that main energy source is those ultimate magnetic energy, is “magnetar” hypothesis. Then due to the re-arrangement of the magnetic fields and its dispersion, (5) transient outbursts and sudden bursts are considered to be induced.

Generally observed emissions from AXSS and SGRs are classified by “persistent emission” and “burst emissions”. Continuous emission excepting the latter (described in §2.4) is defined the former (§2.3). Those two class emissions are further named by brightness as “outburst” and “quiescent”, and “giant flare”, “intermediate flare”, and “short burst”. The details are described following sections.

2.3 Persistent X-ray Emission from AXPs and SGRs

2.3.1 Time Variation

Some AXPs (e.g., 1E 1547.0–5408, 1E 1048.1–5937) show flux enhancement 1–2 orders in long-term scale from hours to months. Figure 2.3 shows X-ray light curve of AXP 1E 1547.0–5408 for about three years (Iwahashi et al. 2013). In this figure, two flux-increased regions are called as outburst phase, and other intervals are quiescent phase. During the outburst, some X-ray observations reported that X-ray pulse shape and its frequency are changed than during the quiescent (Archibald et al. 2013; Gavriil et al. 2004). Interestingly, although normal glitches, which is spin-up rotation phenomenon known in radio pulsars, are also discovered from AXPs (i.e., Dib et al. 2008; Kaspi et al. 2000), noteworthy is that (Archibald et al. 2013) reported a sudden spin-down phenomenon “anti-glitch”. Since existing models of neutron star of spin-down do not predict this anti-glitch, rethinking of glitch models is required.

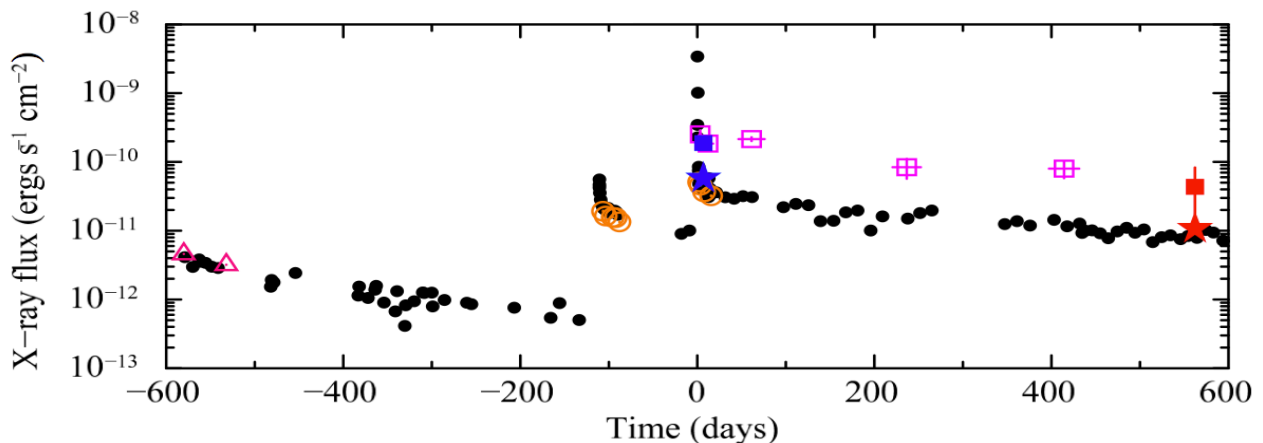


Figure 2.3: Long-term X-ray light curve of AXP 1E 1547.0–5408 from UTC 2009 January 22 01:32:41 (Iwahashi et al. 2013). The data points of black filled circles, pink open triangles, orange open circles, and star points are the absorbed *Swift*/XRT 2–10 keV flux (Enoto et al. 2012), the absorbed *XMM-Newton* 1–10 keV flux (Halpern et al. 2008), the absorbed *Chandra* 0.5–7 keV (Ng et al. 2011), and the absorbed *Suzaku* 2–10 keV X-ray fluxes, respectively. The hard X-ray components are also overlaid; the magenta square points are the unabsorbed *INTEGRAL* 20–150 keV X-ray fluxes (Kuiper et al. 2012).

2.3.2 Energy Spectra

X-ray emissions from AXPs and SGRs in the persistent phase are represented mainly in the soft X-ray band below 10 keV. The energy spectra of the persistent emissions are often fitted by combination of a power-law plus a blackbody (PL+BB) model and/or two temperature blackbodies (2BB) model empirically, and references therein [Mereghetti \(2008\)](#). In the energy spectra of a SGR object (SGR 0418+5729), variable absorption line is discovered ([Tiengo et al. 2013](#)). Figure 2.4 shows the observed absorption features. One of the interpretations of the absorption line is due to proton cyclotron resonance scattering. If the absorption line is made by protons, the cyclotron energy of Landau level is written as

$$E_p = \frac{6.3}{1+z} \left(\frac{B}{10^{15} \text{ G}} \right) \text{ keV}, \quad (2.8)$$

where $(1+z)^{-1} = (1 - 2GM_{\text{ns}}/(Rc^2))^{1/2}$ represents the gravitational redshift with typical neutron star mass of $1.4 M_{\odot}$ and its radius of 12 km. Therefore the results support that the SGRs have really strong magnetic field. However, the electron cyclotron feature is not yet denied, which resonance energy is

$$E_e = \frac{11.6}{1+z} \left(\frac{B}{10^{12} \text{ G}} \right) \text{ keV}. \quad (2.9)$$

To resolve the question, future work of high energy resolved observation with ASTRO-H satellite would provide us advanced answers ([Kitamoto et al. 2014](#)).

For a long time, emissions from AXPs are thought to only soft X-ray band, however in a decade, hard X-ray emission above 10 keV have been discovered from several magnetars (e.g., [Enoto et al. \(2010b\)](#); [Götz et al. \(2006\)](#); [Kuiper et al. \(2006, 2004\)](#); [Nakagawa et al. \(2009\)](#); [Rea et al. \(2009\)](#)), and thanks to deep observations by recent-sensitive hard-X-ray instruments. The hard X-ray spectra are well measured in comprehensive SGRs and AXPs in persistent phase. Figure 2.5 shows broadband spectra observed by *Suzaku* ([Enoto et al. 2010b](#)). Its components are often represented by a single power-law (PL) function with a hard photon index of $\Gamma \sim 1$. According to indicated upper-limit fluxes with high-energy observation in GeV band with *Fermi*-LAT ([Abdo et al. 2010](#)) and in MeV band with *CGRO*-COMPTEL ([den Hartog et al. 2006](#); [Kuiper et al. 2006](#)), high-energy photons above MeV energy range have not been observed to date, and the hard X-ray component extending from 10 keV should have a cut-off feature below 750 keV observationally, whereas such a

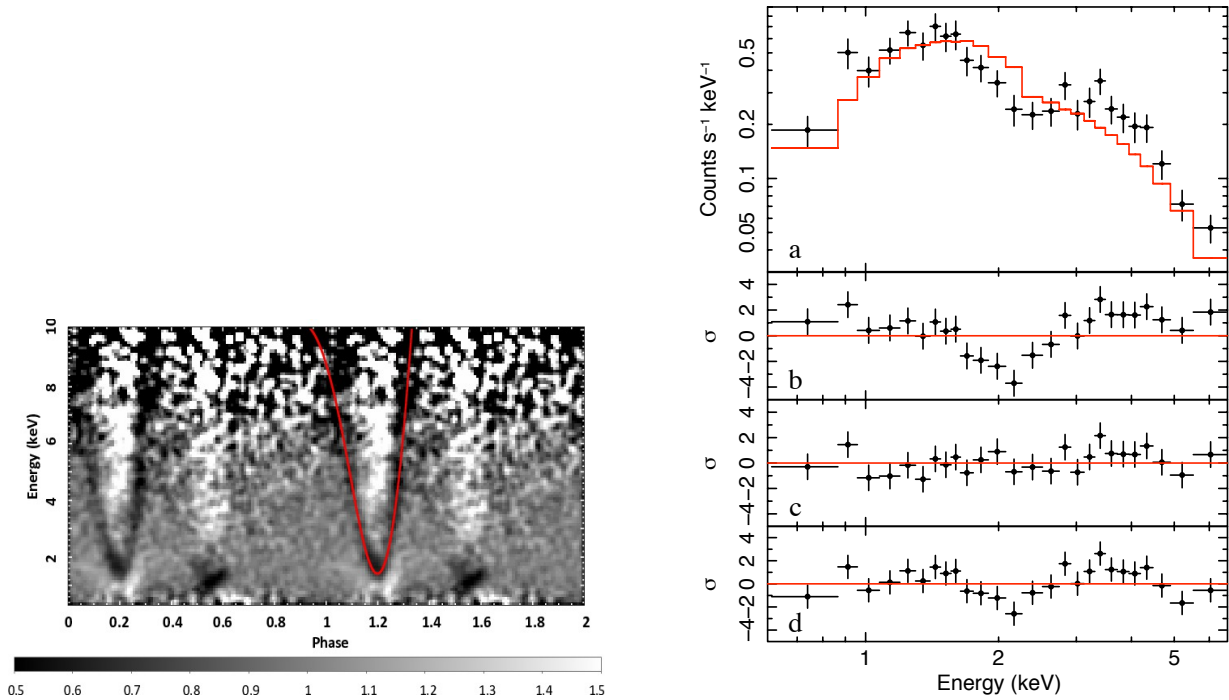


Figure 2.4: Phase-dependent spectral feature and a sample of phase resolved spectrum observed by *XMM-Newton* (from [Tiengo et al. \(2013\)](#)). (Left) the red line shows (for only one of the two displayed cycles) the results of a simple proton cyclotron model consisting of a baryon-loaded plasma loop emerging from the surface of a magnetar and intercepting the X-ray radiation from a small hotspot. (Right) Spectrum from the phase interval 0.15–0.17 (black dots) and best fit model of the phase-averaged spectrum, rescaled with a free normalization factor (red line). Bottom panels are residuals with three models, **b**; this model, **c**; after the addition of an absorption line with the model of **b**, and **d**; an absorbed blackbody plus power law model with free temperature, photon index and normalizations.

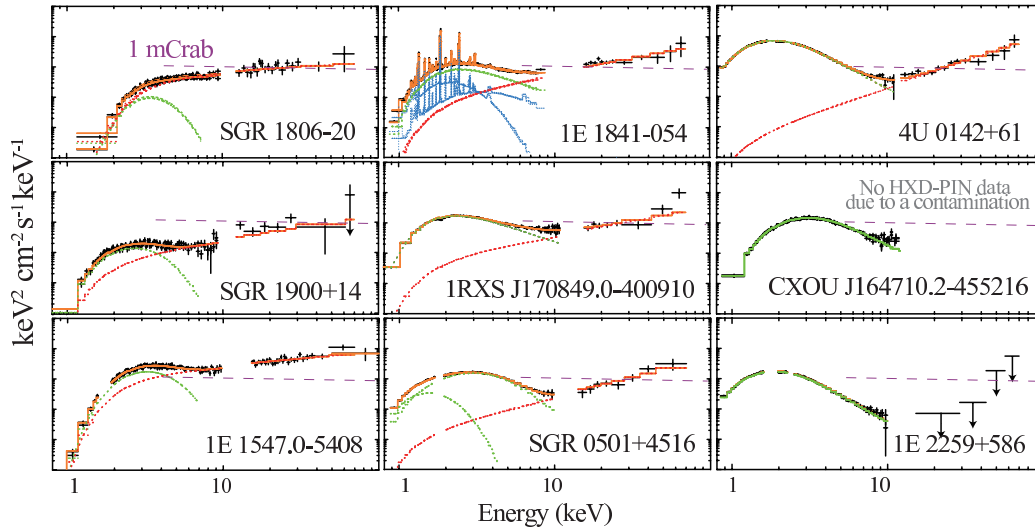


Figure 2.5: *Suzaku* view of nine AXPs and SGRs $\nu F\nu$ spectra taken from [Enoto et al. \(2010b\)](#) ([Rea & Esposito 2011](#)). The spectra without background components include interstellar absorption. Green, red and blue lines represent the soft X-ray components, the hard X-ray components and the SNR contamination. Horizontal blue lines are a 1 mCrab intensity.

feature has not discovered yet due to lack of the detectors sensitivities. Therefore, detail measurement of the spectral shape around MeV energy band is a new discovery space to investigate emission mechanism.

2.4 Burst Emission from AXPs and SGRs

Sudden phenomena of SGRs and AXPs (i.e., flare up events) are observationally classified as three classes according to its properties of duration time and radiated luminosity; “giant flare”, “intermediate flare” and “short burst”. The burst emissions are known to accompany the outburst emissions (§2.3.1). Figure 2.6 shows a typical spectrum of the burst emissions ([Woods & Thompson 2006](#)). The spectra of the SGR/AXP bursts show different shapes with the other burst phenomena.

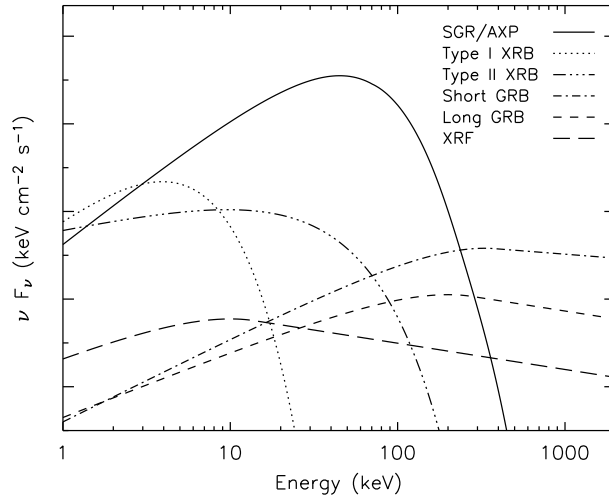


Figure 2.6: Characteristic energy spectra of high-energy burst phenomena (Woods & Thompson 2006). The SGR/AXP burst spectrum shows a shape of a combination of two blackbodies. XRB, GRB, and XRF are X-ray burst, classical gamma-ray burst, and X-ray flushes, respectively.

2.4.1 Giant Flare

The giant flares are bright burst phenomena with long duration of about few hundred seconds. They follow semi-periodic signals, which is called as pulsation tail, and some bright events whose fluxes exceed about hundred times of the Eddington luminosity (see review, Mereghetti 2008). These flares are rare, which are historically only three events, and these observed properties are listed in Table 2.1 (Mereghetti 2008). These light curves show extreme bright hard initial spike and following pulsation tail (Feroci et al. 2001; Hurley et al. 1999). Coherent modulations in the light curve during the pulsation tail epoch representing a frequency at a few seconds strongly reflect the neutron star rotation periods.

The initial spike of all giant flares are too bright to avoid saturating astronomical X-ray/gamma-ray detectors, and particularly one of SGR 1806–20 are two orders magnitude brighter than the following emission. As summarized in Table 2.1, the shape of the time variation in the light curve show steep rise and fast decay; fast rise time at a hundred milliseconds and power-law type decay with time scale of a few hundred seconds. At the pulsating tail intervals, the light curve shapes are well reproduced by a trapped fireball model (Feroci et al. 2001; Guidorzi et al. 2004; Hurley et al. 2005), which indicate a flux time-variation of cooling hot pair-photon plasma stuck in the strong magnetic field. The X-ray time variation by the trapped fireball cooling model is described by $L_X(t) = L_X(0) \left(1 - \frac{t}{t_{\text{evap}}}\right)^X$ (Thompson

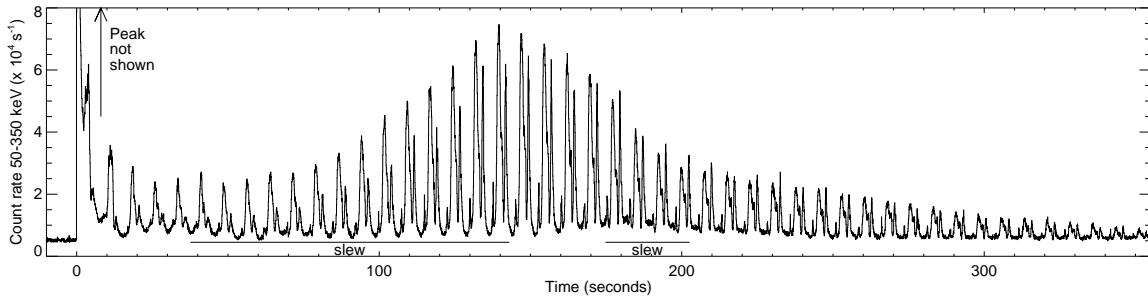


Figure 2.7: *Swift*-BAT light curve of 2004 December 27 giant flare from SGR 1806–20 is in > 50 keV energy range with 64 ms time resolution referred from (Hurley et al. 1999). Note that a peak at 140 s is due to slewing the spacecraft, its is not intrinsic phenomenon.

& Duncan 2001), where t_{evap} and χ mean an evaporation time and benchmark of the fireball geometry, respectively. The index χ indicates the dimension of the geometry surface; $\chi = 2$ for a spherical, $\chi = 1$ for a cylindrical and $\chi = 0$ for a thin slab. Giant flares in 1998 from SGR 1900+14 and in 2004 from SGR 1806–20 obtained $\chi \sim 3.2$ (Feroci et al. 2001) and ~ 1.5 (Hurley et al. 2005), respectively.

Energy spectra in the X-ray band of the initial spikes in all three giant flares are characterized by emissions from thermal plasma with an extreme hot temperature or an empirical spectral shape by the power-law model with the high-energy cutoff; thermal plasma of as an optically thin thermal bremsstrahlung (OTTB) or a blackbody (BB) of $kT \sim 100$ keV (Hurley et al. 1999) or non-thermal emission from accelerated plasma as a single power-law with exponential cut-off function (PLE) with a hard photon index ~ 0.7 and cut-off energy ~ 670 keV (Frederiks et al. 2007; Palmer et al. 2005). X-ray spectra during the pulsation tail intervals show a softer shape than initial spike, which can be reproduced by the OTTB with the temperature at 10 keV. In addition to the soft thermal components, Boggs et al. (2007); Frederiks et al. (2007); Guidorzi et al. (2004) suggest that hard power-law components extending to MeV range exist which seem like hard X-ray components in the persistent emission spectra.

2.4.2 Intermediate Flare

Intermediate flares are occasional events, and second class of magnetar bursts. Its show long duration of few ten seconds, longer than at least half of rotation period of the pulsar, and

Table 2.1: Comparison of the three giant flares referred from [Mereghetti \(2008\)](#)

Source	SGR 0526–66	SGR 1900+14	SGR 1806–20
Date	March 5, 1979	August 27, 1998	December 27, 2004
Assumed distance (kpc)	55	15	15
Initial spike			
Duration (s)	~ 0.25	~ 0.35	~ 0.5
Peak luminosity (erg s^{-1})	3.6×10^{44}	$> 8.3 \times 10^{44}$	$(2/5) \times 10^{47}$
Fluence (erg cm^{-2})	4.5×10^{-4}	$> 1.2 \times 10^{-2}$	0.6/2
Isotropic energy (erg)	1.6×10^{44}	$> 1.5 \times 10^{44}$	$(1.6/5) \times 10^{46}$
Pulsating tail			
Duration (s)	~ 200	~ 400	~ 380
Fluence (erg cm^{-2})	1×10^{-3}	9.4×10^{-3}	5×10^{-3}
Isotropic energy (erg)	3.6×10^{44}	1.2×10^{44}	1.3×10^{44}
Spectrum	$kT \sim 30 \text{ keV}$	$kT \sim 20 \text{ keV}$	$kT \sim 15\text{--}30 \text{ keV}$
Pulse period (s)	8.1	5.15	7.56
QPO frequencies (Hz)	43	28, 54, 84, 155	18, 30, 92.5, 150, 625, 1840

bright peak luminosity reaching $\sim 40^{41} \text{ erg s}^{-1}$, which is weaker than those of giant flares but greater than short bursts. Light curves of these flares are reported in various shapes, and Figure 2.8 shows several examples. Light curves of some intermediate flares show similarity properties with giant flares such as following pulsation tail and represented by the fireball model ([Guidorzi et al. 2004](#); [Olive et al. 2004](#)). In addition, since almost intermediate flares are observed from objects of giant flare occurring ([Guidorzi et al. 2004](#)) and the latter flares follow the former flares in the days or months ([Lenters et al. 2003](#)), the intermediate flares are suggested as residual energy release of giant flares and two different class flares have same emission mechanism ([Woods & Thompson 2006](#)).

X-ray spectra of the intermediate flares are represented by 2BB ([Feroci et al. 2004](#); [Olive et al. 2004](#)) and/or PL models (photon index ~ 2), generally. These spectra are hard than the tail component of giant flares. Since spectral and temporal properties are similar to classical GRBs, these events are not indistinguishable without localized information.

2.4.3 Short burst

Short bursts are typical burst emission from magnetars. Duration is shorter about 100 ms and weaker brightness (up to $\sim 10^{42} \text{ erg s}^{-1}$) than other class flares. The waiting time

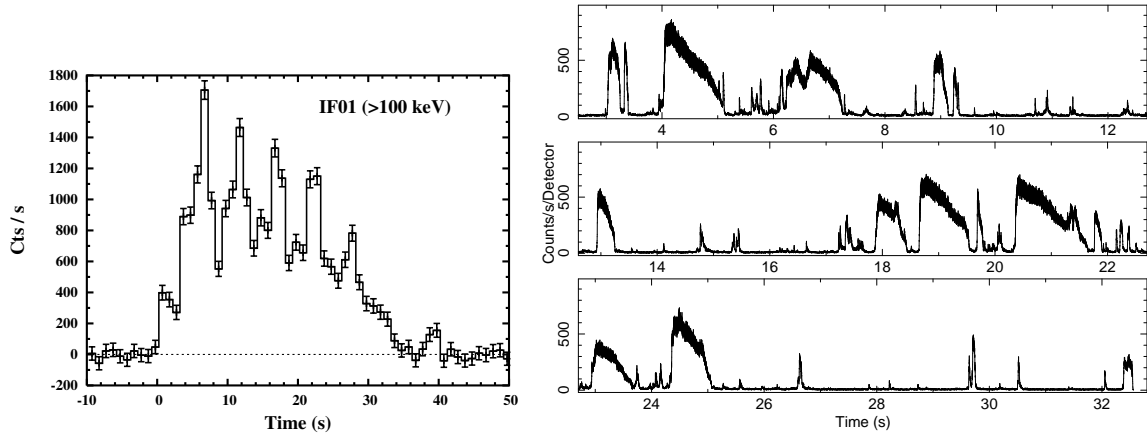


Figure 2.8: Light curves of intermediate flares. (Left panel) 2001 April 18 event from SGR 1900+14 obtained by *BeppoSAX* from [Guidorzi et al. \(2004\)](#). There is not a initial spike but pulsation tail is followed. (Right panel) 2006 March 29 burst forest of same object observed by *Swift*-BAT in 15–100 keV range ([Israel et al. 2008](#)). In this paper, longer than 500 ms events are defined as intermediate flares and seven flares are detected.

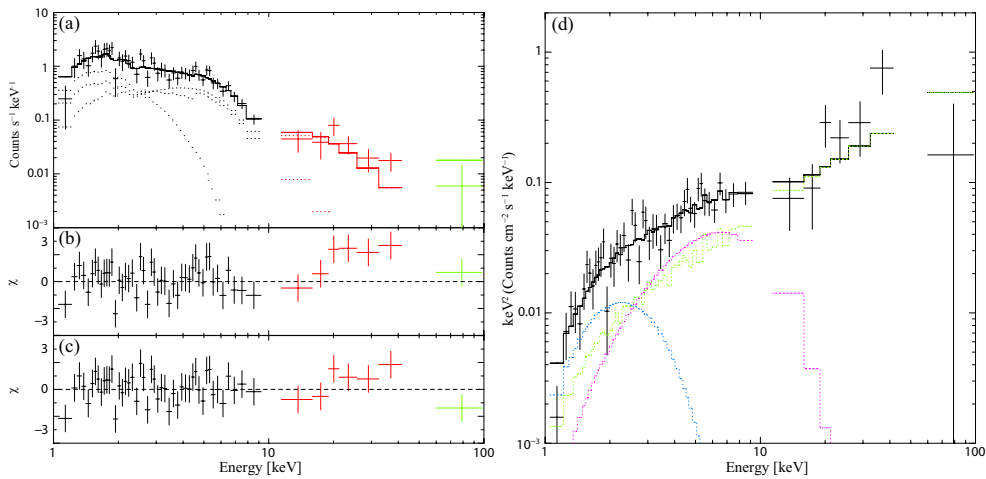


Figure 2.9: (a) Background-subtracted *Suzaku* spectra of the summed 31 short bursts from SGR 0501+4516, fitted jointly with a 2BB+PL model ([Nakagawa et al. 2011](#)). Panels (b) and (c) show residuals from the 2BB and 2BB+PL fits, respectively. Panel (d) is the same as panel (a), but in the νF_ν form.

between event-by-event is known to distribute the lognormal properties (e.g., Hurley et al. 1994). Typical X-ray spectra of the short bursts are well reproduced by 2BB with temperatures of $kT_{\text{low}} \sim 2\text{--}4\text{ keV}$ and $kT_{\text{high}} \sim 8\text{--}15\text{ keV}$ (Esposito et al. 2007; Feroci et al. 2004; Nakagawa et al. 2011, 2007). For bright short bursts ($> 10^{41}\text{ erg s}^{-1}$), a correlation between the BB temperature and emitting surface area size ($R^2 \propto kT^{-3}$) is reported (Israel et al. 2008). In addition, fitting by the 2BB model exhibits a relation between two temperatures with $3kT_{\text{low}} \sim kT_{\text{high}}$ (Nakagawa et al. 2009). This relation is confirmed in the persistent emission (Gotthelf & Halpern 2005; Morii et al. 2010) and intermediate flares (Olive et al. 2004). Moreover Nakagawa et al. (2011) discovered a hard X-ray component in spectrum of accumulated weak short bursts from SGR 0501+4516. Figure 2.9 shows the reported spectra of the hard X-ray component. Interestingly, this paper reported that the measured photon index is consistent with those observed from the persistent emission (Enoto et al. 2010c; Rea et al. 2009). The relation and spectral similarities between the spectra of burst emission and the persistent emission, suggest a common radiation process producing both kinds of emission and support the idea that these emissions consist of numerous micro-bursts (Nakagawa et al. 2011, 2009). If its suggestion is truth, the short burst spectra should also have the cut-off feature in sub-MeV range like that of the persistent emission. Therefore revealing the spectral shape in the high-energy range is important to examine this hypothesis. However, from the short burst spectra, the high-energy photons reaching MeV band has not been reported so far. In fact, detections of around 1 MeV photons are reported from only two intermediate flares from SGR 1900+14 (Woods et al. 1999) and two giant flares from SGR 1900+14 (Hurley et al. 1999) and SGR 1806–20 (Boggs et al. 2007; Frederiks et al. 2007; Hurley et al. 2005; Palmer et al. 2005).

2.5 Magnetars Hypothesis

Although recent observational and theoretical magnetar researches collect hint of magnetar activity bit by bit, there is a large number of conflicts to understand brief origin, source energy of emission, magnetic field structure, process of magnetic decay, absence of radio radiation and much more. In this section, we introduce some interpretations of magnetar and expected exotic physical phenomena (see reviews by Mereghetti 2008; Woods & Thompson 2006).

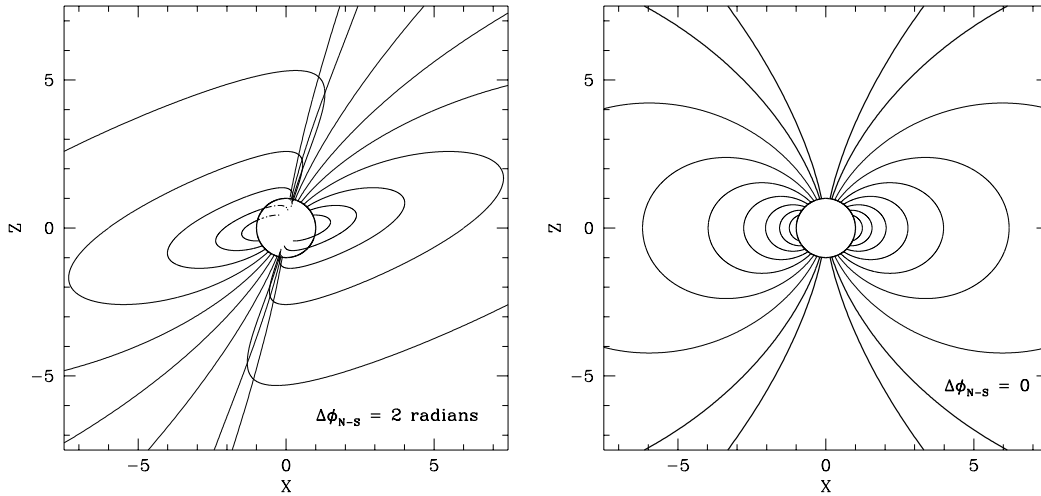


Figure 2.10: Twisted magnetosphere (left panel) and a pure dipole (right panel) taken from Thompson et al. (2002).

2.5.1 Magnetized Neutron Star Model

Duncan & Thompson (1992) proposed strong magnetized neutron star hypothesis, namely “magnetar”, to explain observed sporadic burst emission from SGRs. Generally magnetar model is that highly magnetized neutron stars than the quantum critical field $B_Q \sim 4.4 \times 10^{13}$ G (Duncan & Thompson 1992; Thompson & Duncan 1995), and its magnetic field decay powers variable X-ray emission. Thompson et al. (2002) suggests that magnetars have at least ten times stronger toroidal magnetic field inner the star than poloidal filed. The strong field is twisted globally. Figure 2.10 shows illustration of a twisted dipole filed (Thompson et al. 2002). Although untwisted filed shares the neutron star crust, the rotation motion of the crust makes the field helicity and twisted. Figure 2.11 shows a stable field of mixed poloidal-toroidal twisted torus (Braithwaite 2009). The energy of the outbursts and the sudden bursts are considered to be powered by rearrangement of its twisted strong magnetic field and/or cracking of neutron star crust due to star-quakes.

The Origin of the strong magnetic field is unclear, how do the strong magnetic field made? One of the popular hypothesis is that magnetars born with rapid rotation proto-neutron stars ($P_0 \sim 0.6\text{--}3$ ms; ordinary pulsar $P_0 > 10$ ms). Duncan & Thompson (1992) suggested field as strong as $3 \times 10^{17} (P_0/1\text{ms})^{-1}$ G can be generated by $\alpha - \Omega$ dynamo with differential rotation. If proto-neutron star rotates with $P_0 = 1$ ms, then rotation energy

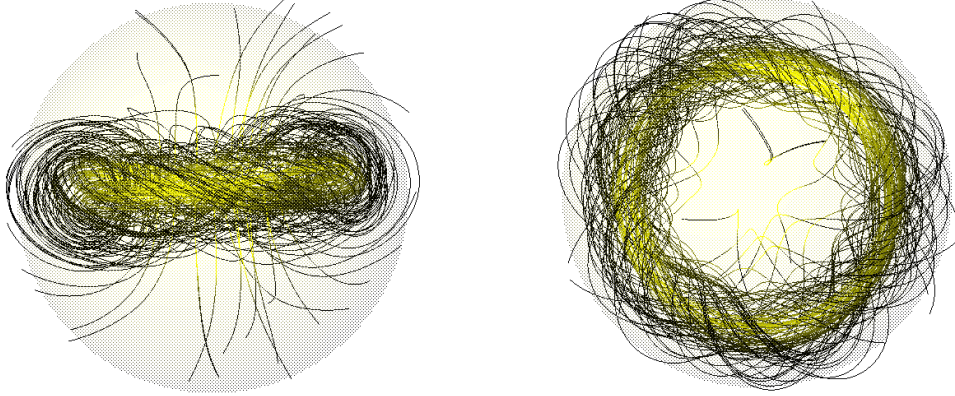


Figure 2.11: Stable twisted-toroid field in a star (Braithwaite 2009). Yellow and black lines indicate strong and weak magnetic field, respectively.

reaches to $E_{\text{rot}} = 3 \times 10^{52} (P_0/1 \text{ ms})^{-2}$. The extreme energy might be provided with surrounding supernova during ~ 10 s, and magnetar rapidly spin-downs due to magnetic break. Therefore SNRs surrounding magnetars should have a huge energy like that of hyper-nova than ordinary SNRs, and X-ray observation of measuring expansion energy of the SNRs hosting magnetars is important to reveal the magnetar origin. However according to Vink & Kuiper (2006), measured expansion energies ($\sim 10^{51}$ erg) of three SNRs do not meet the condition of $P_0 \sim 0.6\text{--}3$ ms.

2.5.2 Interesting Phenomena in Strong Magnetic Field

If the strong magnetic field above the critical value B_Q exists on the neutron star surface, quantum electrodynamics suggest that exotic phenomena (i.e., photon splitting) occur (Harding & Lai 2006). The photon splitting phenomenon is that one photon is divided into two or more number of photons due to interaction between virtual pair and the magnetic field through vacuum polarization in photon propagation when its pair radiate,

$$\gamma \leftrightarrow \gamma + \gamma. \quad (2.10)$$

In the thermal equilibrium, the photon splitting and its inverse phenomenon (photon merging) balance (Thompson & Duncan 1995). Two kinds of ordinary (O) and extraordinary (E)

polarization mode photons behave differently when those pass through the strong magnetic field, and the photon splitting occurs for only two polarization channels, $E \leftrightarrow O + O$ and $E \leftrightarrow E + O$.

2.5.3 Alternative Models for AXPs and SGRs

In contradiction to above described strong magnetized neutron star model, several alternative models do not require the strong field. An alternative model is called “fossil disk” or “fall-back disk” models which disk is made by dispersed-residual matters at supernova. This model naturally explains the relatively slow spin periods (2–12 s) than typical pulsars with rapid spin-down due to propeller torques. After the propeller phase, the disk matters are accreted into the central neutron star, and its neutron star are observed as AXP. Moreover, this model can explain observed optical/infrared emission as from the disk. Since this model suggest the energy source of magnetars is gravitational energy, the biggest benefit of this model do not require the strong field as the magnetar model. But the accretion model does not easily explain sudden magnetar bursts and flares, especially extreme bright flares exceeding Eddington limits.

Other alternative model is massive highly magnetized rotating white dwarf model (Malheiro et al. 2012). This model predicts the radiation source of magnetars is basically rotation energy. Observed X-ray luminosities of magnetars L_X and estimated rotational energy losses L_{rot} of the white dwarfs satisfy the condition of $L_X < L_{\text{rot}}$. Moreover observed radiated energies of giant flares are explained by energy release from involved glitch.

2.6 Target Object; AXP 1E 1547.0–5408

2.6.1 Overview of AXP 1E 1547.0–5408

AXP 1E 1547.0–5408 (SGR J1550–5418, PSR J1550–5418) is a magnetar associated with a young supernova remnant G327.24–0.13 (Gelfand & Gaensler 2007). Camilo et al. (2007) discovered a radio pulsation, and latest X-ray observation (Dib et al. 2012) derived a spin period (~ 2.1 s) and a spin down rate ($\sim 4.8 \times 10^{-11}$ s s $^{-1}$), which imply a strong dipole surface field of $\sim 3.2 \times 10^{14}$ Gauss and relatively young characteristic age of about 690 yr

among magnetars³. The spin period is the fastest, and the estimated age is the youngest among AXPs and SGRs (Figure 2.1). Recent radio observation with very long baseline interferometry (VLBI) reported by Deller et al. (2012) revealed detailed location of the object, R.A. (J2000) $15^{\text{h}}50^{\text{m}}54^{\text{s}}.12386$ and Decl. (J2000) $-54^{\circ}18'24''.1141$. In this thesis, we assume a distance to AXP 1E 1547.0–5408 of $d \sim 4$ kpc (Tiengo et al. 2010).

Radio pulsed emissions from AXPs/SGRs have been observed in only three objects included AXP 1E 1547.0–5408, the other two are XTE J1810–197 and PSR J1622–4950. Rea et al. (2012) indicated a possibility of that the radio emissions are power by the rotation energy of the neutron star. Therefore the radio emitting objects are considered to be a missing link between magnetar candidates and rotation-powered ordinary pulsars. Similarities between the two kinds also have been reported in Vink & Bamba (2009). They found extended emission source around the object, and suggested that it might be pulsar wind nebula.

2.6.2 Activity on 2008 October and 2009 January

Historically, this object shows three times outburst activities (see review Rea & Esposito 2011). First is 2007 August observed by *XMM-Newton* reported in Halpern et al. (2008) (pink triangles in Figure 2.3). Since those observations indicated flux decay at least before 2007 June 22, a whole of the activity is not revealed. Second activity is in 2008 October 3. During this outburst, *Swift* successfully detected several short bursts, and X-ray pulsations were observed (Israel et al. 2010). Moreover observed X-ray spectra (1–10 keV range) show softening; fitting by PL model, the photon index switches from ~ 2 to ~ 4 within about 10 days.

Finally, in 2009 January 22, the object became active phase and show a large number of bursts. The activity was noticed by several X-ray/gamma-ray detectors including *Swift* (Gronwall et al. 2009), *Fermi* (Connaughton & Briggs 2009), *INTEGRAL* (Mereghetti et al. 2009a; Savchenko et al. 2009), *Konus-Wind* (Golenetskii et al. 2009a,b,c), *RHESSI* (Bellm et al. 2009) and *Suzaku* (Terada et al. 2009b). These notices triggered several follow-up observations in broadband wavelength from radio to hard X-ray. Thereby many interesting temporal, spectral, and statistical investigations of sudden bursts, and persistent emissions in X-ray energy band of 0.1–200 keV were reported by many papers (Enoto et al. 2012, 2010a;

³<http://www.physics.mcgill.ca/~pulsar/magnetar/main.html>

Iwahashi et al. 2013; Kaneko et al. 2010; Kuiper et al. 2012; Lin et al. 2012; Scholz & Kaspi 2011; van der Horst et al. 2012; Younes et al. 2014).

Interestingly *Swift* and *XMM-Newton* follow-up observation discovered three X-ray rings centered on the object (Tiengo et al. 2010). To produce the ring, large energetic source is required at $1\text{--}20 \times 10^{44}$ erg, whose quantity is dependent on gas models. Tiengo et al. (2010) suggested that any bursts are the irradiating source among detected extreme flux events by *INTEGRAL* (Mereghetti et al. 2009b). Although measuring luminosities are crucial to investigate ambient environment of the object, it has not been determined accurately due to the candidate bursts are too bright to measure the exact flux (Mereghetti et al. 2009b; Savchenko et al. 2010).

2.7 Scope of Present Thesis

As described above sections, although detailed X-ray studies are already performed using several X-ray observatories, sub-MeV energy band study above 200 keV has not investigated yet. Therefore no body knows sub-MeV band energy spectra from AXP 1E 1547.0–5408 during the outbursts, and this energy band observation is new discovery space to investigate emission mechanism of an AXP. Main purpose of this presented thesis is to reveal the spectral shapes and radiated energy of burst emissions from a magnetar candidate object AXP 1E 1547.0–5408 using *Suzaku* wide-band all-sky monitor (WAM). Moreover using obtained *Suzaku*/WAM data, we also performed statistical study of observed count rate in the detector and yielded spectral parameters, and compare our results with previous reports about X-ray bursts and persistent emissions.

Chapter 3

Instrumentation

Contents

3.1	<i>Suzaku</i> Wide-band All-sky Monitor	33
3.1.1	Overview	33
3.1.2	Electronics for WAM	36
3.1.3	Energy Calibreation	38
3.1.4	Generating Energy Response Matrix	39
3.2	Other Instruments	39
3.2.1	<i>Swift</i> Burst Alert Telescope	39
3.2.2	<i>Swift</i> X-ray Telescope	40
3.2.3	<i>Fermi</i> Gamma-ray Burst Monitor	42
3.2.4	<i>INTEGRAL</i> Anti-Coincidence System	43

3.1 *Suzaku* Wide-band All-sky Monitor

3.1.1 Overview

The Wide-band All-sky Monitor (WAM, [Yamaoka et al. 2009](#)) is space-use scintillation counters to observe astrophysical objects in the 50 keV to 5 MeV bandpass, which is originally used for the active shield of the Hard X-ray Detector (HXD, [Takahashi et al. 2007](#)) on-board

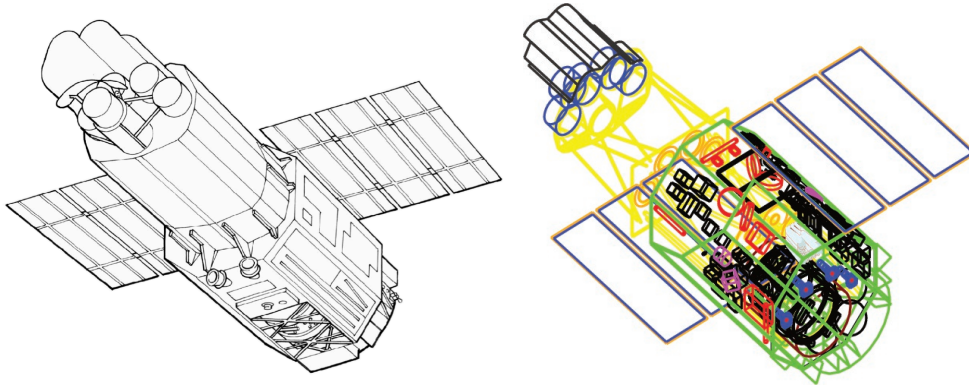


Figure 3.1: Left is schematic view of *Suzaku* satellite from Mitsuda et al. (2007). Right is a constructed Geant4 *Suzaku* geometry for generation of energy response matrix of the WAM (§3.1.4).

Suzaku satellite (Mitsuda et al. 2007). Figure 3.1 and 3.2 indicate schematic view of *Suzaku* and the WAM detector, respectively, and Table 3.1 summarize capabilities of the WAM. It comprises four walls (WAM-0, WAM-1, WAM-2 and WAM-3) of Bismuth Orthogermanate $\text{Bi}_4\text{Ge}_3\text{O}_{12}$ (BGO) crystal with a field of view of 2π steradian, covering a wide spectral range from 50 keV to 5 MeV and a large effective area reaching 400 cm^2 for 1 MeV photon, at launch. The four detectors are constructed as square cylinder and view each sky but through the spacecraft materials. The energy range and effective area are variable due to a long term gain drifts at the occasion, which is monitored every day by using the annihilation line from the radioactive nuclei induced by the particle activations during the passage of the SAA and incoming photon angle to the WAM. The angles of on-axis are defined with WAM-0 ($\theta = 90^\circ$, $\phi = 90^\circ$), WAM-1 ($\theta = 90^\circ$, $\phi = 0^\circ$), WAM-2 ($\theta = 90^\circ$, $\phi = 180^\circ$) and WAM-3 ($\theta = 90^\circ$, $\phi = 270^\circ$) (Yamaoka et al. 2009). Figure 3.3 shows definition of the angle.

The effective area is the largest among current gamma-ray spectrometers onboard astronomical satellites between 300 keV and 5 MeV energy band. Therefore the WAM has advantage to detect the soft gamma-ray photons of sub-MeV energy range among the current-active hard X-ray observatory. Exploiting those characteristics, the WAM make investigating classical GRBs and solar flares available (e.g., Endo et al. 2010; Tashiro et al. 2012; Urata et al. 2014).

The WAM produces two format data such as transient (TRN) data and gamma-ray

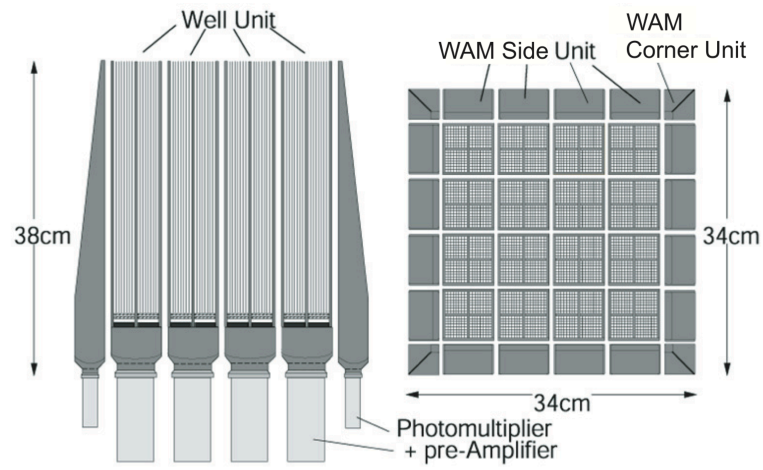


Figure 3.2: Schematic view of the HXD detector. Left and right panel show cross-sectional and top view, respectively (Yamaoka et al. 2009).

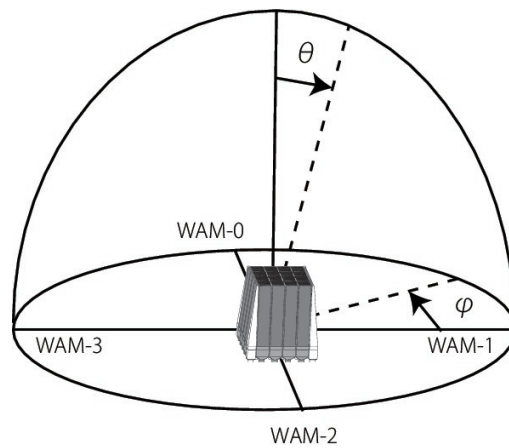


Figure 3.3: Definition of incident angle of photons to the WAM.

Table 3.1: Characteristics of *Suzaku*-WAM from [Yamaoka et al. \(2009\)](#)

Sensors	20 BGO crystals (readout by Photo-Multiplier Tube)
Number of detectors	4 (referred to as WAM-0, WAM-1, WAM-2 and WAM-3)
Energy range	50–5000 keV (55 energy channels)
Geometrical area	800 cm ² per side
Effective area @ 1 MeV	400 cm ² per side
Energy resolution @ 662 keV	~ 30%
Field of view	~ 2 π
Time resolution	1/64 s during 64 s of the burst (BST data) continuous 1 s (TRN data)
Telemetry rate	5 kbps
Response time to GRBs	within a day (no alerts)

burst (BST) data. TRN data is continuously accumulated with 1 s time resolution and 55 energy channels excepting during passage through the south atlantic anomaly (SAA). Sample of a calm day light curve of TRN data and geomagnetic cut-off rigidity (COR) are shown in Figure 3.4. We can see long term trend in an hour scale and data gaps in the TRN data. The former is caused by the fluctuation of the non X-ray background induced by the trapped charged particles in geomagnetic field of the Earth. Consequently, its background flux strongly depend on the COR value along *Suzaku* satellite orbit. The latter is due to passage through the SAA, then to protect the photomultiplier tube of the HXD the detector high voltage is turn-off by the operation. Whereas the BST data are recorded with 16 μ s time resolution and 4 energy channels (i.e., TH0, TH1, TH2 and TH3) for 64 s, and they are acquired only when a GRB activates onboard triggering system. Only one set of BST data can be stored in the on-board buffer before the spacecraft data recorder reads it out during passage through the SAA. After the readout, the on-board buffers become recordable again. Because of this limitation, we can obtain at most about ten BST data sets in a day, but we lose latter BST data if other bursts occur soon after recording is triggered. The individual four energy channels of the BST data correspond to 2–3, 4–7, 8–16 and 17–54 energy channel of TRN data. The absolute time accuracy of the both data is 320 μ s ([Terada et al. 2008](#)).

3.1.2 Electronics for WAM

Generated signals in photomultiplier tubes belong the BGO crystals are read out by four independent analog signal processing unit board (TPU). Main roles of the TPU are (1) hit

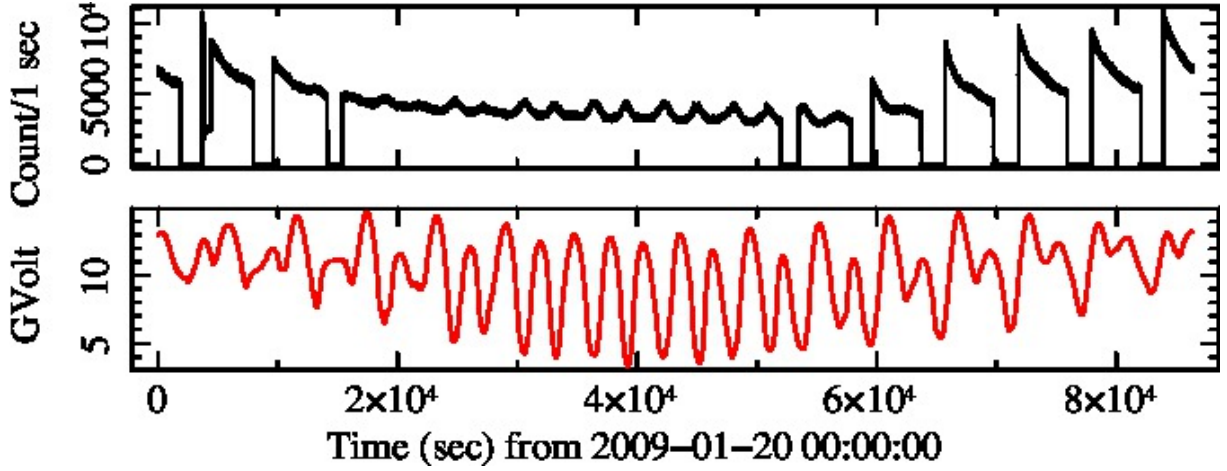


Figure 3.4: Light curves of one of calm days of the WAM on 2009 January 20. This day is calm and no astronomical event. Black line indicates 1 s count rate of 2–54 energy channel, and red line is electric voltage of COR in the orbit of *Suzaku*.

pattern sending to main HXD unit, (2) analog-to-digital signal conversion, (3) accumulation of the signals and produce the two types of histogram data (the BST and the TRN), (4) GRB detection, and (5) triggering safety functionality to turn off the detector high voltage (see detail [Yamaoka et al. 2009](#)). Figure 3.5 shows signal process flow in the TPU. First, (1) is work for anti-coincident detector of the HXD, it is called also “active shield”. Using obtained hit pattern information in the WAM, we can reduce background events due to ambient particles (e.g., high-energy electrons, protons, albedo neutrons), electron/positron pair creation and Compton scattering. Next, (2), (3), and (4) is abilities for all-sky monitor for sub-MeV energy photons. To trigger the WAM and produce the BST data effectually due to astronomical events such as classical GRBs, solar flares, and suddenly event like that magnetar burst, trigger criterion is defined as

$$S\Delta t - B_g\Delta t > \sigma\sqrt{B_g\Delta t}. \quad (3.1)$$

Here, S is the whole count rate including source and background component at any given time for sampling time Δt , B_g is average background count rate for 8s before the time of S , and σ is the significance level. The parameters of Δt (1/4 s, 1 s or both) and σ (5.7, 8.0, 11.2, or 16.0) are able to change after launch. Finally, (5) is work for a monitor of ambient particle to protect the HXD, especially radiation-belt like that of SAA. If count rates of the four corner units over 8 s reach a certain level, the high voltage is reduced automatically.

an Earth-occultation technique using Crab nebula spectra (Yamaoka et al. 2009). This uncertainty is included as systematic error of the response matrix.

3.1.4 Generating Energy Response Matrix

The response matrices of the WAM are complicated, depending on incident angle of photons. Since the WAM is inside the *Suzaku* satellite body, observed spectral shape and flux are affected by heavy absorption and scattered from it. In order to generate the response matrixes of the detectors, we used a Geant4-based Monte-Carlo simulation code (Ohno et al. 2005; Ozaki et al. 2006; Terada et al. 2005). In this code, *Suzaku* mass model is developed and represents size, component material, and these space distributions (Figure 3.1). The accuracy of the matrixes has been verified by in-orbit cross calibration using GRB spectra (Sakamoto et al. 2011b).

3.2 Other Instruments

We analyzed data taken by other X-ray and/or gamma-ray astronomical detectors achieve higher timing resolution observation or imaging localization of events on-board *Swift*, *Fermi*, and *INTEGRAL* satellites, in order to supplement higher time-resolution information than the WAM data and localization capability of individual events.

3.2.1 *Swift* Burst Alert Telescope

The burst alert telescope (BAT, Barthelmy et al. 2005) on-board *Swift* (Gehrels et al. 2004) is a hard X-ray instrument for astronomical use with very large field of view covering a hard X-ray range of 15–150 keV. The BAT has an imaging capability with the coded-mask technique. This energy range is valid for the imaging (and also for the background subtraction technique by the weighting mask method). The BAT consists of 32,768 pieces of 4.00 mm square 2.00 mm thick CdZnTe detector elements, Pb tiles coded-aperture mask and fringe shield covering side wall between the mask and the detector plane and under the detector plane (Barthelmy et al. 2005). Its observational capabilities are listed in Table 3.2. It is a powerful detector to catch the initial detections of classical gamma-ray bursts (GRBs) and localizes the position with 4 arcmin accuracy. Currently, for only five years the BAT successfully

Table 3.2: Characteristics of *Swift*-BAT from [Barthelmy et al. \(2005\)](#)

Energy range	15–150 keV
Energy resolution	~ 7 keV
Aperture	Coded mask, random pattern, 50% open
Detecting area	5240 cm ²
Detector material	CdZnTe
Detector operation	Photon counting
Field of view	1.4 str (half-coded)
Detector elements	256 Modules of 128 elements/module
Detector element size	4.00 × 4.00 × 2.00 mm ³
Coded mask cell size	5.00 × 5.00 × 1.00 mm ³ Pb tiles
Instrument dimensions	2.4 m × 1.2 m × 1.2 m
Telescope PSF	17 arcmin
Source position accuracy	1–4 arcmin
Sensitivity	$\sim 10^8$ erg cm ⁻²
Number of bursts detected	> 100 year ⁻¹

detected at least 476 GRBs ([Sakamoto et al. 2008, 2011a](#)). Therefore the BAT is suitable also for observations of transient astronomical phenomena like AXP and SGR bursts. If the BAT finds a significant bright source with the on-board software automatically, the photon-by-photon data with 100 μ s time resolution are produced and stored. The duration of the data covers 300 s before to 300 s after until 2006 March 17, and 300 s before to 1000 s after to date. Whereas, when the trigger is not activated, the BAT performs observation with survey mode, which provides typically 5 minutes accumulated data.

3.2.2 *Swift* X-ray Telescope

The X-ray telescope (XRT, [Burrows et al. 2005](#)) system on-board *Swift* is a sensitive autonomous X-ray imaging spectrometer. The XRT consists of Wolter I type X-ray telescope mirror and an X-ray charge-coupled device (CCD) camera on the focal plane. [Table 3.3](#) summarizes properties of the XRT. When the BAT is triggered by an astronomical object like GRB, *Swift* satellite immediately change its attitude to put the object into the XRT field of view automatically, to perform sensitive deep follow-up observation. A combination with the BAT and the XRT provide us useful imaging, temporal, and spectral data in the broadband energy range (0.1–150 keV).

Table 3.3: Characteristics of *Swift*-XRT taken from [Burrows et al. \(2005\)](#)

Telescope	Wolter I (3.5 m focal length)
Detector	e2v technologies CCD-22
Detector format	600 × 600 pixels
Pixel size	40 μm × 40 μm
Pixel scale	2.36 arcseconds/pixel
Field of view	23.6 × 23.6 arcminutes
Point spread function	18 arcseconds (half power diameter) @ 1.5 keV 22 arcseconds (half power diameter) @ 8.1 keV
Position accuracy	3 arcseconds
Readout modes	Image (IM) mode Photodiode (PD) mode Windowed Timing (WT) mode Photon-Counting (PC) mode
Time resolution	0.14 ms, 1.8 ms, or 2.5 s
Energy range	0.2–10 keV
Energy resolution	140 eV @ 5.9 keV (at launch)
Effective area	~ 125 cm ² @ 1.5 keV ~ 20 cm ² @ 8.1 keV
Sensitivity	2 × 10 ⁻¹⁴ erg cm ⁻² s ⁻¹ in 10 ⁴ seconds
Operation	Autonomous

The XRT produce four types of data in different mode; image (IM) mode, photodiode (PD) mode, Windowed (WD) mode, and photon-counting (PC) mode. The IM mode produces image data with collecting the accumulated charge without any X-ray event recognition. The IM mode can be utilized for source fluxes between 25 mCrabs and at least 45 Crabs, and it provide accurate position determination and good flux estimation. The PD mode provides fast timing resolution (0.14 ms) data but without imaging information, and this is useful to extremely bright source up to 60 Crabs. The WT mode data have one dimension image information and 1.8 ms time resolution. Grand-processed data products are list of one dimension position, arrival time, energy, and event grade pattern of X-ray event-by-event. Finally, the PC mode provides data of full imaging and spectroscopic resolution, but 2.5 s time resolution. It is useful to weak source below 1 mCrab.

3.2.3 *Fermi* Gamma-ray Burst Monitor

Gamma-ray burst monitor (GBM, Meegan et al. 2009) on-board *Fermi* satellite is a similar system to the WAM, which is used for the entire sky monitor comprised by 2 BGO and 12 NaI scintillation detectors. The BGO crystals have a cylinder shape with 12.7 cm diameter and length, and two photomultiplier tubes are attached to the both plane sides. They are placed at opposite sides of the spacecraft. The NaI scintillators cover lower energy range of 8 keV–1 MeV than the BGO scintillators. The NaI crystals are formed of disk of a diameter of 12.7 cm and a thickness of 1.27 cm. Axes of the field of view of each the NaI detector face different directions. The major difference from the WAM is that the GBM crystals face the deep space directly and thus no complex absorptions by the spacecraft like in the WAM case occur in GBM system. Therefore GBM flight software is able to determine position of triggered events approximately in orbit by comparing the relative count rates of a dozen detectors with expected ones. This method archives position accuracy of 8° for on-board analysis, and approximately 4° by off-line analysis on ground (von Kienlin et al. 2014). Successive GBM trigger and localize information are archived¹. According to GRB catalog of the GBM (Gruber et al. 2014; von Kienlin et al. 2014), at least 954 GRBs detected for 4 years.

The GBM outputs three data type of the CTIME, CSPEC, and time-tagged event (TTE) data. The first two data are continuously recorded with 256 ms time resolution and 8 energy channels (CTIME), and 4 s and 128 energy channels (CSPEC). When the GBM

¹http://gcn.gsfc.nasa.gov/swift_grbs.html

trigger is activated, these time resolution is increased to 64 ms and 1 s, respectively, for 600 s. Then the TTE data are produced from individual all 14 GBM detectors, which have high temporal of $2\ \mu\text{s}$ and spectral of 128 energy channels resolution.

3.2.4 *INTEGRAL* Anti-Coincidence System

The anti-coincidence system (ACS, [von Kienlin et al. 2003](#)) on board *INTEGRAL* satellite ([Winkler et al. 2003](#)) is an active shield of *INTEGRAL* spectrometer (SPI, [Vedrenne et al. 2003](#)). The main task of the ACS is rejection of background events like that of the WAM. The ACS comprises 91 BGO crystals, and its total mass is 512 kg. The thickness of the individual crystals are from 16 to 50 mm. Thanks to the heavy materials, an effective area of the ACS is the largest among current astronomical photon counting detectors (e.g., [Mereghetti et al. 2005](#)), and a large number bursts are detected (GRB catalogue [Rau et al. 2005](#)). Although the ACS has no imaging capability and no energy information is measured, it provides us higher time-resolution data than the WAM TRN data between 80 keV and 8 MeV energy range. The observed light curves are archived and published in Heavens archive².

²<http://isdc.unige.ch/heavens/>

Chapter 4

Observation and Data Reduction

Contents

4.1	Observation of Bursts from AXP 1E 1547.0–5408 with WAM	45
4.2	Observations with Other Instruments	48
4.2.1	Observation with <i>Swift</i> BAT and XRT	48
4.2.2	Observation with <i>Fermi</i> GBM	50
4.2.3	Observation with <i>INTEGRAL</i> ACS	50

4.1 Observation of Bursts from AXP 1E 1547.0–5408 with WAM

On 2009 January 22, [Gronwall et al. \(2009\)](#) first reported burst activities from AXP 1E 1547.0–5408. On the same day, *Suzaku*-WAM had succeeded to record a series of bright burst like events. Figure 4.1 shows three band light curves of WAM-0 during this activity (observational ID = 703049010, covering UTC January 19 23:30:36–22 18:41:42). The light curves after dead-time corrections are extracted, using `hxdmkwam1c` which is a standard FTOOLS included in the HEADAS software package version 6.14¹. We can see a large number of bright bursts for ~ 16 hours surpassing the COR fluctuation. These light curves are employed on burst detection in following §5.1.1. In addition, we exhibited a 70 keV–6.2 MeV energy band light

¹<http://heasarc.nasa.gov/lheasoft/>

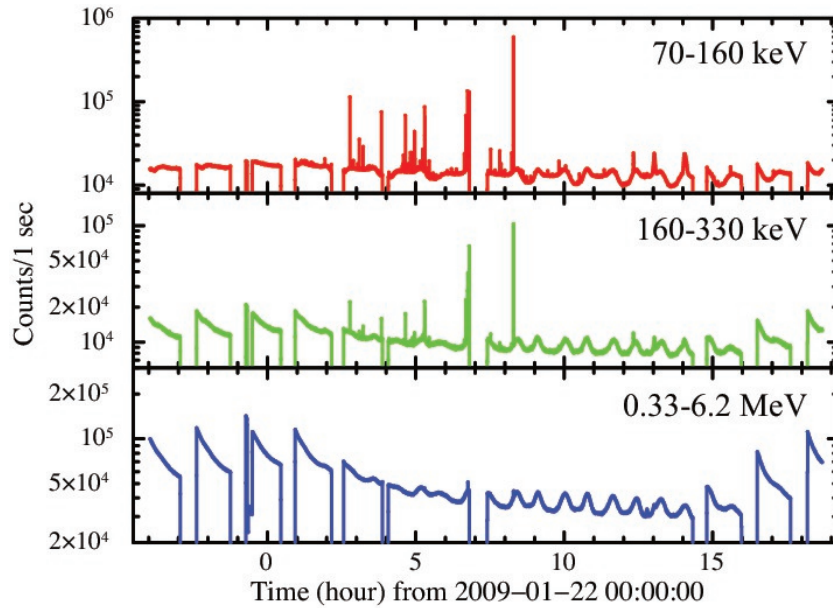


Figure 4.1: *Suzaku*/WAM-0 TRN light curves after dead-time correction on 2009 January 22. Red, green and blue lines indicate each energy channel; 2–3, 4–7 and 8–54 channel corresponding to 70–160 keV, 160–330 keV and 0.33–6.2 MeV in the day using the location of AXP 1E 1547.0–5408.

curve in Figure 4.2 to compare it with other instrument data. As described in §3.1.1, in the light curves, the long term trend in an hour scale and the data gaps are normally seen in the light curves of a calm days (Figure 3.4). A data gap between UTC 06:48:07 and 07:24:14 is not caused by the SAA but the safety function (radiation belt monitor; RBM) on-board by which the high voltage of the photomultiplier tube is set to be 0 volt when the count rate of the corner counter of the WAM exceeds the threshold. The RBM is activated on UTC 06:48:04 by the brightest bursts, actually it is reported as the highest fluence event also by the ACS during this data (Mereghetti et al. 2009b). Conclusively, exposure of the TRN data without WAM power-off intervals is 66 ks.

During the activity, 5 events were stored in the BST data format. The trigger times are UTC 01:28:59.790, 02:46:56.290, 04:34:52.789, 15:10:35.284 and 17:02:56.283. Moreover, after about 29.6 s from the trigger time at 04:34:52.789, significant bright another burst is confirmed by the off-line analysis of the TRN data. Figure 4.3 shows the six light curves with four energy ranges. T_{90} duration, which is the time to accumulate between 5% and 95% of the counts, of the events were distributed from 0.13 s to 2.0 s. Table 4.1 summarizes the trigger times and the T_{90} durations. The trigger information has been reported in the

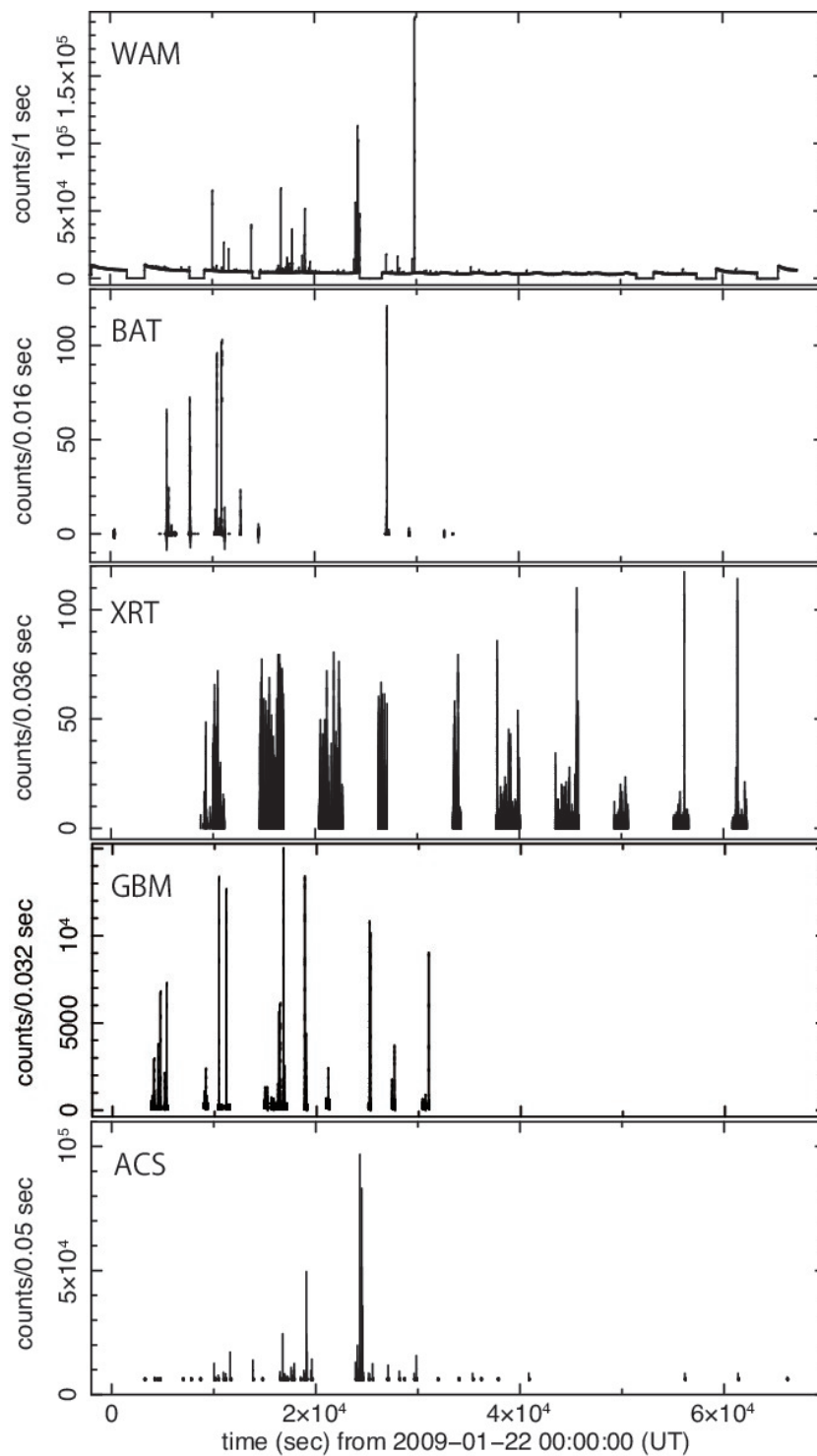


Figure 4.2: Comparison of light curves of five instruments. The light curves of the WAM, the XRT, the GRB and the ACS still include background components, but background component of the BAT light curve is subtracted.

astronomer’s telegram (ATel #1906: [Terada et al. 2009a](#)) and in the gamma-ray coordinate network (GCN, [Terada et al. 2009b](#)), immediately after the detection.

Table 4.1: Trigger Time of BST data from [Terada et al. \(2009a\)](#)

Time (UTC)	T90 duration (s)
2009-01-22	
01:28:59	0.14
02:46:56	1.5
04:34:52	0.41 (the first event)
	2.0 (the second event including its precursor)
15:10:34	0.13
17:02:55	0.36

4.2 Observations with Other Instruments

4.2.1 Observation with *Swift* BAT and XRT

The *Swift* satellite is particularly suited to supplement the non-imaging WAM data. Especially trigger data of the BAT and WD data of the XRT provide us the target localization information of burst-by-burst and high time-resolution temporal information of photon-by-photon. We utilized 16 BAT trigger data (including failed trigger data) and 2 XRT WT mode data sets observed on 2009 January 22, and obtained its from HEASARC data archive². Table 4.2 summarizes the datasets we employed in this thesis.

On the data reduction of the *Swift* data, we retrieved the pipeline products and processed the XRT data using `xrtpipeline`, and utilized `batmaskwtevt` to compute mask weight for the BAT data. Then we utilized latest calibration data base CALDB³ as of the XRT at 2014 July 9 and the BAT at 2009 January 30, and inputted the location of AXP 1E 1547.0–5408, R.A. (J2000) 15^h50^m54^s.12 and Decl. (J2000) $-54^{\circ}18'24''.11$ ([Camilo et al. 2007](#)). We defined source region of a circle with radius 40 pixels on the image of the WT data. Next, for the extractions of light curves, `xselect` and `batbinevt` are used for the XRT and the BAT, respectively. These useful tools and software are standard FTOOLS⁴ and standard *Swift*

²<http://heasarc.gsfc.nasa.gov/cgi-bin/W3Browse/swift.pl>

³http://heasarc.gsfc.nasa.gov/docs/heasarc/caldb/caldb_intro.html

⁴<http://heasarc.gsfc.nasa.gov/ftools/>

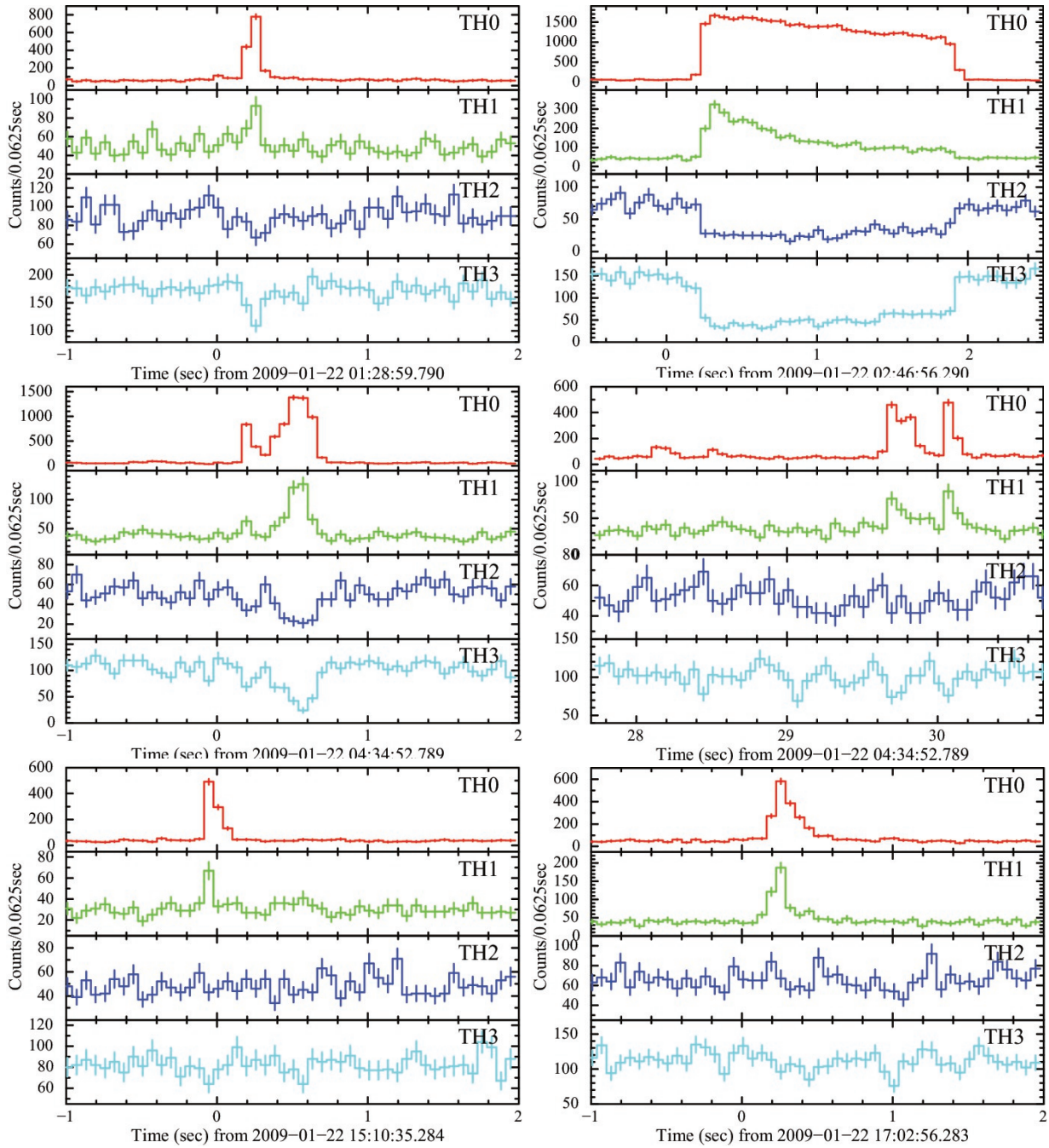


Figure 4.3: Six high-time resolved *Suzaku* WAM-0 light curves from five BST data without dead-time correction. Top Left, top right, middle left, middle right, bottom left and bottom right correspond to occurrences time of ID number 45, 71 and 72, 154, 157, 575, and 578 in Table B.1, respectively. Since the light curves have not been corrected with the dead-time, count rate of the high-energy bands (TH2 and TH3) are decreased below background level. Its correction tool and information have not been published officially,.

software in HEADAS software package version 6.14. Figure 4.2 shows also the BAT light curves with 16 ms binning and the XRT ones with 36 ms binning. Total good time intervals are 15 ks (XRT) and 3.2 ks (BAT).

Both *Suzaku* and *Swift* take similar orbital elements in semi-circular low Earth orbit (LEO) with an apogee of about 570 km. Therefore if the same burst would be detected in individual detectors, arrival time difference of the photons between the two satellites is similar than 46 ms, which is calculated from time of flight of photons, since the time for both satellites report the arrival time to the spacecraft (not on geocentric time etc.). According to Yamaoka et al. (2009), correction accuracies of the time of light are verified as 0 ± 111 ms and -2 ± 36 ms using 15 classical GRBs and only bright 3 GRBs, respectively. Although these values are comparable, its are significantly small than the time-resolution of the TRN data. Therefore in this thesis, we do not consider the time different between *Suzaku* and *Swift* following analysis and discussion.

4.2.2 Observation with *Fermi* GBM

For *Fermi*-GBM data, we got GBM trigger data from the public *Fermi* FTP sever⁵. To extract GBM light curves from 24 TTE data of the NaI detectors, we used `gtbin`, which is included in *Fermi* Science Tools package version v9r32p5-fssc-20130916. Figure 4.2 shows also the GBM light curves with 64 ms binning. Since the *Fermi* satellite changes its attitude by time, reliable detectors are difference from burst to burst. Therefore we used two highest count rate data sets of 12 data sets of the NaI detectors at the burst, and accumulate the both light curves together to get good statistics. In the following analysis, we applied the accumulated data as the GBM light curves. Because the *Fermi* also takes LEO like *Swift* and *Suzaku*, we ignored the time lag between *Suzaku* and *Fermi*.

4.2.3 Observation with *INTEGRAL* ACS

The ACS light curve is useful to get finer temporal information of bursts detected by the WAM, because it provides a high-time-resolution (50 ms) light curve in the similar energy band (80 keV–8 MeV) to that of the WAM (70 keV–6.2 MeV), although the ACS has no energy information about each photon. We utilized all 67 trigger data observed on 2009

⁵<http://heasarc.gsfc.nasa.gov/FTP/fermi/data/gbm//triggers>

January 22 for the following analyses. Figure 4.2 shows also the ACS light curves. In the ACS light curves, estimation of the time difference between *Suzaku* and *INTEGRAL* is not negligible, because *INTEGRAL* satellite takes a highly elliptical orbit of attitude from 9,000 km to 153,000 km. Therefore we calculated the time of flight in data-to-data as summarized in Table 4.2, and shifted the time of the individual ACS light curves.

Sequence ID	Observation date (UTC)		TOF ^a (sec)	Sequence ID	Observation date (UTC)		Exposure (sec)	TOF ^a (sec)
	Start time	Stop time			Start time	Stop time		
2009-01-22.01:14:46	01:15:08.937	01:18:01.737	-0.443	2009-01-22.05:26:52	05:27:14.946	05:30:07.746	173	-0.412
2009-01-22.01:18:42	01:19:04.937	01:21:57.737	-0.444	2009-01-22.06:38:26	06:38:48.949	06:41:41.749	173	-0.414
2009-01-22.01:56:13	01:56:35.938	01:59:28.739	-0.442	2009-01-22.06:38:27	06:38:49.949	06:41:42.749	173	-0.414
2009-01-22.02:09:26	02:09:48.939	02:12:41.739	-0.434	2009-01-22.06:41:01	06:41:23.949	06:44:16.749	173	-0.412
2009-01-22.02:24:32	02:24:54.939	02:27:47.740	-0.429	2009-01-22.06:41:02	06:41:24.949	06:44:17.749	173	-0.412
2009-01-22.02:46:55	02:47:17.940	02:50:10.740	-0.433	2009-01-22.06:43:05	06:43:27.949	06:46:20.749	173	-0.411
2009-01-22.02:49:00	02:49:22.940	02:52:15.741	-0.434	2009-01-22.06:44:36	06:44:58.949	06:47:51.749	173	-0.410
2009-01-22.02:54:01	02:54:23.941	02:57:16.741	-0.436	2009-01-22.06:47:36	06:47:58.949	06:50:51.750	173	-0.408
2009-01-22.03:02:29	03:02:51.941	03:05:44.741	-0.438	2009-01-22.06:49:48	06:50:10.950	06:53:03.750	173	-0.407
2009-01-22.03:02:31	03:02:53.941	03:05:46.741	-0.438	2009-01-22.06:59:35	06:59:57.950	07:02:50.750	173	-0.401
2009-01-22.03:05:48	03:06:10.941	03:09:03.741	-0.439	2009-01-22.07:05:54	07:06:16.950	07:09:09.750	173	-0.398
2009-01-22.03:05:50	03:06:12.941	03:09:05.741	-0.439	2009-01-22.07:05:56	07:06:18.950	07:09:11.750	173	-0.398
2009-01-22.03:13:31	03:13:53.941	03:16:46.741	-0.439	2009-01-22.07:30:06	07:30:28.951	07:33:21.751	173	-0.398
2009-01-22.03:13:33	03:13:55.941	03:16:48.741	-0.439	2009-01-22.07:31:13	07:31:35.951	07:34:28.751	173	-0.399
2009-01-22.03:14:00	03:14:22.941	03:17:15.741	-0.439	2009-01-22.07:31:15	07:31:37.951	07:34:30.751	173	-0.399
2009-01-22.03:50:36	03:50:58.943	03:53:51.743	-0.423	2009-01-22.07:49:38	07:50:00.952	07:52:53.752	173	-0.405
2009-01-22.03:50:38	03:51:00.943	03:53:53.743	-0.423	2009-01-22.07:49:40	07:50:02.952	07:52:55.752	173	-0.405
2009-01-22.04:05:45	04:06:07.943	04:09:00.743	-0.419	2009-01-22.07:57:29	07:57:51.952	08:00:44.752	173	-0.405
2009-01-22.04:34:51	04:35:13.944	04:38:06.745	-0.428	2009-01-22.08:13:49	08:14:11.953	08:17:04.753	173	-0.401
2009-01-22.04:34:53	04:35:15.944	04:38:08.745	-0.428	2009-01-22.08:13:50	08:14:12.953	08:17:05.753	173	-0.401
2009-01-22.04:39:03	04:39:25.945	04:42:18.745	-0.429	2009-01-22.08:17:27	08:17:49.953	08:20:42.753	173	-0.399
2009-01-22.04:39:04	04:39:26.945	04:42:19.745	-0.429	2009-01-22.08:17:29	08:17:51.953	08:20:44.753	173	-0.399
2009-01-22.04:42:03	04:42:25.945	04:45:18.745	-0.429	2009-01-22.08:52:24	08:52:46.954	08:55:39.754	173	-0.382
2009-01-22.04:45:10	04:45:32.945	04:48:25.745	-0.430	2009-01-22.09:26:37	09:26:59.956	09:29:52.756	173	-0.391
2009-01-22.04:46:56	04:47:18.945	04:50:11.745	-0.430	2009-01-22.09:49:28	09:49:50.957	09:52:43.757	173	-0.386
2009-01-22.04:53:15	04:53:37.945	04:56:30.745	-0.429	2009-01-22.10:03:04	10:03:26.957	10:06:19.757	173	-0.378
2009-01-22.04:57:17	04:57:39.945	05:00:32.745	-0.428	2009-01-22.10:30:37	10:30:59.958	10:33:52.758	173	-0.367
2009-01-22.04:57:19	04:57:41.945	05:00:34.745	-0.428	2009-01-22.11:20:56	11:21:18.960	11:24:11.760	173	-0.372
2009-01-22.05:08:26	05:08:48.946	05:11:41.746	-0.422	2009-01-22.15:35:53	15:36:15.971	15:39:08.771	173	-0.314
2009-01-22.05:14:02	05:14:24.946	05:17:17.746	-0.419	2009-01-22.17:02:56	17:03:18.974	17:06:11.774	173	-0.289
2009-01-22.05:14:04	05:14:26.946	05:17:19.746	-0.419	2009-01-22.18:22:56	18:23:18.977	18:26:11.778	173	-0.266
2009-01-22.05:17:41	05:18:03.946	05:20:56.746	-0.417					

a: Corrected time of flight.

Chapter 5

Analysis and Results

Contents

5.1	Temporal Analysis	56
5.1.1	Burst Detections with the WAM	56
5.1.2	Search for WAM Bursts Simultaneously Detected with Other Instruments	56
5.1.3	Estimation of Incident Angles of Bursts by the WAM	57
5.1.4	Correlation Searches from WAM Selected Bursts	61
5.2	Preparations for Spectral Analysis	64
5.2.1	Response Matrixes Generation	64
5.2.2	Data Selection	65
5.2.3	Development of Pile-up Simulator	65
5.3	Spectral Analysis	67
5.3.1	Individual Spectral Fitting	67
5.3.2	Results on Bright Bursts	70

5.1 Temporal Analysis

5.1.1 Burst Detections with the WAM

To extract the bursts from the TRN light curves (e.g., Figure 4.1), since the background count rates have long time-scale modulation along with the changes of COR by the orbit of ~ 90 minutes intervals, we try to pick-up shorter time-scale flare-up events by the detection criteria as

$$C_s - \frac{C_b}{t_b} > \sigma \frac{\sqrt{C_b}}{t_b}, \quad (5.1)$$

where t_b , C_s , C_b and σ are sampling time of background component, source count rate value at a given time bin, background count for the sampling time t_b and significant level, respectively. This algorithm is used also for the detection in orbit for the WAM, which is originally developed for *Ginga* satellite. We set $t_b = 8$ s and $\sigma = 5.0$, and searched bursts from the light curves in the 70–160 keV, 160–330 keV, and 330–6200 keV energy bands (red, green, and blue lines in Figure 4.1, respectively). If a burst (or bursts) detected by the previous searches during the background interval of t_b , we ignore the time bins and instead assign previous bins of the time interval. This function is does not exist in the on-board software but is adapted especially to this analysis of AXP 1E 1547.0–5408. Consequently, 568, 413, 89 and 85 time bins were successfully detected as flare up events by the WAM-0, WAM-1, WAM-2 and WAM-3 respectively, in the lower energy range. In the higher two energy range, 110, 86, 26, and 24 time bins in the medium energy range and 19, 13, 1, and 1 time bins in the higher energy range were detected, respectively. WAM-0 and WAM-1 count rate values without background components of all detected time bins are listed in Table B.1.

5.1.2 Search for WAM Bursts Simultaneously Detected with Other Instruments

To know detailed temporal information of the WAM detected bursts (Table B.1), other instrument data are useful in the sense of time resolution (§3.2). In addition, the imaging capabilities of the *Swift*/BAT and the XRT are important to enhance the evidence whether

the non-imaging detector WAM detected bursts are from AXP 1E 1547.0–5408 or not in §5.1.3. We therefore searched for the simultaneous bursts in light curves by *Swift*, *Fermi*, *INTEGRAL* (§3.2), which are summarized in Figure 4.2.

The GBM light curves with 64 ms time binning show a slow variation due to the changes of the attitude of the satellite, we used same method and same criteria with the WAM: i.e., 8 s background integration and 5.0σ significant level (§5.1.1). As a result, a dozen of NaI GBM detectors detected 183 time bins on average. For other three detectors, in order to detect statistically-significant-bright time bins we have studied distribution of the count rates in the light curves of Figure 4.2. We calculated histograms of count rate and performed fitting with Gaussian functions to the BAT and the ACS data and Poisson function to the XRT data as demonstrated in Figure 5.1. The histograms of the BAT and the ACS are produced with respect to each trigger data, and then noisy intervals are ignored by hand. We made ten histograms from XRT light curves separated by SAA regions. Detection criteria are defined as 5.0σ significant levels from the mean of the fitted Gauss functions, and probability of less than 0.1% of the Poisson functions. In equation, the probability P_i of the number of counts in each time bin n_i is written by

$$P_i = \frac{\lambda^{n_i} e^{-\lambda}}{n_i!}, \quad (5.2)$$

where λ is mean counts of the Poisson function, and the criteria mean $P_i < 0.001/N$ where N is total number of the time bins in the histogram.

If the time bins of the other instruments are significantly above the detection criteria with above methods and its times are within any detected WAM 1 s time bins, we define these events as simultaneous bursts. Table B.1 also shows simultaneous information.

5.1.3 Estimation of Incident Angles of Bursts by the WAM

Since the WAM has no imaging capability, we are not able to determine incoming directions of photon-by-photon. But the count rate ratio between WAM-0 and WAM-1 geometrically provides the information the incident angle of irradiating photons. Here we examine the ratio of count rates between WAM-0 and WAM-1 for the bursts detected by both sides in 2–3 energy channels (corresponding to 70–160 keV) to check consistency with the assumption that they are from AXP 1E 1547.0–5408. Figure 5.2 represents two histograms of the count rate ratio; one is the distribution of simultaneous events whose origin is confirmed to be

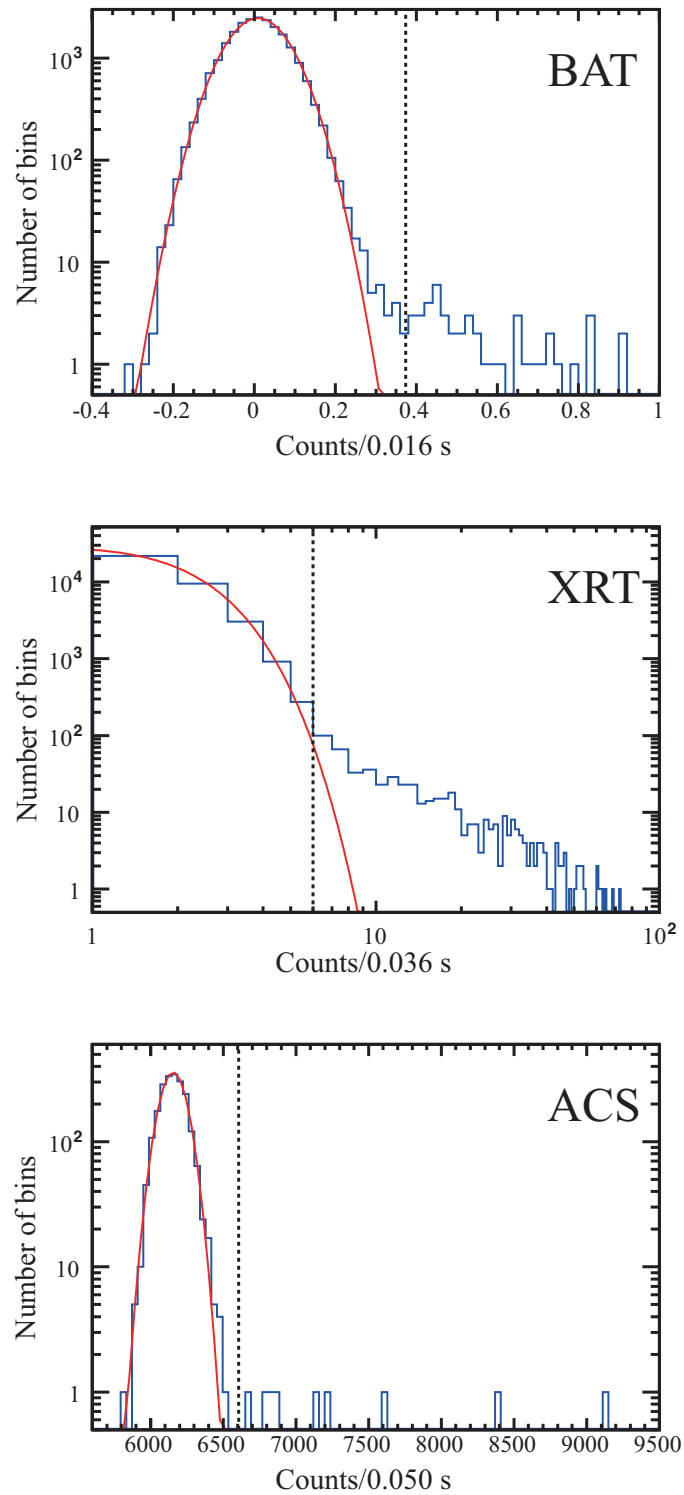


Figure 5.1: Samples of count rate histogram (solid lines) of three detectors, the BAT, the XRT and the ACS. Red lines indicate best-fit Gauss distributions (BAT and ACS) and Poisson distribution (ACS), and vertical dotted lines are threshold of detection.

AXP 1E 1547.0–5408 with *Swift* and another is that of others. They follow lognormal Gaussian shapes well, with the mean values of 0.24 ± 0.01 and 0.23 ± 0.01 , and sigma of 0.07 ± 0.01 and 0.07 ± 0.01 , for simultaneous and the other events respectively. These resemble parameters indicate the two distributions are statistically consistent. Thus, this distribution indicates that non-simultaneous event also come from the object. In comparison, the expected ratio of count rates can be calculated from the target position we assume (i.e., AXP 1E 1547.0–5408) and the energy response function of the WAM detectors by the Monte-Carlo Geant4 simulation with *Suzaku* mass model. According to the location of the object by Deller et al. (2012), and the attitude of the satellite, the incident angles from the object to the WAM are zenith angle $\theta = 59.9^\circ$ and azimuthal angle $\phi = 51.4^\circ$. This requires the count rate ratio of $0.09^{+0.15}_{-0.24}$ in lognormal frame, where quoted errors are estimated from the systematic error in effective areas of WAM response matrix at 30% (Yamaoka et al. 2009). As a result, the observed ratios of count rates are both consistent with the expected value with the assumption that the signals come from AXP 1E 1547.0–5408 within the systematic errors. We also checked the GRB Coordinate Network circular¹ and archive of solar flares², and confirmed that there were no reports of other astronomical transient events in the same period. We therefore defined the following conditions to determine whether the events came from AXP 1E 1547.0–5408 or not.

- It should be detected in both WAM-0 and WAM-1 sides at least in 70–160 keV band.
- Count rate ratio between the two sides should be within 4 sigma level from mean value from the fitted Gaussian.

Numerically, 404 time bins in the WAM light curves are selected as safe events coming from the object and 3 bins are not. 109 and 17 time bins of the 404 time bins are detected also in 160–330 keV and 0.33–6.2 MeV range (§5.1.1). We consider that the reason why the three events are outside of the distribution to due to that the two events (observational ID 64 and 363 in Table B.1) are too weak and the last one is too as bright as saturation occurs in the WAM-0. The results are listed in Table B.1. Hereafter, we used these 404 events for the incoming analysis. Figure 5.3 shows a time history of above detected events. Integrated count rates is 1.8×10^6 counts.

¹http://gcn.gsfc.nasa.gov/gcn3_archive.html

²http://www.lmsal.com/solarsoft/latest_events_archive.html

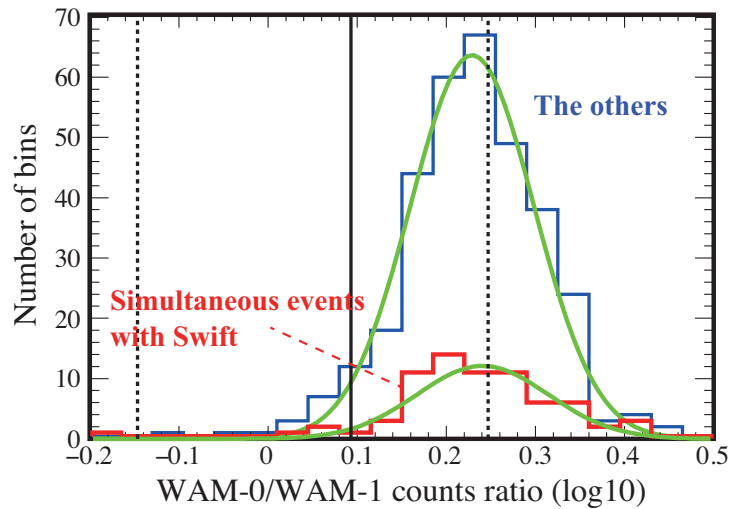


Figure 5.2: Histogram of WAM-0/WAM-1 count rate ratio of detected events in 70–160 keV band in both sides, then used count rate values are corrected with dead-time and listed in Table B.1. Blue and red are simultaneous events with *Swift* and not ones, respectively. Green curved lines are best-fit Gauss functions in log-normal space. Vertical lines indicate expected count rate ratio from direction of AXP 1E 1547.0–5408 (solid lines) and its systematic error of 30% (dotted lines).

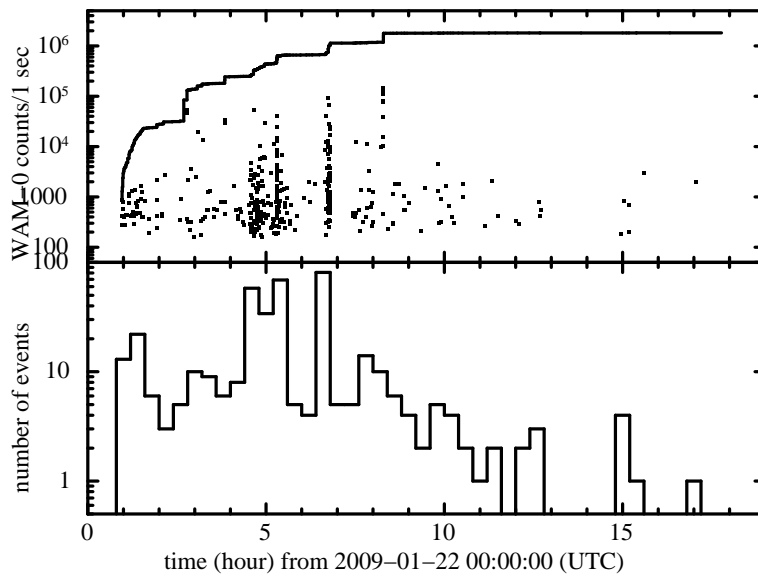


Figure 5.3: Time history of detected events by WAM-0, which are defined as emitted from AXP 1E 1547.0–5408 in §5.1.3. The count rate values are in 70–160 keV (2–3 ch) energy range. The step line in upper panel indicates integrated count rate values.

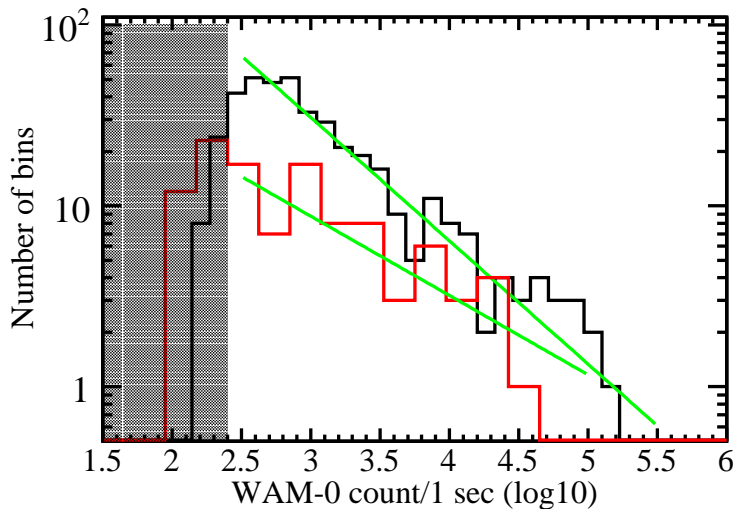


Figure 5.4: WAM-0 count rate histograms of detected events in the two band of 70–160 keV (black) and 160–330 keV (red). Hatched areas indicate detection thresholds. Green lines are best-fit power-law functions. Plotted points are defined as bursts from AXP 1E 1547.0–5408 in §5.1.3. Hatched area indicates detection threshold. The thresholds of the two energy bands are comparable.

5.1.4 Correlation Searches from WAM Selected Bursts

Thanks to the large effective area of the WAM, this allows us to see various bright bursts in broad dynamic range of three orders of magnitude. Figure 5.4 shows count rate distribution with dead-time correction of the 404 time bins selected above (§5.1.3). The two histograms are represented by simple power-law functions with slope indexes -0.7 ± 0.1 for higher-energy range and -0.4 ± 0.1 for lower-energy range, where the quoted errors indicate 68.3% level. Its slope indexes are similar with *INTEGRAL* ACS observation (Savchenko et al. 2010) in same day of same object; reported indexes values of peak count rate and fluence distribution are -0.8 ± 0.2 and -0.5 ± 0.1 , respectively.

Figure 5.5 shows distribution of waiting time T_{waiting} , which is time difference between detected times of event-by-event, in two energy bands in WAM-0. Where if two or more time bins are continuously detected, we selected only first time bins. Then we ignored six time bins that calculated waiting times are with in SAA region or HXD off intervals. In the scatter panel (left panel of Figure 5.5), we cannot significant correlation between burst brightness of initial pulse and the waiting times. We fitted the two distributions in histogram space (right panel of Figure 5.5) using lognormal Gauss functions, and yielded

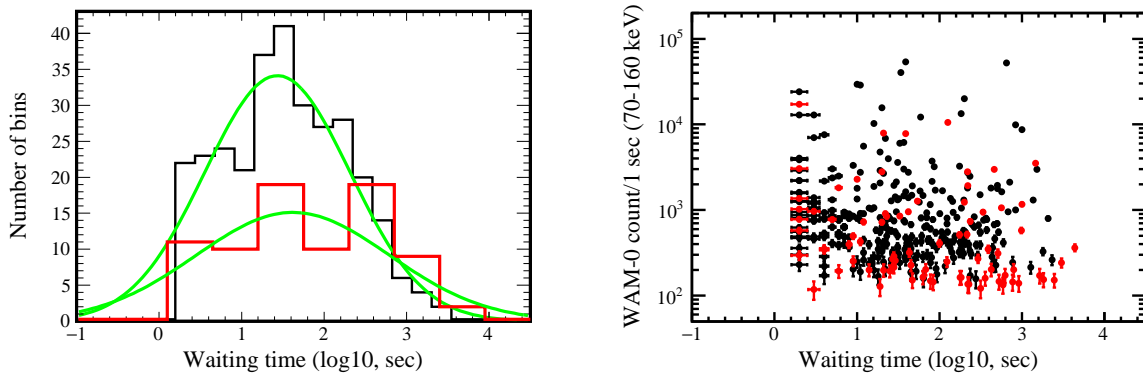


Figure 5.5: Histograms and scatter plot of waiting time of detected events in the two band of 70–160 keV (black) and 160–330 keV (red). In the left panel, green lines are best-fit lognormal Gauss functions. Plotted points are defined as bursts from AXP 1E 1547.0–5408 in §5.1.3.

mean and standard deviation values are 1.43 ± 0.08 and 0.88 ± 0.07 for 70–160 keV range and 1.62 ± 0.23 and 1.17 ± 0.20 for 160–33-keV range in lognormal space, respectively. These values mean that the waiting times are distributed with $3.2 \text{ s} < T_{\text{waiting,soft}} < 200, \text{ s}$ and $2.5 \text{ s} < T_{\text{waiting,hard}} < 631 \text{ s}$ in normal space. It is absence of short waiting time distribution ($1 \text{ s} < T_{\text{waiting}} < 10 \text{ s}$) in the histograms that a possible is strongly due to selection bias in §5.1.2 and §5.1.3. We therefore examined the lognormal Gauss fitting to all detected time bins without via the selection. In consequence, yielded parameters of a mean value (1.33 ± 0.06) and a sigma (0.82 ± 0.05) for low-energy band and (1.62 ± 0.23 and 1.14 ± 0.18) for high-energy band are comparable with the results of selected bins. Another candidate is the selection bias with burst detection criteria, and there is no significant relation between the waiting time and burst brightness (Figure 5.5 left panel). Thus we can consider the lognormal distributions are intrinsic phenomenon of AXP 1E 1547.0–5408. Although utilized TRN data are 1 s time resolution, the waiting times are comparable with 50 ms time resolved ACS observation (Savchenko et al. 2010) of $2.3 \text{ s} < T_{\text{waiting}} < 465 \text{ s}$.

Figure 5.6 shows scatter plot of count rates between 70–160 keV and 160–330 keV, and 70–160 keV and 0.33–6.2 MeV band, and hardness diagram (i.e., count rate ratio between in 70–160 keV and 160–330 keV, and 70–160 keV and 0.33–6.2 MeV energy range). In the hardness plot, absent of points of lower count rate and lower hardness ratio is considered to be due to a bias from detection criteria. Although the correlation (hardness ratio \propto fluence) in short bursts from 1E 2259+586 (Gavriil et al. 2004) and (hardness ratio \propto count rate) in 1E 1547.0–5408 Savchenko et al. (2010) are reported, here is no significant simple

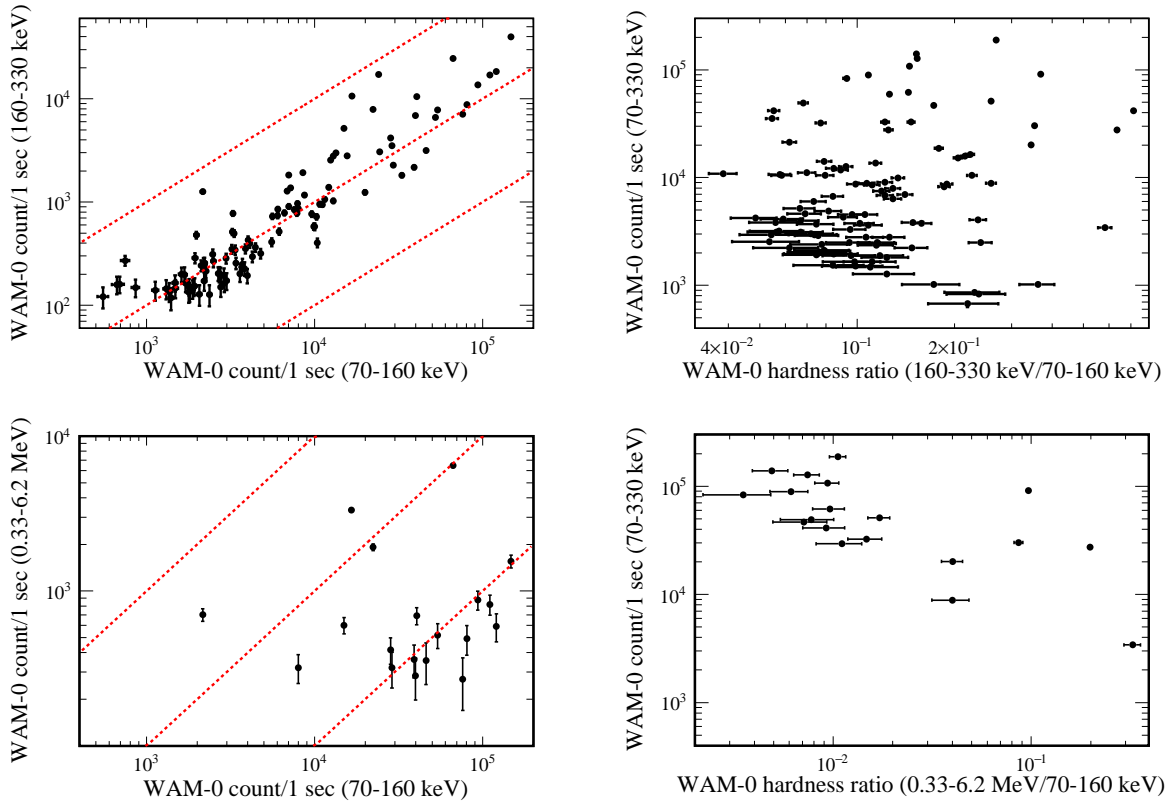


Figure 5.6: Scatter diagrams of WAM-0 count rate. (Top two panels) All plotted data are detected in both energy bands (70–160 keV and 160–330 keV) on WAM-0 and defined as bursts from AXP 1E 1547.0–5408 in §5.1.3. (Bottom two panels) plotted points are detected in all three bands (70–160 keV, 160–330 keV, and 0.33–6.2 MeV) on WAM-0 and, these time bins also defined from AXP 1E 1547.0–5408 in §5.1.3. Red dotted lines means that ratio of vertical axis value over horizontal axis value are 1, 0.1, and 0.01.

correlation. In addition, we plotted Figure 5.7, which is scatter plot of obtained hardness ratio values and the waiting time, however we cannot see significant correlation also.

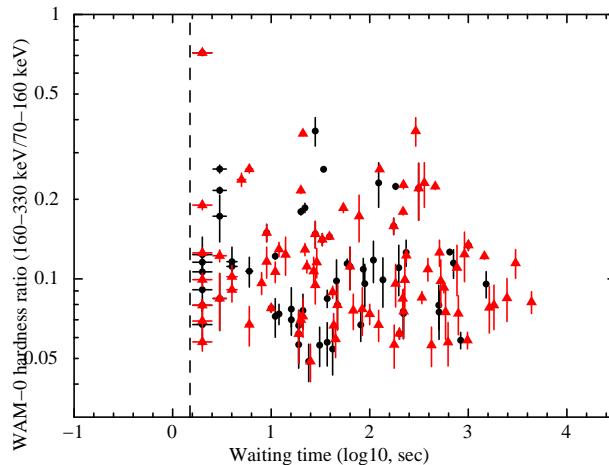


Figure 5.7: Scatter plot between waiting time and hardness ration of 160–330 keV over 70–160 keV. Black and red indicate different waiting time in 70–160 keV and 160–330 keV energy band, respectively, but hardness ratio values are shared. Vertical dashed line indicates measurement limit of the waiting time.

5.2 Preparations for Spectral Analysis

5.2.1 Response Matrixes Generation

According to the *Suzaku* operation on the day and the location of AXP 1E 1547.0–5408 (Camilo et al. 2007), incident angles of high-energy photons from the magnetar to the WAM is calculated as $\theta = 59.9^\circ$, $\phi = 51.4^\circ$. The angle definition is described in §3.1.1. This angle is approximately the halfway between the WAM-0 and the WAM-1 sides. To calculate the response matrix, we used the response matrix generator (§3.1.4) and the angle as the input parameters. The absolute flux for the incident angle has uncertainty of about 30%, which can be see by referring to Figure 18 in Yamaoka et al. (2009). According to Yamaoka et al. (2009) the response matrix uncertainty below 160 keV is insufficient under current calibration, we therefore ignored the range below 160 keV. Since the *Suzaku* satellite structure on the WAM-0 side is not as complex as that on the other sides, the effective area for the WAM-0 is the most reliable among those of the sides. Therefore, we leave the normalization factor of WAM-1 with respect to the WAM-0 sides as a free parameter in the spectral fitting below.

5.2.2 Data Selection

In order to perform WAM spectral analysis, we extracted energy spectra of detected bursts in §5.1.1. The detected source time is defined as T_0 , and the time is listed in Table B.1. Since we used the TRN data with 1-s time-resolution, the detected source 1-s region is $T_0 - T_0 + 1$ s. Using `hxdmkwamspec` included in HEADAS software, we extracted 98 energy spectra from the time bins meeting below selection criteria: (1) at least detected in 160–330 keV range of WAM-0, (2) at least simultaneous detected with one of other instruments, and (3) selected as AXP 1E 1547.0–5408 burst in §5.1.3. Background spectra are extracted from the average of before and after the source time bins, specifically, from $T_0 - 140$ s to $T_0 - 4$ s and $T_0 + 4$ s to $T_0 + 140$ s, respectively, avoiding detected other bursts with WAM-0 and WAM-1.

5.2.3 Development of Pile-up Simulator

If more than one photon coming into the detectors in short time interval than process pitch of on-board electronics, these events are not able to be separated into individual events and thus become treated as a high-energy event or a non X-ray event. In other words, the spectral shape become harder in the case of very bright sources, and thus the estimation of the pile-up effect on spectra is important. Actually some bright bursts were too bright to measure the exact flux by the ACS (Mereghetti et al. 2009b) and the GBM (van der Horst et al. 2012) observation. We consider that the observed spectra by the WAM might be also affected by the pile-up effect. We therefore developed a pile-up simulation code based on the C++ programming language to reproduce the on-board analog electronics TPU (§3.1.2) and to correct the effect in the following spectral fitting. We utilized the SLLIB and SFITSIO³ libraries for reading and writing Flexible Imaging Transport System (FITS) data format files. The inputs are a background spectrum, a light curve, a response matrix, and the spectral model, and the output is the spectral model affected by the pile-up effect. Figure 5.8 shows summary of the pile-up simulator.

The simulator plays the following role. First, it reads the input files and calculates the incident event number. Second, based on shapes of the input spectra and the light curve, the simulator randomizes the arrival time and photon energy. The time and energy information are applied to individual incident events. In this step, we defined pulse shapes of individual events by three functions in the time t and the voltage space V . Figure 5.9 shows the pulse

³<http://www.ir.isas.jaxa.jp/~cyamauch/sli/index.html>

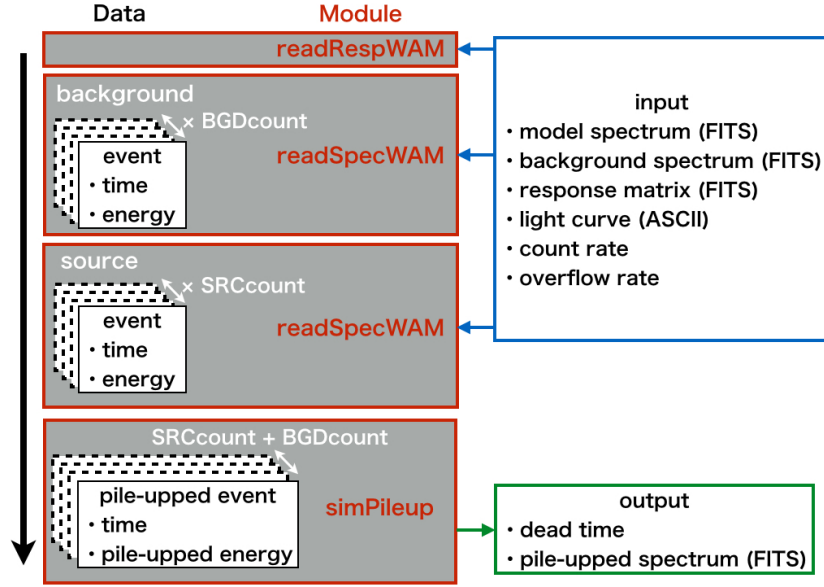


Figure 5.8: Summary of the pile-up simulator. Blue and green are indicate input files and parameters and output ones, respectively.

shape. The three functions are written by

$$V = \begin{cases} A \cdot e^{-\frac{t^2}{2 \times 0.3^2}} & (t < 0 \mu s) \\ A \cdot \frac{1}{8} (9e^{-\frac{t^2}{2 \times 0.65^2}} - 1) & (0 \mu s \leq t, t < 2.5 \mu s) \\ A \cdot \frac{1}{8} [\frac{1}{8}(t - 2.5) - 1] & (2.5 \mu s \leq t) \end{cases}$$

where A is the pulse height, and t is the time from assigned one ($t = 0$) in μs unit. Moreover we assumed that the assigned energies to event-by-event simply proportion the pulse-height. Described above two steps are performed in `readRespWAM` and `readSpecWAM` modules (Figure 5.8), and following two steps are in `simPileup` module (Figure 5.8). Third, these events pass through the reproduced process algorithm of the analog electronics TPU. It is at this point that they are affected by the pile-up effect. Moreover, the simulator accumulates the spectrum from those events. Finally, those three steps are repeated 128 times with different random seed. The simulator calculates an average spectrum assuming Poisson distribution, which it writes out to a FITS format file as the output model. By comparing the output model that considers the pile-up effect with the observed real spectrum, we searched the best-fit parameters by using a Monte-Carlo approach and calculated the chi-squared values.

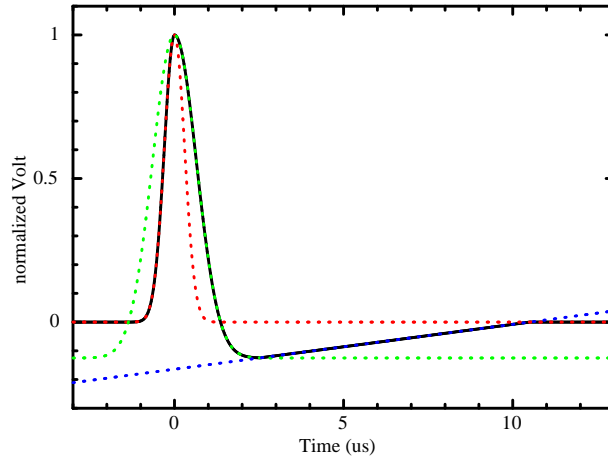


Figure 5.9: Definition of pulse shape in the pile-up simulator (Black solid line), which consists of combination with three functions.

Performance verification of the pile-up simulator is described in §A. For spectral fitting in §5.3, although we used basically the pile-up simulator with chi-square test, XSPEC that is standard software to perform spectral fitting and included in HEADAS software package was also utilized. Useful software XSPEC performs rapid calculation, and its performance is attested by enormous pervious research in X-ray astronomy. But this tool cannot correct the pile-up effect. Therefore the pile-up simulator benefit to all bursts.

5.3 Spectral Analysis

5.3.1 Individual Spectral Fitting

We performed individual spectral fitting for 98 selected time bins (§5.2.2) using our data-acquisition pile-up simulator (§5.2.3 and §A). For detected bursts in only WAM-0 we utilized 1-s WAM-0 spectral data, and for the other selected bursts both sides data were utilized. At the first step, we applied three single-component models consisting of a blackbody (BB), an optically thin thermal bremsstrahlung (OTTB), and a power-law (PL). In the case of that obtained reduced chi-squared values $\chi^2/\text{d.o.f}$, which is test-statistics with chi-squared value over degree of freedom in chi-squared test, are more than 2.2, the more complicated models were assigned, such as a PL with an exponential cut-off (PLE), two-component combination models consisting of two temperatures BB (2BB), a BB plus an OTTB (BB+OTTB), and a

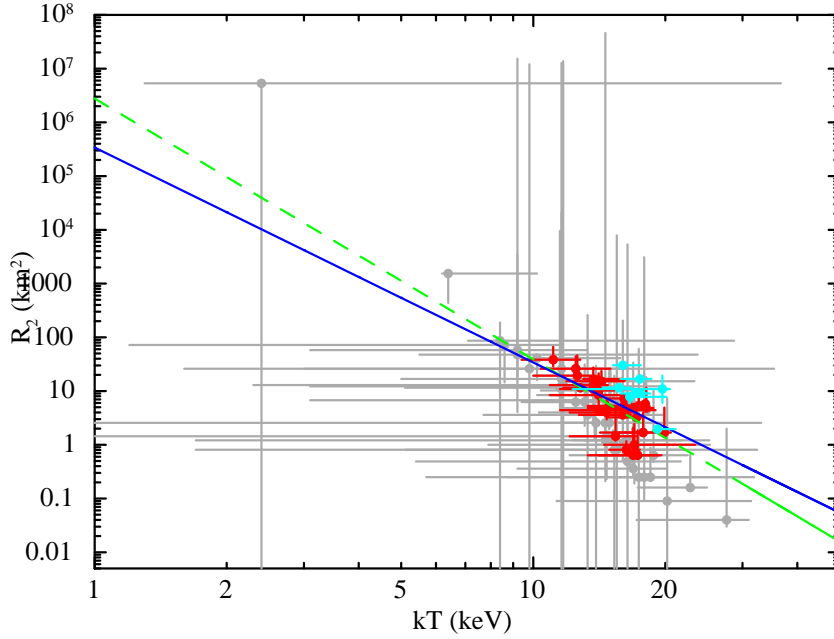


Figure 5.10: Scatter plot between the emission area and the temperature of acceptable BB fitting. Red and black points are better statistical data of quoted errors of R^2 within 70% and the others, respectively. Cyan points represent values of the BB components in acceptable BB+PLE fitting. Green dashed line represents a power-law relation ($R^2 \propto kT^{-4.9 \pm 0.1}$), and blue solid line is $R^2 \propto kT^{-4}$.

BB plus a PL (BB+PL). When obtained statistics values are within the criterion, we defined the model as acceptable. This criterion ($\chi^2/\text{d.o.f} \sim 2.2$) means within about 68% in chi-squared distributions for number of energy bins of the WAM spectra. Moreover for bright bursts, to compare the spectral shapes with persistent emission (§2.3) we utilized also a BB plus a PLE (BB+PLE) model. In following analysis, all quoted errors are 90% significant level.

The single component models better fit 79 time bins of all selected events. Top panel of Figure 5.11 shows sample results of spectral fitting with the BB. In Table C.1, C.2, and C.3, yielded parameters of the single component models are summarized. The BB model of the three models represents many events than the other two models. Then an average temperature is $kT \sim 14.7$ keV. Figure 5.10 shows relation between the BB emission area and the temperature, the data points are taken from Table C.1. We fitted the distribution with a power-law function, and yielded the slope index of -4.9 ± 0.1 . The spectral shapes of surplus 19 events are represented by the two components models. The fitting results

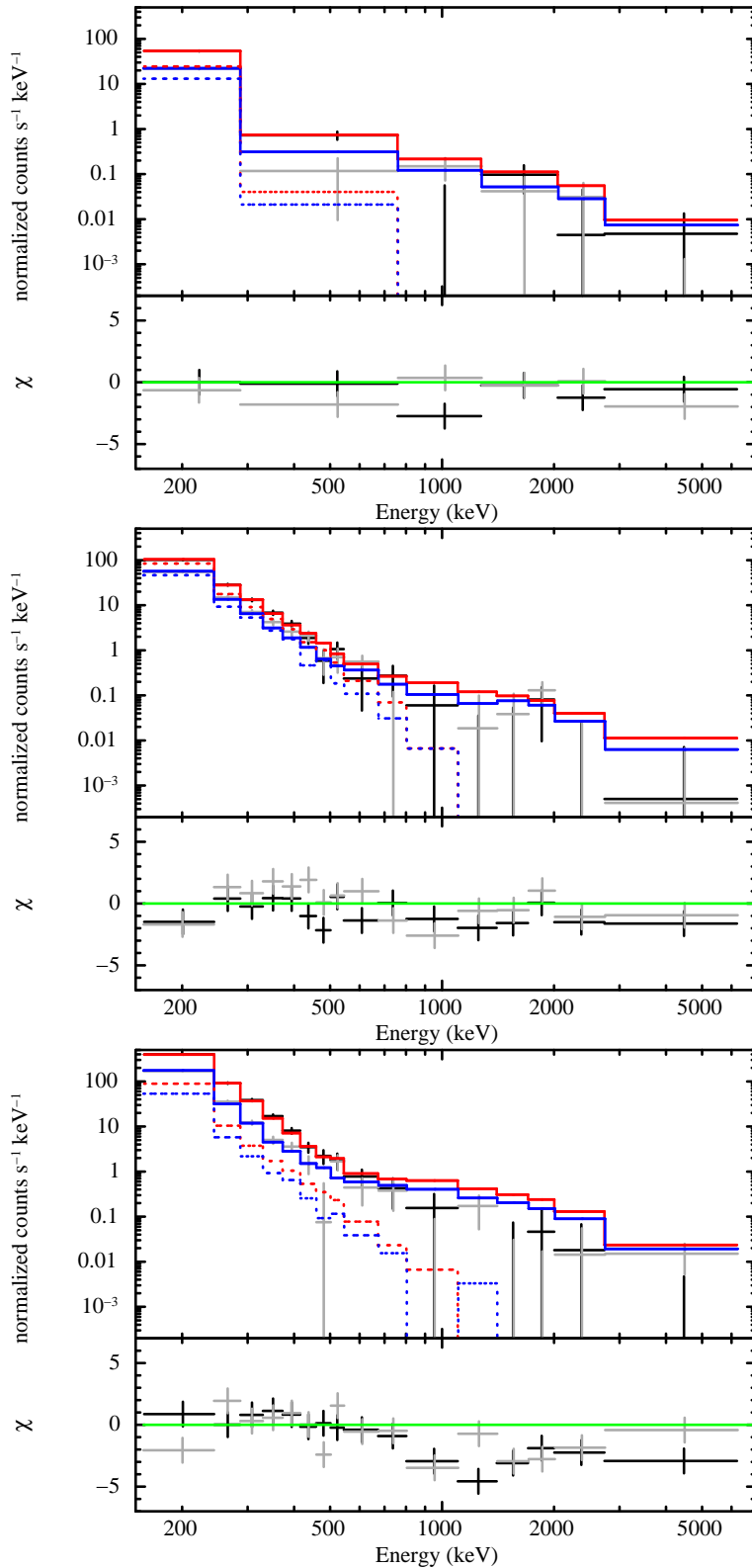


Figure 5.11: Spectra of burst ID 524 (top), 392 (middle), and 520 (bottom) with acceptable model as the BB, the BB+OTTB, and the BB+PLE model, respectively. The lower panels show the residual from best-fit models affected by the pile-up effect. Red lines and blue lines represent the models of WAM-0 and WAM-1, respectively. Models before affected by the pile-up effect and after one are shown as dotted and solid lines, respectively.

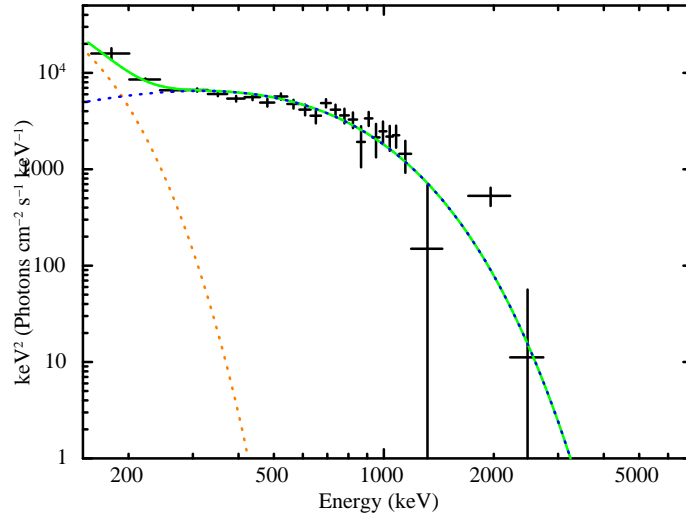


Figure 5.12: Sample $\nu F\nu$ spectrum of burst ID 424 with the best-fit BB+PLE model. Black points are WAM-0 data, and orange, blue, and green lines indicate the BB component, the PLE one, and those sum-up, respectively.

and yielded spectral parameters are shown in Figure 5.11 and summarized in Table C.4, C.5, C.6, and C.7. These 1 s fluence in 160 keV–6.2 MeV range are relativistic bright than represented events by the single component models. Although, obtained sample number and statistics are a few and large, respectively, to determine which model is best to represent the spectral shapes commonly, the BB+OTTB and the BB+PLE models are reasonable than the BB+BB and the BB+PL models. Figure 5.12 shows a $\nu F\nu$ spectrum of burst ID 424, which is the brightest among fitted 98 events. Figure 5.13 and 5.14 show scatter plots of yielded parameters of the BB+OTTB and the BB+PLE models. Although we cannot see strong relations among the parameters due to large errors, the data points in all three plots seem to correlate with simple proportional relations.

5.3.2 Results on Bright Bursts

In this section, we exhibit the detailed spectral analysis of three bright bursts. These light curves and energy spectra are shown in Figure 5.15 and 5.11.

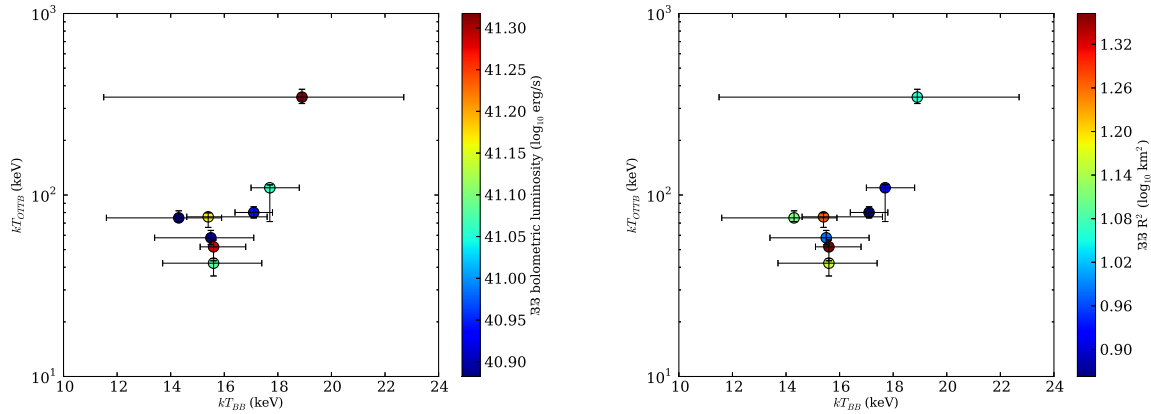


Figure 5.13: Temperature relation between the BB and the OTTB components in the BB+OTTB fitting. The two panels show same data set, but color maps indicate different parameters of the BB component of the bolometric luminosity and radiation area size R^2 .

06:45:13 burst

This is the second brightest burst in 160–330 keV of WAM-0 occur at UTC 06:45:13.3 (burst ID 424 in Table B.1). [Mereghetti et al. \(2009b\)](#) and [Savchenko et al. \(2010\)](#) reported that the ACS detected this burst as the brightest event and labeled it with identifier number 121 and b with properties of a duration of 1.45 s, peak flux of $> 26.3 \times 10^{-5} \text{ erg cm}^{-2} \text{ s}^{-1}$, and fluence of $> 4.6 \times 10^{-5} \text{ erg cm}^{-2}$ in 25 keV–2 MeV energy range. Spectra of ID number 424 and 425 are well fitted by the BB+OTTB and the OTTB models, respectively. The two spectra show rapid spectral shape change. The former consists of hot BB of $\sim 18.9 \text{ keV}$ and high OTTB temperature of $\sim 346 \text{ keV}$, while the latter indicates ordinary OTTB temperature of $\sim 55.3 \text{ keV}$ in better OTTB fitted bursts (Table C.2).

06:48:04 burst

This is known to be the brightest burst from AXP 1E 1547.0–5408 to date, and interesting burst. In Table B.1, the burst numbered by 492–494. The ACS observation ([Mereghetti et al. 2009b](#)) shows extremely bright initial spike and about 8 s pulsation tails. In the WAM-0/WAM-1 ratio histogram (Figure 5.2), since the time bin at the initial spike (ID 493) might be saturated, the bin is within the criteria of the distribution from AXP 1E 1547.0–5408 (§5.1.3). In addition, the time bin of ID 494 is instant of shutdown of the sensor high voltage.

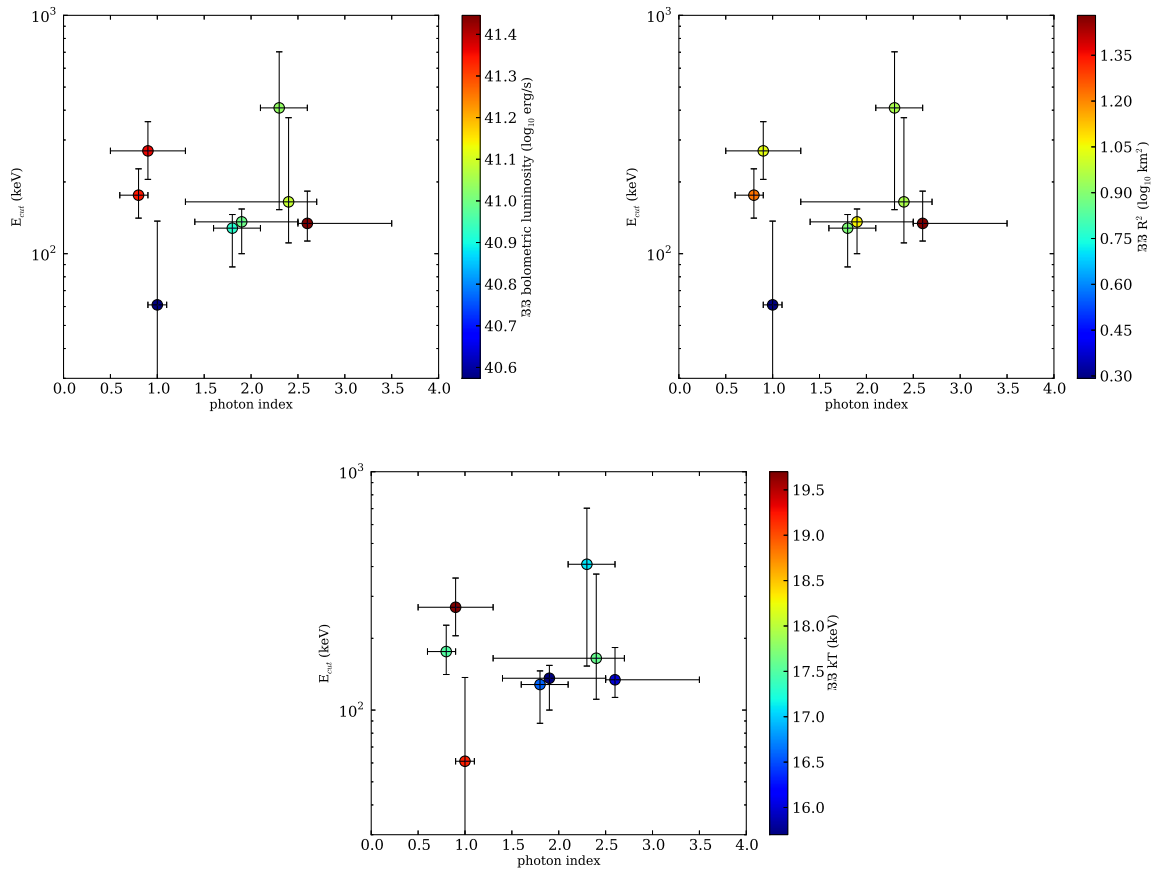


Figure 5.14: Scatter plots of yielded parameters of the PLE component in BB+PLE fitting between the photon index, and the cutoff energy E_{cut} . The three panels show same data set, but color maps indicate different parameters of the BB component of the bolometric luminosity, the radiation area size R^2 , and the temperature kT .

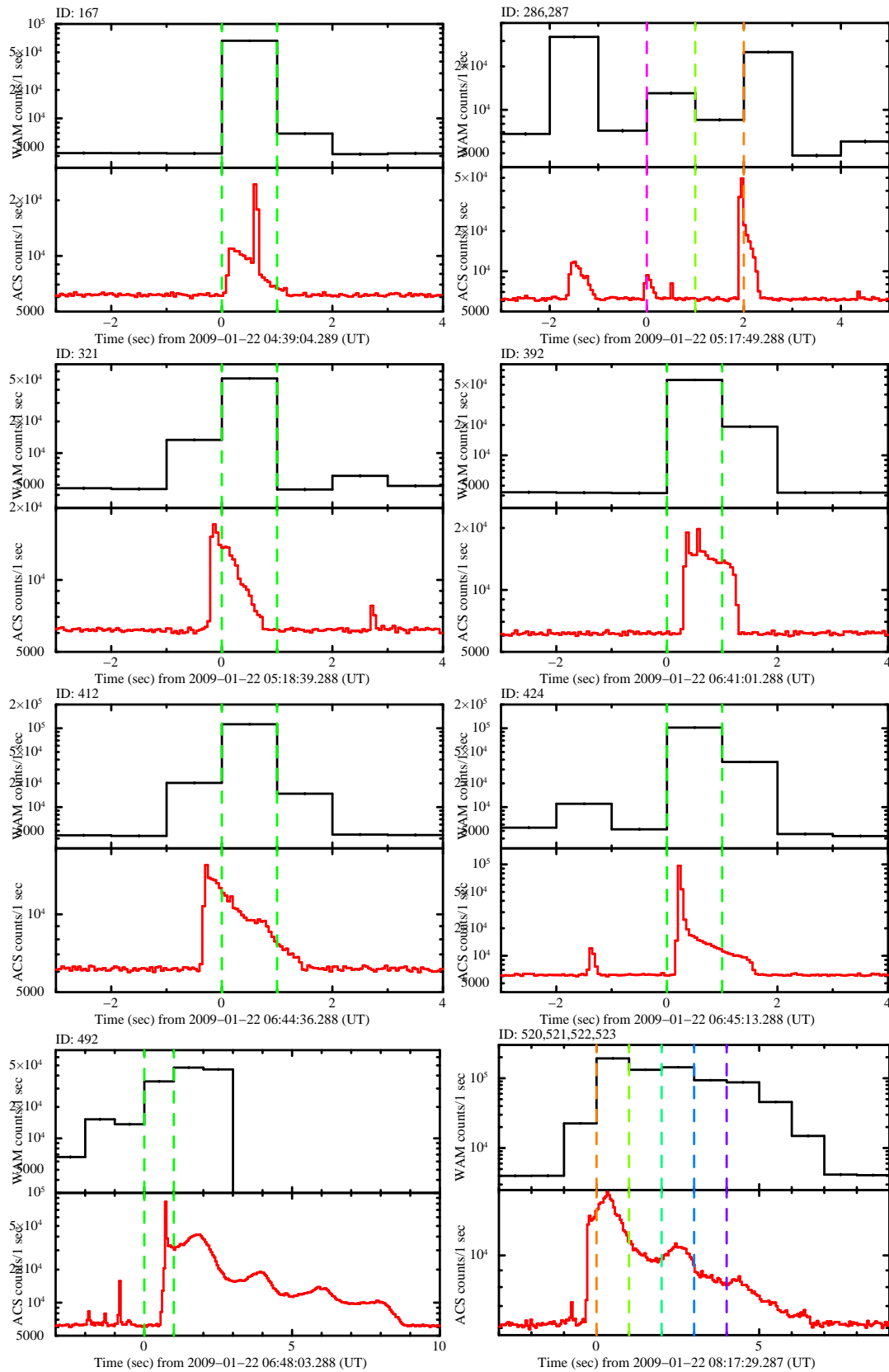


Figure 5.15: WAM-0 and ACS light curves represented by two components models. Between the vertical lines indicate extracted intervals for spectral analysis.

We therefore did not perform spectral fitting to the two time bins.

Chapter 6

Discussion

Contents

6.1	Summary of Observational Results	75
6.2	Burst Statistics, Intensity Distribution	76
6.3	Burst Energetics	77
6.3.1	Estimation of Entire Radiated Energy in Sub-MeV Range	77
6.3.2	Comparison of the BB Parameters with Other Observations	78
6.3.3	Estimation of Surface Magnetic Field Strength to Enclose the BB Plasma	78
6.3.4	Fluence for the Light Echoes	80
6.4	Origin of the Hard X-ray Component	81
6.5	Possible Interpretation of the Radiation Origin	84

6.1 Summary of Observational Results

Making the best use of large effective area and spectral ability of the *Suzaku*/WAM, imaging ability of the *Swift*/BAT and the *Swift*/XRT, and high temporal resolution of the *Fermi*/GBM and the *INTEGRAL*/ACS, we have analyzed the data of 578 time bins of detected bursts by all *Suzaku*/WAM-0 and WAM-1 sides (§5.1.1). To avoid contamination from other astronomical events as solar flares and classical GRBs and ambient particle events

in the satellite orbit, we first selected 404 time bins of all detected events, comparing count rate ratio values of WAM-0 over WAM-1 sides between *Swift* simultaneous events and the others (§5.1.3). Using the defined events as radiated from AXP 1E 1547.0–5408, we searched any correlations in the space of waiting time, brightness, and hardness ratio (§5.1.4). Next, to perform WAM spectral fitting using newly developed pile-up simulator (§5.2.3), we selected 98 events (§5.2.2). In §5.3, we successfully performed spectral fitting with the pile-up correction, and yield individual spectral parameters, which provide us important information about uninvestigated energy band in 160 keV–6.2 MeV.

6.2 Burst Statistics, Intensity Distribution

According to *Fermi*/GBM (8–100 keV; van der Horst et al. 2012) and *INTEGRAL*/ACS (80 keV–8 MeV; Savchenko et al. 2010) observations in same day of 2009 January 22, the mean burst durations are 68 ms and 179 ms, respectively. Since these durations are significant shorter than time resolution of utilized WAM TRN data (1 s), we can consider that presented count rate distributions of Figure 5.4 (§5.1.4) correspond to fluence distributions. The yielded fitting results are $N/dF \propto F^{-0.7 \pm 0.1}$ in soft bandpass (70–160 keV) and $N/dF \propto F^{-0.4 \pm 0.1}$ in hard bandpass (160–330 keV), and these slope indexes are comparable with that of the GBM (-0.7 ± 0.2 ; van der Horst et al. 2012) and the ACS (-0.5 ± 0.1 ; Savchenko et al. 2010). Converting N/dF space to dN/dF , the obtained results are written by $dN/dF \propto F^{-1.7 \pm 0.1}$ and $dN/dF \propto F^{-1.4 \pm 0.1}$, respectively. Like the power-law distribution between fluence and burst number have been represented in burst distributions of other AXPs and SGRs (e.g., Gavriil et al. 2004; Nakagawa et al. 2011, 2007), and Cheng et al. (1996) suggested a similarity of these indexes between the AXPs/SGRs and earthquakes in the earth. Indexes of earthquakes in California, Yellowstone, and Utah regions are -1.63 , -1.70 , and -1.61 , respectively (Cheng et al. 1996). It is well known to be “Gutenberg-Richter” experimental rule, which is a famous empirical rule. Our results also accord the low, and this low is also applied to solar flares. The similar results have been often explained by self-organized criticality.

Yielded mean waiting time T_{waiting} (Figure 5.5 in §5.1.4) are ~ 27 s in 70–160 keV and ~ 42 s in 160–330 keV energy bandpass. The T_{waiting} are comparable with previous reports of other AXPs/SGRs, ~ 47 s from AXP 1E 2259+586 in 2–20 keV (Gavriil et al. 2004), ~ 97 s from SGR 1806–20 in 2–60 keV (Gögüş et al. 2000), and ~ 49 s from SGR 1900+14

in 2–60 keV (Gögüş et al. 1999). These results also support the self-organized criticality system for bursts occurrence.

6.3 Burst Energetics

In §5.3, we have presented spectral fitting for individual events. 58 events of all 78 events are better fitted by the single component models as the BB, the OTTB, and the PL models. Same-day observations in 8–200 keV bandpass with the *Fermi*/GBM (van der Horst et al. 2012) reported that spectral shapes of almost bursts are represented by the 2BB model of average temperatures of ~ 5 keV and ~ 14 keV. Since we find an average temperature of 14.7 keV in our results of the BB model fits, we consider that the WAM observed spectra correspond to the higher temperature components of the 2BB model in X-ray band (Lin et al. 2012; van der Horst et al. 2012; Younes et al. 2014). The following sections discuss radiation energies of the BB model.

6.3.1 Estimation of Entire Radiated Energy in Sub-MeV Range

In Figure 5.3, time history of observed bursts by the WAM was revealed in §5.1.3. Assuming the average BB spectrum of temperature of $kT \sim 14.7$ keV and using the response matrix of WAM-0 (§5.2.1), a count rate (1 count/1 sec) in 70–160 keV (2–3 ch) energy range corresponds to bolometric luminosity of 1.8×10^{36} erg s^{-1} . Integrated count rate of all detected bursts in this bandpass reaches 1.8×10^6 counts, and it corresponds to 3.2×10^{42} ergs. Assuming the dipole magnetic field, total magnetic energy is estimated by

$$\begin{aligned} E_{\text{mag}} &\sim \frac{B^2}{8\pi} R^3 \\ &= 4.1 \times 10^{42} \text{ erg} \left(\frac{B}{3.2 \times 10^{14} \text{ G}} \right)^2 \left(\frac{R}{10 \text{ km}} \right)^3, \end{aligned} \quad (6.1)$$

where B and R are the surface magnetic strength and the radius of the neutron star, respectively. Then the derived counts have not been corrected by the pile-up effect nor included systematic uncertainty of the response matrix, and at some intervals of the WAM exposure are absented by SAA regions and the RBM functions. Since to reveal complete total released energy measuring flux of unmeasured soft X-ray emission and the persistent emission are re-

quired, we can consider that our measured energy is a lower limit of total released energy. If energy source of observed burst emissions were only loss of the magnetic energy, energy of pure dipole field is not enough. Therefore our measured energy supports a hypothesis of that the strong twisted toroidal magnetic field exists in the neutron star interior.

6.3.2 Comparison of the BB Parameters with Other Observations

In §5.3, the BB model represents many observed spectral shapes than the other employed models, and the yielded parameter values of the model are plotted in Figure 5.10. If luminosities of all events were the same, the slope index would be -4 from Stefan-Boltzmann law. Although our results have large statistical and systematic errors, we have confirmed the relation of the slope index of -4.9 ± 0.1 in the WAM results, and the yielded index is comparable with the GBM observation of -4.6 ± 0.4 and -5.3 ± 0.4 for brighter events (Younes et al. 2014) derived from higher temperature components of the 2BB model fitting below 200 keV range. Similar steep slope index was already reported by Israel et al. (2008) from *Swift* observation of SGR 1900+14 above 11 keV BB temperature, and the authors also revealed that bright bursts followed a relation of $R^2 \propto kT^{-3}$. One of interpretation of the reported results is due to the photon-splitting effect and Compton scattering, and the effects extend the observed spectra toward lower energies. The former effect changes photon number, while the latter conserves photon number. According to Thompson & Duncan (1995), the minimum temperature is ~ 11 keV at which photon splitting effect is efficient in maintaining a nearly Planckian spectrum. Since our found average temperature of 14.7 keV is significantly higher than the minimum temperature, derived radiation area values R^2 could have been estimated as smaller than intrinsic values.

6.3.3 Estimation of Surface Magnetic Field Strength to Enclose the BB Plasma

We also converted the radiation area size R^2 -values to bolometric BB luminosities using a distance to AXP 1E 1547.0–5408 of 4 kpc. Figure 6.1 shows histograms of the bolometric BB luminosities, and a scatter plot of the luminosities vs. the R^2 -values. In the former figure, we find possible luminosity limit around 10^{41} erg s $^{-1}$, which is significantly higher than Eddington luminosity $L_{\text{edd}} \sim 1.8 \times 10^{38} (M/1.4M_{\odot})$ erg s $^{-1}$. If the limit value is not

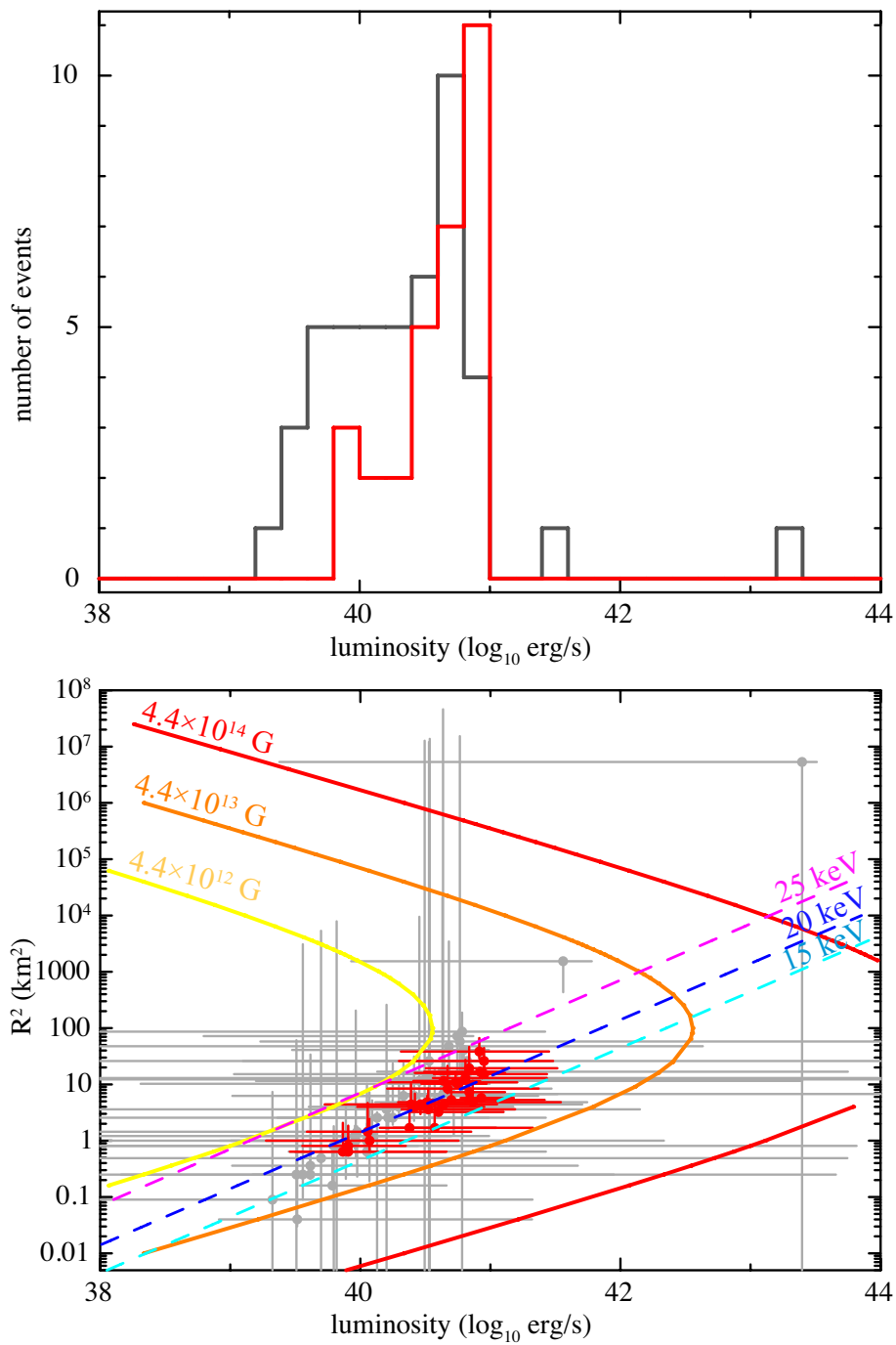


Figure 6.1: Histograms of bolometric luminosities, and scatter plot between the emission area R^2 and the luminosity. Red and black crosses indicate the same events with Figure 5.10.

instrumental bias but intrinsic phenomena of AXP 1E 1547.0–5408, we can estimate lower limit of the surface magnetic field strength employing the trapped fireball model (Thompson & Duncan 1995, 2001). This model was suggested to explain the thermal emission of giant flares, and it interprets the emissions as optically thick pair-photon plasma trapped in closed strong magnetic loop. The trapped fireball model represents not only spectra of giant flares but also time variation of giant flares and intermediate flares (Feroci et al. 2001; Hurley et al. 2005; Olive et al. 2004). Moreover since the model defines that the radiation region is not surface of neutron star, it allows the brighter observed luminosity than Eddington luminosity. Assuming dipole magnetic field simplistically, the field strength of stellar surface B_\star can be estimated through confinement of the energy E_{BB} of the fireball pair-photon plasma in closed magnetic loop of outer radius ΔR . The following in-equation is referred from Equation 1 of Thompson & Duncan (1995),

$$\frac{[B(R_\star + \Delta R)]^2}{8\pi} \geq \frac{E_{\text{BB}}}{3\Delta R^3}, \quad (6.2)$$

where R_\star is the stellar radius. Let a dipole field geometry be $B(R) = B_\star(R/R_\star)^{-3}$. The field strength is written by

$$B_\star > 9.1 \times 10^{11} \left(\frac{E_{\text{BB}}}{10^{41} \text{ erg/s}} \right)^{1/2} \left(\frac{\Delta R}{10 \text{ km}} \right)^{-3/2} \left(1 + \frac{\Delta R}{R_\star} \right)^3 \text{ G}. \quad (6.3)$$

In Figure 6.1, we plotted the estimated magnetic field, and compared them to the WAM results. Whereat the data do not require strong surface field reaching the critical value B_{Q} , but the results indicate the lower limit of the field strength at least $\sim 10^{13}$ G and are congruous with estimated magnetic strength of 3.2×10^{14} G from the rotation periods. As noted above in §6.3.2, if the Planckian distribution is broken by the photon splitting effect, the BB luminosities and the estimated magnetic strength would be derived lower than the intrinsic values.

6.3.4 Fluence for the Light Echoes

Two weeks following observations from 2009 January 22 performed by *Swift*/XRT and *XMM-Newton*/EPIC in soft X-ray bandpass discovered three X-ray rings centered on the object (Tiengo et al. 2010). The ring radii increased and their flux decreased with time. Although

Tiengo et al. (2010) suggested that bright bursts at UTC 06:45:13 (ID 424–425 in Table B.1) lasting ~ 1.5 s and 06:48:04 (ID 493–494) following 8 s tail are candidates for X-ray scattering echoes, these exact fluence has not been measured. According to this suggestion, unabsorbed total energy between 10^{44} erg and 2×10^{45} erg is necessary to generate echoes.

In §5.3, we succeeded in measuring the flux of the burst of ID 424 and 425 through newly developed pile-up simulator (§5.2.3), but the pulsating burst of ID 493–494 was not examined due to causing detector saturation and triggering RBM safety function. The former is the highest flux burst among samples of spectral analysis. The measured total fluence for 2 s is $\sim 12.1 \times 10^{-6}$ erg cm $^{-2}$ in 0.16–6.2 MeV bandpass using results of BB+OTTB and OTTB model fitting. Since soft X-ray flux could be responsible for the dust scattering rings, we calculated a total energy from 1 keV to 10,000 keV range extrapolating the acceptable models, and its energy is $\sim 4.4 \times 10^{41} (\frac{d}{4 \text{ kpc}})^2$ erg assuming isotropic emission. We found that the burst cannot satisfy the condition for forming echoes. Moreover precisely, our measurement is performed in the limited-energy bandpass (0.16–6.2 MeV), and the total fluence could become larger if there were to be another emission component below 160 keV; however, it is not feasible to enhance the fluence by two or three orders of magnitude.

Another candidate other than the highest flux burst could be the pulsation burst of ID 493–494, which has the highest fluence among bursts detected by the ACS (Mereghetti et al. 2009b). The emission energy is already estimated as about $2.4 \times 10^{43} (\frac{d}{10 \text{ kpc}})^2$ erg ($\sim 3.8 \times 10^{42} (\frac{d}{4 \text{ kpc}})^2$ erg) in Mereghetti et al. (2009b), and this energy is likewise not sufficient for generating light echoes. The light echoes are attributed not to the recorded burst tail but to an unrecorded initial spike, which caused the safety switch off of the WAM and saturated the ACS. Therefore, to reveal the origin of the light echoes, the unmeasured soft X-ray spectral shape, especially in the initial spike, is required.

6.4 Origin of the Hard X-ray Component

Thanks to the ability of the WAM to perform wide-band spectroscopy over a large effective area, we succeeded in revealing the spectral shapes of the bursts in the sub-MeV (160 keV–6.2 MeV). Especially, our results revealed additional components to the BB spectral component of ~ 15 keV in the spectra of 19 relatively brighter events among all detected bursts by the WAM §5.3. This is one of the main results of this thesis. Yielded spectral parameters with combination of two-components models are summarized in Table C.4, C.5, C.6, and

C.7, and the BB+OTTB and the BB+PLE models are acceptable than the BB+BB and the BB+PL models. A detailed investigation of the relations will be addressed in future work.

In the BB component of the BB+OTTB and BB+PLE models, the average temperatures are 15.6 keV and 16.0 keV, respectively, and they are comparable with the average temperatures from the 2BB model with the *Fermi*/GBM (~ 5 keV and ~ 15 keV; van der Horst et al. 2012). Moreover the average temperatures of the WAM are consistent with that for the accumulated weak short bursts (~ 13 keV; Enoto et al. 2012) also. The BB components are stable in different emissions, whereas the OTTB and the PLE components are variable in event-by-event. The OTTB temperatures are represented by ~ 40 – 350 keV, and it seems like the temperatures of giant flares spectra (see a review; Mereghetti 2008), but no such variations are observed in shorter time scale (at longest 8 s; Mereghetti et al. 2009b) than the spin period of the object or dimmer radiation energy than typical flux of giant flares (10^{44} erg). In the BB+PLE model, measured photon indexes and cutoff energies of the PLE components also show various values of ~ 0.9 – 3.0 and ~ 60 – 1100 keV, respectively. Next, in order to compare the energy partition rate to each radiation component among the nine different emissions from the object, Figure 6.2 shows a scatter plot of the luminosity in the bolometric BB luminosity (L_{BB} or $L_{2\text{BB}}$) and 1–300 keV luminosity (L_{PL}) of the PL component. The data for our work are calculated by extrapolating the energy range down to 1 keV by using the best-fit parameters of the BB+PLE model (Table C.7). As a result, the empirical correlation for the luminosities between BB and non-thermal components can be extended into the five-orders-of-magnitude brighter region, although the similarities on the spectral shape below about 10^{38} erg s^{-1} are already indicated in Enoto et al. (2012). Our results provide a second example of a magnetar whose spectral shape in the hard X-ray to soft gamma-ray band is stable among various luminosity ranges, after the first report on SGR 0501+4516 (Nakagawa et al. 2011). These results further support the common radiation mechanism in observationally different emissions.

The properties of WAM observed bursts are as if the bursts were “small-scale giant flare” and “large-scale weak short burst”, and match those of intermediate flares (Woods & Thompson 2006). Therefore, that the bursts observed in the WAM energy bandpass (160 keV–6.2 MeV) could be the missing link among three kinds of burst emissions of giant flares, intermediate flares, and short bursts, which are expected to have the same radiation mechanisms because the giant flares commonly follow the intermediate flares by several days or months. However a giant flare has not been observed from AXP 1E 1547.0–5408.

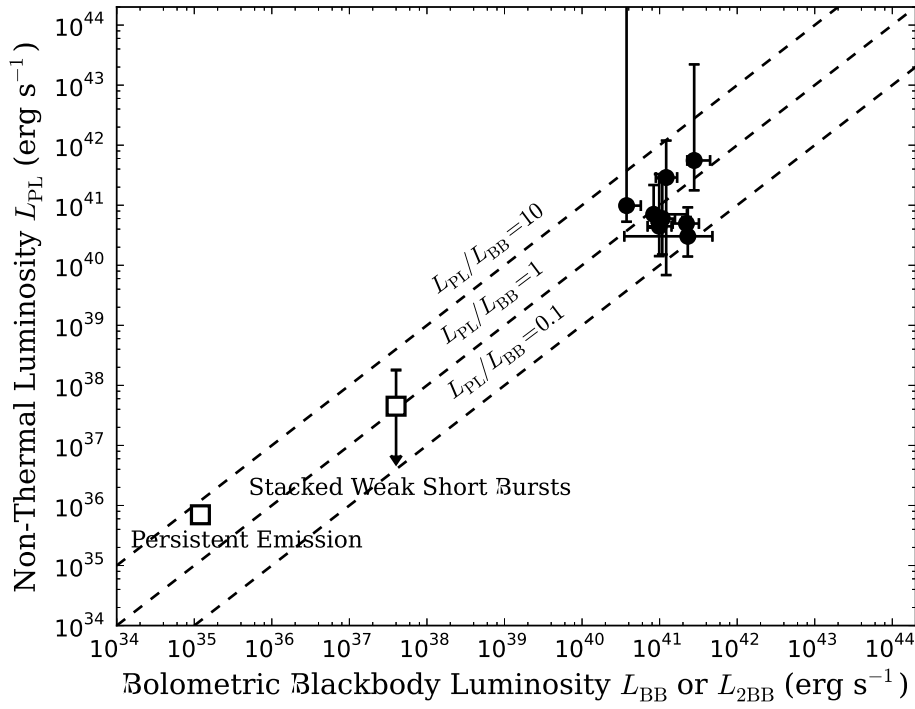


Figure 6.2: Relation between the bolometric BB luminosity and that of the hard X-ray PL component in the 1–300 keV energy range. Points of persistent emission and stacked weak short bursts (squares) are taken from Figure 15 of [Enoto et al. \(2012\)](#). Our results are acceptable BB+PLE model fitting (circles) including the systematic error of absolute flux of 30%.

6.5 Possible Interpretation of the Radiation Origin

Main observational results of this thesis are three, (1) the WAM spectra of bursts are generally represented by the BB model, and the yielded temperature and the radiation area values are comparable with independent observation of *Fermi*, *Swift* and *Suzaku* (Enoto et al. 2012; Lin et al. 2012; van der Horst et al. 2012; Younes et al. 2014)(§6.3.2 and §6.4), (2) derived steep sloop distribution in the kT - R^2 space (§6.3.2), and (3) discovery of additional spectral components in the relatively bright event spectra in addition to the BB component (§6.4).

The trapped fireball model interprets the BB properties of (1), (2), and that soft X-ray spectra are well represented by the 2BB model (Thompson & Duncan 1995). The reconnection of a stressed magnetic field or excitation of Alfvén wave turbulence by crustal cracking inevitably generates optically thick photon-pair plasma in closed magnetic loop. When radiated ordinary (O) and extraordinary (E) polarization mode photons pass through the strong magnetic sphere, the two kinds photons behave differently due to different cross sections. On the strong magnetic loop than the critical field B_Q and near the neutron star surface, since the probability of the photon splitting for E -mode photons is not negligible, high-energy E -mode photons cannot escape the loop, and they are switched to lower energy O -mode photons. In contrast, scattering cross-section of photon splitting of O -mode photons is lower than E -mode photons, and its distribution extend geometrically. However cross-section of Compton scattering and pair-creation of O -mode photons are not also negligible. Therefore the trapped fireball model explains that observed spectra are thermalized, and the two temperature components in X-ray spectra reflect the distribution of the two polarization mode photons. Thompson & Duncan (1995) argues that if thermal equilibrium of the pair-photon plasma is maintained by the photon splitting balancing its inverse process (photon merging), then the photon number increases while the temperature of the plasma decreases to ~ 11 keV (Harding & Lai 2006). This temperature is comparable with the observed average 14.7 keV.

Based on the trapped fireball model, we can consider the BB components of our results were emitted from the E -mode photosphere. Therefore it is a natural guess that the electron-positron annihilation line escapes from the trapped pair-photon plasma affected by the photon splitting effect. If AXP 1E 1547.0–5408 has a strong surface magnetic field of 3.2×10^{14} G estimated from the rotation period, at the attitude of 10 km from the star surface the strength would be comparable with the critical field B_Q . Derived radiation area of results of the BB+OTTB and the BB+PLE models are significantly smaller than 10 km

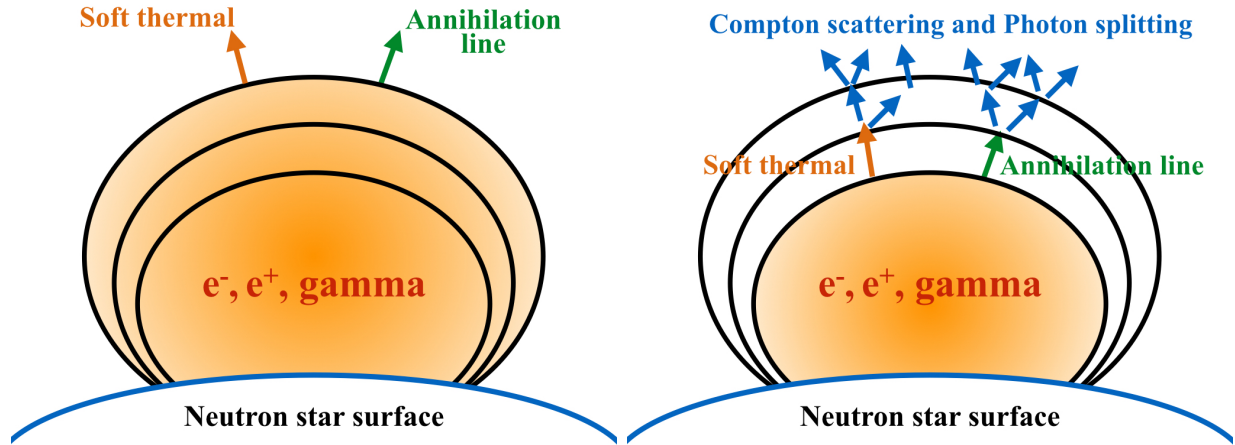


Figure 6.3: Schematic view of a possible interpretation.

(Figure 5.10). Therefore we can consider the pair annihilation 511 keV photons were spread toward lower energy, and the OTTB or the PLE shape represents the spectral shape. Figure 6.3 shows schematic view of the phenomena. In the case of large radiation area (> 10 km) of E -mode photosphere, the photon splitting effect is not efficient, and the additional spectral component could not be observed by the WAM, due to absent sensitivity and energy resolution. Thus this interpretation requires that the object is really a magnetar. Moreover light curve shape of the burst ID 492-493 is represented by predicted function of the time variation of the trapped fireball model (Thompson & Duncan 2001, Yasuda et al. 2015), which supports the above interpretation. In the persistent emission spectra from AXPs/SGRs, the electron-positron annihilation line interpreted the hard X-ray components (Enoto 2010).

Chapter 7

Conclusion

We have presented statistical and spectral analysis of observed burst emissions from AXP 1E 1547.0–5408 using the *Suzaku*/WAM data. The most important observational results are summarized as follows.

1. At least 404 time bins detected in the WAM TRN light curves in the 70–160 keV bandpass, and the distributions of those count rate values and waiting times between event-to-event are represented by power-law functions and lognormal functions, respectively. The phenomena have been confirmed in previous X-ray and gamma ray studies on several AXPs and SGRs as Gutenberg-Richter law.
2. Spectral fitting of the 78 energy spectra of the bursts in sub-MeV range of 0.16–6.2 MeV bandpass have been presented, which show two-three orders magnitude higher luminosities than Eddington luminosity. We found that the BB model generally represents the spectral shapes, and an average temperature is ~ 14.7 keV. Moreover the yielded parameters of temperature kT and radiation area R^2 show steep slope index $R^2 \propto kT^{-4.9 \pm 0.1}$ than Stefan-Boltzmann law.
3. In the 19 energy spectra of the 78 events, we discovered at least one more component in addition to the optically thick thermal component as the BB. Especially, acceptable fits with BB+OTTB and the BB+PLE models indicate the spectral cutoff below 511 keV.

With above observational results, we have constructed the following interpretations.

1. Assuming the trapped fireball model, the obtained luminosities indicate a surface magnetic field strength at lowest $\sim 10^{13}$ G, which is congruous with the estimated strength of 3.2×10^{14} G from the rotation period.
2. With the results of item 2 and 3, the measured spectral shape can be regarded as emissions affected by Compton scattering and the photon splitting effects from the trapped fireball in strong magnetic loop.

Bibliography

- Abdo, A. A., Ackermann, M., Ajello, M., et al. 2010, *Astrophysical Journal Letter*, 725, L73
- Archibald, R. F., Kaspi, V. M., Ng, C.-Y., et al. 2013, *Nature*, 497, 591
- Barthelmy, S. D., Barbier, L. M., Cummings, J. R., et al. 2005, *Space Science Reviews*, 120, 143
- Bellm, E., Smith, D. M., & Hurley, K. 2009, GRB Coordinates Network, 8857, 1
- Boggs, S. E., Zoglauer, A., Bellm, E., et al. 2007, *Astrophysical Journal*, 661, 458
- Braithwaite, J. 2009, *Monthly Notices of the Royal Astronomical Society*, 397, 763
- Burrows, D. N., Hill, J. E., Nousek, J. A., et al. 2005, *Space Science Reviews*, 120, 165
- Camilo, F., Ransom, S. M., Halpern, J. P., & Reynolds, J. 2007, *Astrophysical Journal Letter*, 666, L93
- Cheng, B., Epstein, R. I., Guyer, R. A., & Young, A. C. 1996, *Nature*, 382, 518
- Connaughton, V. & Briggs, M. 2009, GRB Coordinates Network, 8835, 1
- Deller, A. T., Camilo, F., Reynolds, J. E., & Halpern, J. P. 2012, *Astrophysical Journal Letter*, 748, L1
- den Hartog, P. R., Hermsen, W., Kuiper, L., et al. 2006, *Astronomy & Astrophysics*, 451, 587
- Dib, R., Kaspi, V. M., & Gavriil, F. P. 2008, *Astrophysical Journal*, 673, 1044
- Dib, R., Kaspi, V. M., Scholz, P., & Gavriil, F. P. 2012, *Astrophysical Journal*, 748, 3
- Duncan, R. C. & Thompson, C. 1992, *Astrophysical Journal Letter*, 392, L9
- Endo, A., Minoshima, T., Morigami, K., et al. 2010, *Publication of Astronomical Society of Japan*, 62, 1341
- Enoto, T. 2010, X-ray studies of Magnetars with Suzaku
- Enoto, T., Nakagawa, Y. E., Sakamoto, T., & Makishima, K. 2012, *Monthly Notices of the Royal Astronomical Society*, 427, 2824

- Enoto, T., Nakazawa, K., Makishima, K., et al. 2010a, *Publication of Astronomical Society of Japan*, 62, 475
- Enoto, T., Nakazawa, K., Makishima, K., et al. 2010b, *Astrophysical Journal Letter*, 722, L162
- Enoto, T., Rea, N., Nakagawa, Y. E., et al. 2010c, *Astrophysical Journal*, 715, 665
- Esposito, P., Mereghetti, S., Tiengo, A., et al. 2007, *Astronomy & Astrophysics*, 476, 321
- Fahlman, G. G. & Gregory, P. C. 1981, *Nature*, 293, 202
- Feroci, M., Caliendo, G. A., Massaro, E., Mereghetti, S., & Woods, P. M. 2004, *Astrophysical Journal*, 612, 408
- Feroci, M., Hurley, K., Duncan, R. C., & Thompson, C. 2001, *Astrophysical Journal*, 549, 1021
- Frederiks, D. D., Golenetskii, S. V., Palshin, V. D., et al. 2007, *Astronomy Letters*, 33, 1
- Gavriil, F. P., Kaspi, V. M., & Woods, P. M. 2004, *Astrophysical Journal*, 607, 959
- Gehrels, N., Chincarini, G., Giommi, P., et al. 2004, *Astrophysical Journal*, 611, 1005
- Gelfand, J. D. & Gaensler, B. M. 2007, *Astrophysical Journal*, 667, 1111
- Golenetskii, S., Aptekar, R., Mazets, E., et al. 2009a, GRB Coordinates Network, 8858, 1
- Golenetskii, S., Aptekar, R., Mazets, E., et al. 2009b, GRB Coordinates Network, 8863, 1
- Golenetskii, S., Aptekar, R., Mazets, E., et al. 2009c, GRB Coordinates Network, 8913, 1
- Gotthelf, E. V. & Halpern, J. P. 2005, *Astrophysical Journal*, 632, 1075
- Götz, D., Mereghetti, S., Tiengo, A., & Esposito, P. 2006, *Astronomy & Astrophysics*, 449, L31
- Göğüş, E., Woods, P. M., Kouveliotou, C., et al. 1999, *Astrophysical Journal Letter*, 526, L93
- Göğüş, E., Woods, P. M., Kouveliotou, C., et al. 2000, *Astrophysical Journal Letter*, 532, L121
- Gronwall, C., Holland, S. T., Markwardt, C. B., et al. 2009, GRB Coordinates Network, 8833, 1
- Gruber, D., Goldstein, A., Weller von Ahlefeld, V., et al. 2014, *Astrophysical Journal Supplement*, 211, 12
- Guidorzi, C., Frontera, F., Montanari, E., et al. 2004, *Astronomy & Astrophysics*, 416, 297
- Halpern, J. P., Gotthelf, E. V., Reynolds, J., Ransom, S. M., & Camilo, F. 2008, *Astrophysical Journal*, 676, 1178

- Harding, A. K. & Lai, D. 2006, *Reports on Progress in Physics*, 69, 2631
- Hewish, A., Bell, S. J., Pilkington, J. D. H., Scott, P. F., & Collins, R. A. 1968, *Nature*, 217, 709
- Hurley, K., Boggs, S. E., Smith, D. M., et al. 2005, *Nature*, 434, 1098
- Hurley, K., Cline, T., Mazets, E., et al. 1999, *Nature*, 397, 41
- Hurley, K. J., McBreen, B., Rabbette, M., & Steel, S. 1994, *Astronomy & Astrophysics*, 288, L49
- Israel, G. L., Esposito, P., Rea, N., et al. 2010, *Monthly Notices of the Royal Astronomical Society*, 408, 1387
- Israel, G. L., Romano, P., Mangano, V., et al. 2008, *Astrophysical Journal*, 685, 1114
- Iwahashi, T., Enoto, T., Yamada, S., et al. 2013, *Publication of Astronomical Society of Japan*, 65, 52
- Kaneko, Y., Göğüş, E., Kouveliotou, C., et al. 2010, *Astrophysical Journal*, 710, 1335
- Kaspi, V. M. 2007, *Astrophysics and Space Science*, 308, 1
- Kaspi, V. M., Lackey, J. R., & Chakrabarty, D. 2000, *Astrophysical Journal Letter*, 537, L31
- Kitamoto, S., Enoto, T., Safi-Harb, S., et al. 2014, ArXiv e-prints
- Kuiper, L., Hermsen, W., den Hartog, P. R., & Collmar, W. 2006, *Astrophysical Journal*, 645, 556
- Kuiper, L., Hermsen, W., den Hartog, P. R., & Urama, J. O. 2012, *Astrophysical Journal*, 748, 133
- Kuiper, L., Hermsen, W., & Mendez, M. 2004, *Astrophysical Journal*, 613, 1173
- Kumar, H. S., Safi-Harb, S., Slane, P. O., & Gotthelf, E. V. 2014, *Astrophysical Journal*, 781, 41
- Lenters, G. T., Woods, P. M., Goupell, J. E., et al. 2003, *Astrophysical Journal*, 587, 761
- Lin, L., Göğüş, E., Baring, M. G., et al. 2012, *Astrophysical Journal*, 756, 54
- Malheiro, M., Rueda, J. A., & Ruffini, R. 2012, *Publication of Astronomical Society of Japan*, 64, 56
- Manchester, R. N., Hobbs, G. B., Teoh, A., & Hobbs, M. 2005, *Astronomical Journal*, 129, 1993
- Mazets, E. P., Golenetskij, S. V., & Guryan, Y. A. 1979, *Soviet Astronomy Letters*, 5, 343
- Meegan, C., Lichti, G., Bhat, P. N., et al. 2009, *Astrophysical Journal*, 702, 791
- Mereghetti, S. 2008, *Astronomy & Astrophysics Review*, 15, 225

- Mereghetti, S., Gotz, D., von Kienlin, A., et al. 2009a, GRB Coordinates Network, 8841, 1
- Mereghetti, S., Götz, D., von Kienlin, A., et al. 2005, *Astrophysical Journal Letter*, 624, L105
- Mereghetti, S., Götz, D., Weidenspointner, G., et al. 2009b, *Astrophysical Journal Letter*, 696, L74
- Mitsuda, K., Bautz, M., Inoue, H., et al. 2007, *Publication of Astronomical Society of Japan*, 59, 1
- Morii, M., Kitamoto, S., Shibazaki, N., et al. 2010, *Publication of Astronomical Society of Japan*, 62, 1249
- Nakagawa, Y. E., Makishima, K., & Enoto, T. 2011, *Publication of Astronomical Society of Japan*, 63, 813
- Nakagawa, Y. E., Mihara, T., Yoshida, A., et al. 2009, *Publication of Astronomical Society of Japan*, 61, 387
- Nakagawa, Y. E., Yoshida, A., Hurley, K., et al. 2007, *Publication of Astronomical Society of Japan*, 59, 653
- Ng, C.-Y., Kaspi, V. M., Dib, R., et al. 2011, *Astrophysical Journal*, 729, 131
- Nicholl, M., Smartt, S. J., Jerkstrand, A., et al. 2013, *Nature*, 502, 346
- Ohno, M., Fukazawa, Y., Yamaoka, K., et al. 2005, Nuclear Science, IEEE Transactions on, 52, 2758
- Olausen, S. A. & Kaspi, V. M. 2014, *Astrophysical Journal Supplement*, 212, 6
- Olive, J.-F., Hurley, K., Sakamoto, T., et al. 2004, *Astrophysical Journal*, 616, 1148
- Ozaki, M., Watanabe, S., Terada, Y., et al. 2006, Nuclear Science, IEEE Transactions on, 53, 1310
- Palmer, D. M., Barthelmy, S., Gehrels, N., et al. 2005, *Nature*, 434, 1107
- Rau, A., Kienlin, A. V., Hurley, K., & Lichti, G. G. 2005, *Astronomy & Astrophysics*, 438, 1175
- Rea, N. & Esposito, P. 2011, in High-Energy Emission from Pulsars and their Systems, ed. D. F. Torres & N. Rea, 247
- Rea, N., Israel, G. L., Turolla, R., et al. 2009, *Monthly Notices of the Royal Astronomical Society*, 396, 2419
- Rea, N., Pons, J. A., Torres, D. F., & Turolla, R. 2012, *Astrophysical Journal Letter*, 748, L12
- Sakamoto, T., Barthelmy, S. D., Barbier, L., et al. 2008, *Astrophysical Journal Supplement*,

175, 179

- Sakamoto, T., Barthelmy, S. D., Baumgartner, W. H., et al. 2011a, *Astrophysical Journal Supplement*, 195, 2
- Sakamoto, T., Pal'Shin, V., Yamaoka, K., et al. 2011b, *Publication of Astronomical Society of Japan*, 63, 215
- Sasaki, M., Plucinsky, P. P., Gaetz, T. J., et al. 2004, *Astrophysical Journal*, 617, 322
- Savchenko, V., Beckmann, V., Neronov, A., et al. 2009, GRB Coordinates Network, 8837, 1
- Savchenko, V., Neronov, A., Beckmann, V., Produit, N., & Walter, R. 2010, *Astronomy & Astrophysics*, 510, A77
- Scholz, P. & Kaspi, V. M. 2011, *Astrophysical Journal*, 739, 94
- Takahashi, T., Abe, K., Endo, M., et al. 2007, *Publication of Astronomical Society of Japan*, 59, 35
- Tashiro, M. S., Onda, K., Yamaoka, K., et al. 2012, *Publication of Astronomical Society of Japan*, 64, 26
- Terada, Y., Enoto, T., Miyawaki, R., et al. 2008, *Publication of Astronomical Society of Japan*, 60, 25
- Terada, Y., Tashiro, M., Urata, Y., et al. 2009a, The Astronomer's Telegram, 1906, 1
- Terada, Y., Tashiro, M., Urata, Y., et al. 2009b, GRB Coordinates Network, 8845, 1
- Terada, Y., Watanabe, S., Ohno, M., et al. 2005, Nuclear Science, IEEE Transactions on, 52, 902
- Thompson, C. & Duncan, R. C. 1995, *Monthly Notices of the Royal Astronomical Society*, 275, 255
- Thompson, C. & Duncan, R. C. 2001, *Astrophysical Journal*, 561, 980
- Thompson, C., Lyutikov, M., & Kulkarni, S. R. 2002, *Astrophysical Journal*, 574, 332
- Tiengo, A., Esposito, P., Mereghetti, S., et al. 2013, *Nature*, 500, 312
- Tiengo, A., Vianello, G., Esposito, P., et al. 2010, *Astrophysical Journal*, 710, 227
- Urata, Y., Huang, K., Takahashi, S., et al. 2014, *Astrophysical Journal*, 789, 146
- van der Horst, A. J., Kouveliotou, C., Gorgone, N. M., et al. 2012, *Astrophysical Journal*, 749, 122
- Vedrenne, G., Roques, J.-P., Schönfelder, V., et al. 2003, *Astronomy & Astrophysics*, 411, L63
- Vink, J. & Bamba, A. 2009, *Astrophysical Journal Letter*, 707, L148

- Vink, J. & Kuiper, L. 2006, *Monthly Notices of the Royal Astronomical Society*, 370, L14
- von Kienlin, A., Arend, N., Lichti, G. G., Strong, A. W., & Connell, P. 2003, in Society of Photo-Optical Instrumentation Engineers (SPIE) Conference Series, Vol. 4851, X-Ray and Gamma-Ray Telescopes and Instruments for Astronomy., ed. J. E. Truemper & H. D. Tananbaum, 1336–1346
- von Kienlin, A., Meegan, C. A., Paciesas, W. S., et al. 2014, *Astrophysical Journal Supplement*, 211, 13
- Winkler, C., Courvoisier, T. J.-L., Di Cocco, G., et al. 2003, *Astronomy & Astrophysics*, 411, L1
- Woods, P. M., Kouveliotou, C., van Paradijs, J., et al. 1999, *Astrophysical Journal Letter*, 527, L47
- Woods, P. M. & Thompson, C. 2006, Soft gamma repeaters and anomalous X-ray pulsars: magnetar candidates, ed. W. H. G. Lewin & M. van der Klis, 547–586
- Yamaoka, K., Endo, A., Enoto, T., et al. 2009, *Publication of Astronomical Society of Japan*, 61, 35
- Younes, G., Kouveliotou, C., van der Horst, A. J., et al. 2014, *Astrophysical Journal*, 785, 52

Appendix A

Detail of Pile-up Simulator Performance

A.1 Demonstration of Pile-up Simulator

Weight of inflection of spectral shape due to the pile-up effect depends on a light curve of a burst, a response matrix, a background spectrum, a source spectrum and that brightness. We demonstrated dependence property with brightness in Figure A.1, using the pile-up simulator with two spectral models of the BB of 40 keV and the PL function of a photon index $\Gamma = 2.0$ and the data of burst ID 424 in Table B.1; the light curve of the ACS (§4.2.3), the calculated response matrix (§5.2.1), the estimated background spectrum of WAM-0 (§5.2.2). These demonstrations indicate that observed spectral shapes are greatly changed by the pile-up effect depend on inputted photon number. In particular in the case of higher flux (orange and red lines in Figure A.1), flux of lower energy range are strongly decreased and higher energy range are increased as compared to original spectrum with no affected the pile-up effect. Observed count rate of the hardest burst is comparable with the lines of second higher flux cases (orange lines in Figure A.1). Therefore to investigate original spectral shape and flux of the hardest burst, correction of the pile-up effects is important.

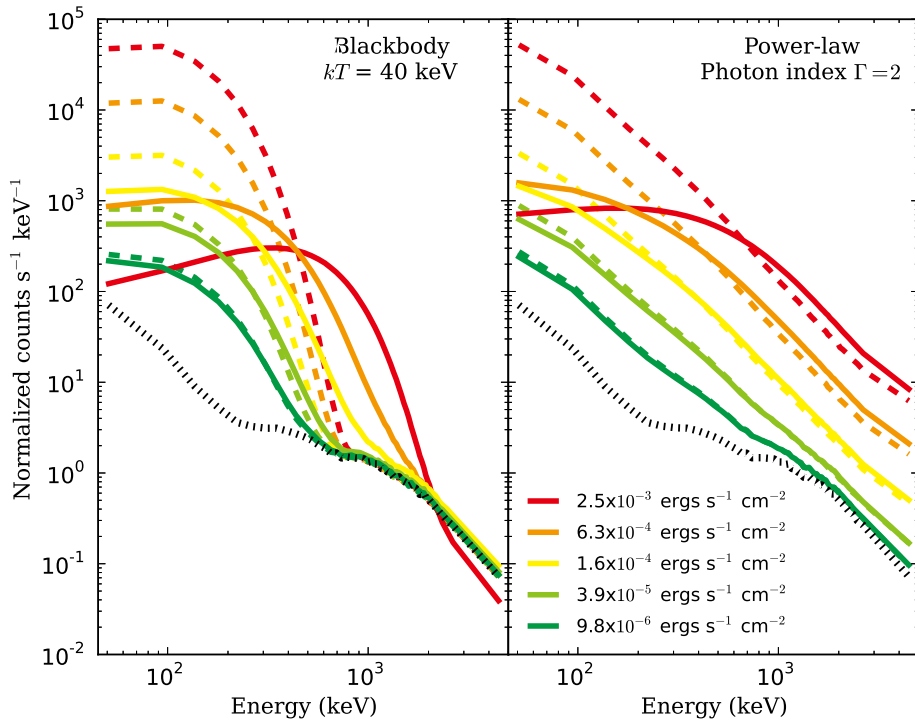


Figure A.1: Demonstration of the pile-up simulator. Left and right panels show estimated observed spectra affected by the pile-up effect (solid lines) and original spectra with no affected by the effect (dashed lines) of a BB of 40 keV and a PL function of photon index $\Gamma = 2.0$. Those spectra have same BB temperature or photon index, and only source fluxes are different. These colors mean different flux in 50 keV–5 MeV energy range, from green to red correspond to from 9.8×10^{-6} to 2.5×10^{-3} erg cm $^{-2}$ s $^{-1}$, respectively. Dotted lines are background level.

A.2 Verification with Bright Solar Flares

In order to verify uncertainty of determination of absolute flux with the pile-up simulator, we checked the uncertainty using five bright solar flares data observed by the WAM after 2009. Comparison of dead-time with count rate between simulated value and observed real one is shown in Figure A.2. We excluded dead-time and count rate from public TRN data of WAM-0 using `hxdmkwam1c` with temporal resolution of 1 s. These solar flares are observed in 2010 February 12, 2011 August 09, 2012 January 23, 2012 March 07 and 2012 July 06, and they are classed as Goes class M8.3, X6.9, M8.7, X5.4 and X1.1, respectively. The pile-up simulator well reproduced the real data. In particular, dead-time of spectra of ID 424 burst as 0.69 s s^{-1} (WAM-0) and 0.67 s s^{-1} (WAM-1) to 1 s exposure in Figure A.2, and reproducibilities around these dead-time are within 1%. Since these reproducibilities are a lot lower than the uncertainty of the response matrixes of 30%, we therefore ignore the reproducibility with the pile-up simulator to measure absolute flux in spectral analysis (§5.3).

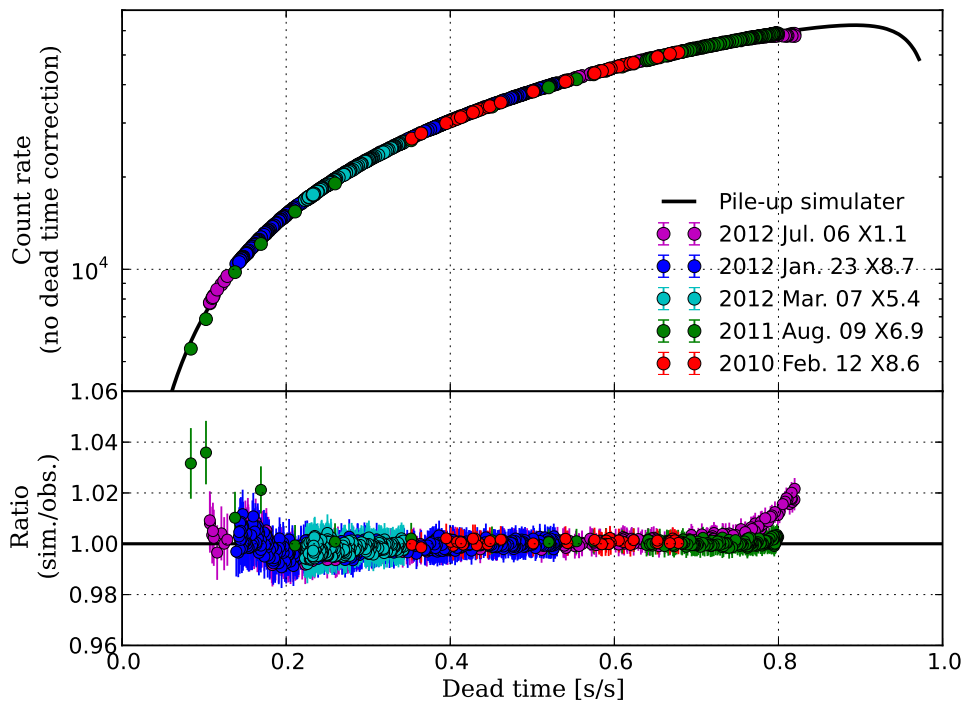


Figure A.2: Relation between dead time and count rate, and comparison of results of the pile-up simulator with observed real data of bright solar flares observed by WAM-0 after 2009. (Top) Red, green, blue, cyan and magenta circles are data of solar flares of 2010 February 12, 2011 August 09, 2012 January 23, 2012 March 07 and 2012 July 06, respectively. Solid black line is result of the pile-up simulator. (Bottom) Ratio of count rate between the observed and simulated ones. We found that a reproducibility of the pile-up simulator is a lot better than the uncertainty of the response matrixes 30%.

Appendix B

All Detected Events

Here is a list of all time bins information detected in the WAM TRN data. Detection criteria is described in §5.1.1.

Table B.1: Detected Events

ID	Date (UT)	WAM-0 (counts/1 sec)		WAM-1 (counts/1 sec)		WAM ¹	Others ¹	Incident angle ²
	2009-01-22	70–160 keV	160–330 keV	70–160 keV	160–330 keV			
1	00:56:43.291	252.7 ±40.3	0
2	00:57:20.291	883.5 ±49.1	...	484.1 ±40.7	...	0,1	...	Yes
3	00:57:34.291	217.6 ±39.5	0
4	00:58:00.291	409.7 ±42.2	...	267.9 ±37.0	...	0,1	...	Yes
5	00:58:18.291	279.6 ±40.8	...	209.2 ±36.5	...	0,1	...	Yes
6	00:59:18.291	808.4 ±47.6	...	555.7 ±41.4	...	0,1	...	Yes
7	00:59:43.291	204.4 ±38.9	0
8	00:59:44.291	573.1 ±44.2	...	312.4 ±37.6	...	0,1	...	Yes
9	01:00:34.291	270.2 ±39.8	...	172.5 ±35.0	...	0,1	...	Yes
10	01:00:57.291	399.4 ±41.8	...	304.9 ±37.1	...	0,1	...	Yes
11	01:01:35.291	184.1 ±38.5	0
12	01:03:25.291	275.0 ±40.0	...	146.1 ±34.2	...	0,1	G	Yes
13	01:03:53.291	261.9 ±39.8	0	G	...
14	01:04:02.291	165.7 ±38.5	0	G	...
15	01:04:25.291	427.1 ±42.4	...	241.5 ±35.9	...	0,1	G	Yes
16	01:05:37.291	445.7 ±42.7	...	245.7 ±35.7	...	0,1	G	Yes
17	01:07:08.291	264.1 ±40.4	0	G	...
18	01:08:41.291	1050.8 ±51.0	...	592.4 ±41.5	...	0,1	G	Yes
19	01:09:58.291	1160.7 ±52.4	...	702.4 ±42.9	...	0,1	A	Yes
20	01:10:01.291	743.0 ±47.1	...	448.8 ±39.0	...	0,1	...	Yes
21	01:12:12.291	409.4 ±42.6	...	277.4 ±36.2	...	0,1	...	Yes
22	01:12:56.291	192.6 ±39.3	0
23	01:13:24.291	205.5 ±39.4	0
24	01:14:14.291	429.6 ±42.8	...	253.7 ±35.7	...	0,1	G	Yes

ID	Date (UT) 2009-01-22	WAM-0 (counts/1 sec)		WAM-1 (counts/1 sec)		WAM ¹	Others ¹	Incident angle ²
		70–160 keV	160–330 keV	70–160 keV	160–330 keV			
25	01:14:45.291	1316.8 ±53.9	...	774.2 ±43.5	...	0,1	G,A	Yes
26	01:15:09.291	184.3 ±39.1	0	G	...
27	01:15:46.291	496.4 ±43.5	...	242.7 ±35.2	...	0,1	G	Yes
28	01:16:08.291	189.4 ±39.1	0	G	...
29	01:16:25.291	160.4 ±38.6	0	G	...
30	01:16:28.291	442.9 ±42.8	...	205.6 ±34.4	...	0,1	G	Yes
31	01:16:40.291	204.9 ±39.2	0	G	...
32	01:17:20.291	422.2 ±42.2	...	212.4 ±34.3	...	0,1	G	Yes
33	01:17:24.291	285.7 ±40.3	...	168.6 ±33.6	...	0,1	G	Yes
34	01:18:10.291	488.4 ±43.1	...	215.1 ±34.2	...	0,1	G	Yes
35	01:18:42.291	1358.2 ±54.2	...	843.8 ±44.0	...	0,1	G,A	Yes
36	01:19:43.291	190.8 ±38.6	0
37	01:20:36.291	453.1 ±42.3	...	249.1 ±34.3	...	0,1	...	Yes
38	01:21:13.291	753.3 ±46.3	...	359.9 ±36.1	...	0,1	...	Yes
39	01:22:23.291	649.5 ±44.7	...	455.3 ±37.4	...	0,1	...	Yes
40	01:23:29.291	633.4 ±44.4	...	393.9 ±36.2	...	0,1	...	Yes
41	01:24:08.291	470.6 ±42.1	...	233.1 ±33.4	...	0,1	...	Yes
42	01:25:04.291	179.0 ±37.8	0	G	...
43	01:25:18.291	814.8 ±46.6	...	485.0 ±37.4	...	0,1	G	Yes
44	01:27:10.291	477.9 ±42.0	...	262.1 ±33.7	...	0,1	G	Yes
45	01:28:59.291	1681.8 ±56.9	198.1 ±34.7	1137.9 ±46.7	...	0,1	G	Yes
46	01:30:09.291	927.6 ±47.9	...	533.3 ±38.1	...	0,1	...	Yes
47	01:31:31.291	403.5 ±40.7	...	280.4 ±33.8	...	0,1	...	Yes
48	01:31:57.291	1279.5 ±52.1	...	808.9 ±42.1	...	0,1	B	Yes
49	01:32:41.291	394.7 ±40.6	...	148.6 ±31.4	...	0,1	B	Yes
50	01:35:02.291	182.4 ±37.3	0	B	...
51	01:35:23.291	817.4 ±46.2	...	515.6 ±37.5	...	0,1	B	Yes
52	01:40:07.291	232.3 ±37.9	0	B	...
53	01:42:45.290	360.8 ±39.7	...	164.7 ±31.6	...	0,1	...	Yes
54	01:42:56.290	189.8 ±37.1	...	116.7 ±30.8	...	0,1	...	Yes
55	01:51:10.290	217.9 ±37.7	0
56	01:55:20.290	138.8 ±36.8	0
57	01:55:48.290	244.4 ±38.4	...	126.4 ±32.1	...	0,1	...	Yes
58	01:56:12.290	848.6 ±46.9	...	521.5 ±38.7	...	0,1	A	Yes
59	01:56:13.290	2203.9 ±62.6	171.7 ±33.8	1338.8 ±50.2	...	0,1	A	Yes
60	01:56:14.290	408.4 ±40.9	...	235.5 ±34.1	...	0,1	...	Yes
61	02:04:02.290	461.5 ±40.6	...	236.3 ±33.4	...	0,1	...	Yes
62	02:05:45.290	415.7 ±39.5	...	195.7 ±32.4	...	0,1	...	Yes
63	02:09:25.290	2711.9 ±66.2	200.5 ±33.5	1711.7 ±53.5	151.9 ±30.5	0,1,3	B,A	Yes
64	02:09:26.290	121.3 ±34.6	...	186.7 ±32.0	...	0,1	B	No
65	02:34:27.290	166.1 ±31.7	...	1	X,G	...
66	02:34:28.290	351.8 ±37.5	...	181.3 ±31.8	...	0,1	X,G	Yes
67	02:36:09.290	909.2 ±45.5	...	479.9 ±36.9	...	0,1	...	Yes
68	02:38:40.290	113.4 ±30.3	1
69	02:42:22.290	177.7 ±35.8	0
70	02:44:50.290	175.6 ±36.0	0
71	02:46:56.290	52276.2 ±379.2	6605.2 ±141.1	35651.6 ±287.2	3024.5 ±91.7	0,1,2,3	A	Yes

ID	Date (UT)	WAM-0 (counts/1 sec)		WAM-1 (counts/1 sec)		WAM ¹	Others ¹	Incident angle ²
		2009-01-22	70–160 keV	160–330 keV	70–160 keV			
72	02:46:57.290	45973.7 ±353.4	3150.1 ±102.0	24200.6 ±221.4	1412.3 ±64.3	0,1,2,3	A	Yes
73	02:47:38.290	364.9 ±39.1	...	167.5 ±31.6	...	0,1	X	Yes
74	02:48:59.290	2157.4 ±61.5	...	1323.4 ±49.0	...	0,1	X,A	Yes
75	02:49:11.290	318.1 ±38.3	...	185.2 ±31.8	...	0,1	X	Yes
76	02:49:43.290	325.4 ±38.5	0	X	...
77	02:50:51.290	144.1 ±35.7	0	B,X	...
78	02:51:08.290	219.8 ±36.9	...	142.0 ±30.9	...	0,1	B,X	Yes
79	02:51:50.290	2
80	02:53:29.290	319.6 ±38.2	...	119.1 ±30.2	...	0,1	B,X,G	Yes
81	02:54:00.290	3595.3 ±75.1	201.8 ±34.0	2435.8 ±61.6	189.3 ±32.2	0,1,2,3	B,X,G,A	Yes
82	02:58:36.290	157.4 ±35.5	...	136.9 ±29.9	...	0,1	B,X	Yes
83	03:02:30.290	2476.6 ±63.7	311.6 ±34.4	1834.7 ±53.7	220.8 ±31.1	0,1,2,3	B,A	Yes
84	03:05:50.290	19933.3 ±192.1	1238.2 ±58.3	12894.8 ±143.9	647.3 ±43.8	0,1,2,3	G,A	Yes
85	03:09:45.290	171.3 ±35.3	...	158.6 ±29.7	...	0,1	...	Yes
86	03:10:29.290	324.8 ±37.7	...	178.9 ±30.3	...	0,1	...	Yes
87	03:11:32.290	208.8 ±35.9	0
88	03:13:32.290	13370.8 ±145.7	2991.8 ±73.7	11154.0 ±129.8	1662.3 ±56.7	0,1,2,3	A	Yes
89	03:14:03.290	363.5 ±38.1	...	124.9 ±29.2	...	0,1	...	Yes
90	03:15:51.290	150.8 ±34.9	0
91	03:16:33.290	225.8 ±36.0	0
92	03:16:34.290	240.4 ±36.2	0
93	03:17:08.290	394.9 ±38.7	...	252.7 ±31.8	...	0,1	...	Yes
94	03:18:55.290	204.7 ±35.8	0
95	03:20:02.290	187.1 ±35.6	0
96	03:20:36.290	539.1 ±40.8	...	215.1 ±31.5	...	0,1	...	Yes
97	03:22:06.290	543.8 ±40.9	...	259.7 ±32.4	...	0,1	...	Yes
98	03:23:03.290	1237.8 ±50.0	...	805.1 ±41.3	...	0,1	...	Yes
99	03:23:04.290	163.3 ±35.3	0
100	03:26:20.290	1310.5 ±51.2	144.4 ±30.7	768.0 ±41.2	...	0,1	...	Yes
101	03:29:11.289	245.4 ±37.1	0
102	03:29:36.289	3
103	03:31:37.289	189.4 ±36.5	0
104	03:32:33.289	585.1 ±42.4	...	322.6 ±34.9	...	0,1	B	Yes
105	03:32:40.289	180.5 ±36.4	0	B	...
106	03:32:54.289	395.4 ±39.7	...	247.7 ±33.7	...	0,1	B	Yes
107	03:38:04.289	546.8 ±41.6	...	257.6 ±33.6	...	0,1	...	Yes
108	03:42:50.289	191.7 ±34.8	0
109	03:44:18.289	129.9 ±30.1	...	1
110	03:44:19.289	776.8 ±43.0	...	394.8 ±34.7	...	0,1	...	Yes
111	03:50:25.289	152.2 ±32.6	0
112	03:50:26.289	800.8 ±42.5	...	372.8 ±33.9	...	0,1	...	Yes
113	03:50:37.289	28845.5 ±242.9	3515.8 ±91.0	19966.4 ±190.6	1668.9 ±62.8	0,1,2,3	A	Yes
114	03:50:38.289	33046.8 ±276.4	1811.7 ±74.5	16150.3 ±167.0	808.5 ±47.8	0,1,2,3	A	Yes
115	03:50:39.289	450.7 ±37.5	...	209.3 ±31.1	...	0,1	...	Yes
116	04:05:44.289	1658.4 ±52.8	...	904.9 ±41.4	117.4 ±27.5	0,1	X,A	Yes
117	04:05:45.289	175.0 ±32.3	0	X	...
118	04:06:26.289	178.1 ±32.3	0	X	...

ID	Date (UT)	WAM-0 (counts/1 sec)		WAM-1 (counts/1 sec)		WAM ¹	Others ¹	Incident angle ²
	2009-01-22	70–160 keV	160–330 keV	70–160 keV	160–330 keV			
119	04:08:31.289	172.0 ±32.3	0	X,G	...
120	04:09:08.289	553.8 ±38.4	...	312.4 ±32.1	...	0,1	X,G	Yes
121	04:10:50.289	136.5 ±31.7	0	G	...
122	04:12:32.289	409.8 ±36.5	...	187.4 ±29.9	...	0,1	X,G	Yes
123	04:12:33.289	360.4 ±35.7	...	145.0 ±29.0	...	0,1	X,G	Yes
124	04:13:22.289	154.9 ±32.5	0	X,G	...
125	04:15:48.289	575.6 ±39.6	...	260.9 ±31.4	...	0,1	X	Yes
126	04:18:22.289	491.8 ±39.0	...	272.7 ±31.8	...	0,1	X	Yes
127	04:19:27.289	210.4 ±34.7	0	X,G	...
128	04:21:32.289	319.2 ±36.7	...	194.6 ±30.3	...	0,1	X,G	Yes
129	04:22:52.289	279.5 ±36.2	...	183.4 ±30.1	...	0,1	X,G	Yes
130	04:23:56.289	174.7 ±34.6	0	X,G	...
131	04:24:45.289	237.3 ±35.6	0	X	...
132	04:26:17.289	107.1 ±28.7	...	1	X	...
133	04:26:47.289	263.4 ±36.1	0	X	...
134	04:27:12.289	183.4 ±34.8	0	X	...
135	04:29:27.289	232.1 ±35.5	0	G	...
136	04:29:51.289	183.3 ±34.7	0	X,G	...
137	04:30:32.289	674.9 ±42.0	...	369.4 ±33.2	...	0,1	X,G	Yes
138	04:31:10.289	103.2 ±28.2	...	1	X	...
139	04:32:18.289	217.0 ±35.3	0	X,G	...
140	04:32:19.289	476.5 ±39.2	...	265.9 ±31.3	...	0,1	X,G	Yes
141	04:32:49.289	2127.8 ±59.5	...	1169.9 ±45.2	...	0,1	X,G	Yes
142	04:33:17.289	211.9 ±35.2	0	X,G	...
143	04:33:27.289	283.4 ±36.4	...	155.3 ±29.2	...	0,1	X,G	Yes
144	04:34:09.289	2765.5 ±65.9	150.1 ±30.1	1623.9 ±50.8	...	0,1,2	X,G	Yes
145	04:34:12.289	178.2 ±34.7	0	X,G	...
146	04:34:17.289	477.1 ±39.3	...	301.2 ±31.9	...	0,1	X,G	Yes
147	04:34:20.289	757.3 ±43.2	...	384.0 ±33.4	...	0,1	X,G	Yes
148	04:34:29.289	203.5 ±35.1	...	140.4 ±28.9	...	0,1	X	Yes
149	04:34:30.289	383.0 ±37.8	...	180.2 ±29.6	...	0,1	X	Yes
150	04:34:33.289	1072.8 ±47.3	...	503.3 ±35.3	...	0,1	X	Yes
151	04:34:40.289	244.5 ±35.7	0	X	...
152	04:34:43.289	161.6 ±34.4	0	X	...
153	04:34:47.289	173.4 ±34.6	0	X	...
154	04:34:52.289	4770.8 ±84.5	317.9 ±34.2	3214.9 ±68.0	196.2 ±30.0	0,1,2,3	X,A	Yes
155	04:34:53.289	3404.5 ±72.0	255.9 ±32.3	2387.0 ±59.6	190.9 ±29.5	0,1,2,3	X,A	Yes
156	04:35:20.289	246.2 ±35.8	...	164.8 ±29.3	...	0,1	X	Yes
157	04:35:22.289	2214.9 ±60.5	256.1 ±31.9	1464.9 ±48.8	165.2 ±28.5	0,1	X,A	Yes
158	04:35:34.289	131.9 ±33.9	0	X	...
159	04:35:52.289	952.0 ±45.7	...	594.2 ±36.5	...	0,1	X,A	Yes
160	04:36:14.289	203.8 ±35.0	...	193.2 ±29.7	...	0,1	X	Yes
161	04:36:40.289	264.3 ±35.9	...	120.9 ±28.2	...	0,1	X	Yes
162	04:36:48.289	218.5 ±35.1	0	X	...
163	04:36:56.289	280.8 ±36.1	...	165.8 ±29.1	...	0,1	X	Yes
164	04:37:15.289	150.6 ±34.1	0	X	...
165	04:38:04.289	178.9 ±34.5	0	X	...

ID	Date (UT) 2009-01-22	WAM-0 (counts/1 sec)		WAM-1 (counts/1 sec)		WAM ¹	Others ¹	Incident angle ²
		70–160 keV	160–330 keV	70–160 keV	160–330 keV			
166	04:38:25.289	1706.6 ±54.6	163.7 ±29.6	1139.8 ±44.3	...	0,1,2,3	X	Yes
167	04:39:04.289	53896.3 ±389.4	7782.6 ±152.4	34294.1 ±277.5	3665.5 ±96.2	0,1,2,3	X,A	Yes
168	04:39:05.289	2368.6 ±62.3	127.0 ±29.5	1467.3 ±48.7	...	0,1	A	Yes
169	04:39:23.289	167.5 ±34.2	...	112.5 ±27.8	...	0,1	X,G	Yes
170	04:39:29.289	212.7 ±34.9	0	X,G	...
171	04:39:36.289	156.9 ±34.0	0	X,G	...
172	04:40:04.289	141.8 ±28.4	...	1	X,G	...
173	04:40:06.289	306.5 ±36.4	...	151.1 ±28.6	...	0,1	X,G	Yes
174	04:40:26.289	326.5 ±36.7	...	271.6 ±30.8	...	0,1	X,G	Yes
175	04:40:28.289	558.3 ±40.0	...	302.4 ±31.4	...	0,1	X,G	Yes
176	04:40:54.289	232.9 ±35.2	...	179.7 ±29.1	...	0,1	X,G	Yes
177	04:41:19.289	794.4 ±43.5	...	439.7 ±33.9	...	0,1	X,G	Yes
178	04:41:20.289	735.3 ±42.6	...	383.1 ±32.8	...	0,1	X,G	Yes
179	04:41:27.289	625.9 ±41.1	...	362.8 ±32.5	...	0,1	G	Yes
180	04:41:43.289	198.6 ±34.6	...	143.1 ±28.4	...	0,1	...	Yes
181	04:42:02.289	2903.2 ±67.1	163.7 ±30.1	2075.1 ±55.7	...	0,1,2,3	A	Yes
182	04:43:05.289	1478.9 ±52.1	164.8 ±29.6	963.0 ±41.9	...	0,1,2	A	Yes
183	04:43:27.289	632.9 ±41.2	...	392.9 ±33.0	...	0,1	...	Yes
184	04:43:33.289	188.7 ±34.6	0
185	04:43:54.289	328.2 ±36.7	...	151.4 ±28.7	...	0,1	...	Yes
186	04:43:56.289	229.5 ±35.3	...	158.4 ±28.8	...	0,1	...	Yes
187	04:43:57.289	221.3 ±35.1	0
188	04:44:00.289	220.6 ±35.1	...	192.7 ±29.4	...	0,1	...	Yes
189	04:44:01.289	295.6 ±36.3	...	160.3 ±28.8	...	0,1	...	Yes
190	04:44:13.289	447.8 ±38.6	...	277.8 ±31.1	...	0,1	...	Yes
191	04:44:19.289	386.0 ±37.7	...	211.1 ±29.8	...	0,1	...	Yes
192	04:44:20.289	828.9 ±43.9	...	433.3 ±33.7	...	0,1	...	Yes
193	04:44:23.289	859.7 ±44.3	148.4 ±28.8	524.5 ±35.1	...	0,1	...	Yes
194	04:44:30.289	400.3 ±37.9	...	178.2 ±29.2	...	0,1	...	Yes
195	04:44:31.289	192.2 ±34.7	0
196	04:44:33.289	1253.3 ±49.3	...	810.4 ±39.6	...	0,1	...	Yes
197	04:44:34.289	238.0 ±35.4	0
198	04:44:42.289	236.9 ±35.4	0
199	04:44:51.289	348.3 ±37.1	...	207.1 ±29.7	...	0,1	...	Yes
200	04:44:52.289	463.4 ±38.9	...	332.9 ±31.9	...	0,1	...	Yes
201	04:44:54.289	557.3 ±40.2	...	274.9 ±31.0	...	0,1	...	Yes
202	04:44:55.289	215.5 ±35.0	0
203	04:45:00.289	760.4 ±43.0	...	517.0 ±35.1	...	0,1	...	Yes
204	04:45:10.289	1348.2 ±50.4	...	803.8 ±39.5	...	0,1,2	A	Yes
205	04:45:31.289	2672.8 ±64.5	202.9 ±30.6	1589.2 ±49.7	110.9 ±26.7	0,1,2	A	Yes
206	04:45:38.289	640.0 ±41.3	...	328.7 ±32.0	...	0,1	A	Yes
207	04:46:02.289	583.9 ±40.5	...	335.4 ±32.0	...	0,1	...	Yes
208	04:46:15.289	196.6 ±34.7	0
209	04:46:39.289	1463.3 ±51.6	...	899.9 ±40.7	...	0,1,2	...	Yes
210	04:46:55.289	1880.9 ±56.4	144.6 ±29.2	1135.8 ±44.0	...	0,1,2	A	Yes
211	04:46:56.289	429.0 ±38.2	...	209.2 ±29.6	...	0,1	...	Yes
212	04:47:20.289	3979.4 ±77.2	194.0 ±31.1	2528.7 ±60.4	...	0,1,2,3	A	Yes

ID	Date (UT) 2009-01-22	WAM-0 (counts/1 sec)		WAM-1 (counts/1 sec)		WAM ¹	Others ¹	Incident angle ²
		70–160 keV	160–330 keV	70–160 keV	160–330 keV			
213	04:47:34.289	236.3 ±35.1	...	222.3 ±29.9	...	0,1	...	Yes
214	04:47:49.289	258.1 ±35.5	...	131.4 ±28.1	...	0,1	...	Yes
215	04:47:50.289	329.9 ±36.6	...	190.8 ±29.3	...	0,1	...	Yes
216	04:48:38.289	169.5 ±34.0	0
217	04:48:48.289	1666.3 ±53.7	...	1059.0 ±42.8	...	0,1,2	...	Yes
218	04:49:00.289	5553.1 ±90.2	409.0 ±35.6	3939.2 ±74.2	254.1 ±30.6	0,1,2,3	...	Yes
219	04:49:04.289	806.2 ±43.4	...	480.6 ±34.4	...	0,1	...	Yes
220	04:49:09.289	183.9 ±34.3	0
221	04:49:20.289	10268.9 ±126.4	719.6 ±43.4	6605.0 ±97.3	323.3 ±33.3	0,1,2,3	...	Yes
222	04:49:30.289	166.7 ±33.9	0
223	04:50:05.289	160.3 ±33.8	0
224	04:50:23.289	150.6 ±33.7	0
225	04:50:24.289	203.9 ±34.6	0
226	04:50:53.289	177.9 ±34.2	...	123.1 ±28.1	...	0,1	...	Yes
227	04:50:55.289	358.4 ±37.0	...	189.7 ±29.4	...	0,1	...	Yes
228	04:51:26.289	372.9 ±37.3	...	242.3 ±30.4	...	0,1	...	Yes
229	04:51:49.289	496.5 ±39.1	...	215.1 ±30.0	...	0,1	...	Yes
230	04:51:50.289	167.0 ±34.0	0
231	04:52:53.289	158.7 ±33.9	...	143.6 ±28.6	...	0,1	...	Yes
232	04:53:14.289	417.6 ±38.0	...	252.3 ±30.8	...	0,1	...	Yes
233	04:53:15.289	6025.6 ±94.1	738.9 ±41.3	4244.1 ±76.9	438.0 ±34.2	0,1,2,3	A	Yes
234	04:53:24.289	3318.0 ±70.8	495.8 ±36.0	2570.4 ±61.0	278.3 ±30.6	0,1,2,3	A	Yes
235	04:53:43.289	2062.5 ±58.3	127.8 ±28.8	1308.5 ±46.6	...	0,1,2	A	Yes
236	04:54:22.289	1637.4 ±53.7	...	1076.3 ±43.6	...	0,1	A	Yes
237	04:54:23.289	306.7 ±36.4	...	199.3 ±29.9	...	0,1	...	Yes
238	04:54:42.289	815.8 ±43.7	...	506.4 ±35.3	...	0,1	...	Yes
239	04:55:03.289	205.2 ±34.9	0
240	04:55:57.289	454.5 ±38.7	...	243.2 ±31.0	...	0,1	...	Yes
241	04:56:42.289	676.9 ±42.0	...	432.0 ±34.5	...	0,1	...	Yes
242	04:57:19.289	6155.1 ±96.0	518.4 ±38.3	4129.6 ±77.0	263.7 ±31.7	0,1,2,3	A	Yes
243	04:57:29.289	29422.9 ±251.8	2280.6 ±77.7	17298.1 ±174.9	1048.5 ±52.1	0,1,2,3	A	Yes
244	04:58:02.289	6039.0 ±93.9	850.9 ±43.0	4491.3 ±80.4	460.0 ±35.6	0,1,2,3	A	Yes
245	04:59:25.289	147.8 ±34.2	0
246	05:00:15.289	375.5 ±37.9	...	202.6 ±31.2	...	0,1	...	Yes
247	05:00:29.289	394.7 ±38.2	...	289.4 ±32.9	...	0,1	...	Yes
248	05:00:47.289	432.3 ±38.9	...	203.9 ±31.4	...	0,1	...	Yes
249	05:01:43.289	218.2 ±35.8	0
250	05:03:15.289	437.5 ±39.4	...	261.5 ±33.1	...	0,1	...	Yes
251	05:03:30.289	1026.1 ±47.6	...	610.6 ±39.1	...	0,1	...	Yes
252	05:03:41.289	754.9 ±44.2	...	434.3 ±36.4	...	0,1	...	Yes
253	05:04:01.289	162.1 ±35.4	0
254	05:05:20.289	181.1 ±36.0	0
255	05:06:54.289	252.4 ±37.2	0
256	05:07:48.289	686.9 ±43.6	...	334.4 ±35.3	...	0,1	...	Yes
257	05:08:25.289	2998.2 ±70.1	172.6 ±32.0	1666.4 ±53.9	...	0,1,2,3	A	Yes
258	05:08:26.289	734.0 ±44.6	...	474.6 ±37.7	...	0,1	...	Yes
259	05:08:59.289	242.7 ±37.2	...	128.1 ±31.4	...	0,1	...	Yes

ID	Date (UT) 2009-01-22	WAM-0 (counts/1 sec)		WAM-1 (counts/1 sec)		WAM ¹	Others ¹	Incident angle ²
		70–160 keV	160–330 keV	70–160 keV	160–330 keV			
260	05:09:20.289	247.0 ±37.3	...	150.1 ±32.0	...	0,1	...	Yes
261	05:10:13.289	193.3 ±36.5	0
262	05:10:27.289	252.2 ±37.3	0
263	05:10:52.289	360.7 ±39.0	...	143.3 ±31.7	...	0,1	...	Yes
264	05:11:36.289	166.9 ±35.9	0
265	05:11:55.288	284.5 ±37.7	...	129.2 ±31.3	...	0,1	...	Yes
266	05:12:25.288	273.7 ±37.5	...	136.1 ±31.2	...	0,1	...	Yes
267	05:13:17.288	192.4 ±36.2	...	155.2 ±31.7	...	0,1	...	Yes
268	05:13:49.288	261.4 ±37.2	0	G	...
269	05:14:02.288	355.2 ±38.5	...	188.7 ±32.1	...	0,1	G	Yes
270	05:14:03.288	11117.3 ±133.8	945.5 ±48.9	7549.5 ±108.0	507.1 ±39.3	0,1,2,3	G,A	Yes
271	05:14:28.288	203.7 ±36.1	0	G	...
272	05:14:29.288	283.5 ±37.4	0	G	...
273	05:16:06.288	803.4 ±45.0	...	445.6 ±36.9	...	0,1	G	Yes
274	05:16:18.288	260.2 ±37.1	...	142.1 ±31.3	...	0,1	G	Yes
275	05:16:43.288	191.1 ±35.6	0	G	...
276	05:16:44.288	136.8 ±34.7	0	G	...
277	05:17:03.288	185.1 ±35.3	...	142.3 ±30.7	...	0,1	G	Yes
278	05:17:41.288	208.2 ±35.5	0
279	05:17:42.288	261.5 ±36.4	...	166.5 ±31.2	...	0,1	...	Yes
280	05:17:43.288	8504.6 ±113.9	1928.3 ±59.6	6243.1 ±95.8	1088.2 ±46.8	0,1,2,3	A	Yes
281	05:17:44.288	1286.4 ±50.4	...	720.2 ±40.3	...	0,1	...	Yes
282	05:17:45.288	4265.1 ±80.5	295.5 ±34.5	2420.8 ±61.3	194.5 ±30.3	0,1,2,3	A	Yes
283	05:17:46.288	2269.3 ±61.6	...	1161.5 ±46.5	...	0,1	...	Yes
284	05:17:47.288	24369.9 ±219.2	3055.8 ±84.0	16098.5 ±167.0	1487.7 ±58.4	0,1,2,3	A	Yes
285	05:17:48.288	2705.2 ±66.3	...	1292.9 ±48.4	...	0,1	A	Yes
286	05:17:49.288	7842.4 ±109.9	779.1 ±44.4	5140.3 ±87.3	452.9 ±36.4	0,1,2,3	A	Yes
287	05:17:50.288	2159.4 ±60.8	1258.6 ±47.9	1795.5 ±54.5	1070.9 ±44.2	0,1,2,3	A	Yes
288	05:17:51.288	14967.0 ±157.3	5158.9 ±95.1	12659.0 ±142.9	2830.8 ±72.0	0,1,2,3	A	Yes
289	05:17:52.288	435.5 ±38.9	...	196.4 ±31.6	...	0,1	...	Yes
290	05:17:53.288	1643.8 ±54.8	...	907.5 ±43.1	...	0,1	A	Yes
291	05:17:54.288	201.9 ±35.3	0
292	05:17:55.288	3874.0 ±76.9	352.5 ±35.2	2541.4 ±62.7	200.1 ±30.4	0,1,2,3	A	Yes
293	05:17:56.288	1165.3 ±49.1	...	560.0 ±38.0	...	0,1	...	Yes
294	05:17:57.288	416.3 ±38.7	...	198.0 ±31.8	...	0,1	...	Yes
295	05:17:58.288	1424.8 ±52.0	...	849.8 ±42.2	...	0,1	A	Yes
296	05:17:59.288	3369.3 ±72.7	343.4 ±35.0	2237.6 ±59.4	205.6 ±30.4	0,1	A	Yes
297	05:18:00.288	817.8 ±44.4	...	533.3 ±37.4	...	0,1	A	Yes
298	05:18:01.288	7200.3 ±103.8	1369.0 ±51.8	5666.2 ±91.2	721.1 ±40.9	0,1,2,3	A	Yes
299	05:18:03.288	12916.7 ±146.3	1026.2 ±51.0	8654.4 ±115.9	544.3 ±39.9	0,1,2,3	A	Yes
300	05:18:04.288	1290.5 ±50.3	...	635.2 ±39.0	...	0,1	...	Yes
301	05:18:07.288	297.6 ±36.7	0
302	05:18:08.288	301.9 ±36.8	0
303	05:18:09.288	406.9 ±38.4	...	260.1 ±32.7	...	0,1	...	Yes
304	05:18:10.288	282.6 ±36.5	0
305	05:18:12.288	245.1 ±35.9	0
306	05:18:15.288	302.3 ±36.9	0

ID	Date (UT) 2009-01-22	WAM-0 (counts/1 sec)		WAM-1 (counts/1 sec)		WAM ¹	Others ¹	Incident angle ²
		70–160 keV	160–330 keV	70–160 keV	160–330 keV			
307	05:18:16.288	946.5 ±46.0	...	517.5 ±37.1	...	0,1	...	Yes
308	05:18:17.288	262.1 ±36.2	0
309	05:18:18.288	625.4 ±41.7	...	382.4 ±34.9	...	0,1	...	Yes
310	05:18:22.288	486.0 ±39.7	...	277.9 ±33.1	...	0,1	...	Yes
311	05:18:25.288	311.5 ±36.9	0
312	05:18:26.288	7577.0 ±106.9	844.4 ±44.8	5300.4 ±88.7	648.3 ±39.8	0,1,2,3	A	Yes
313	05:18:27.288	6603.3 ±100.1	785.3 ±43.7	4397.6 ±80.8	484.1 ±36.6	0,1,2,3	A	Yes
314	05:18:29.288	287.5 ±36.5	0
315	05:18:30.288	292.2 ±36.5	0
316	05:18:31.288	531.6 ±40.2	...	298.3 ±33.4	...	0,1	...	Yes
317	05:18:32.288	3262.7 ±71.1	774.4 ±41.5	2489.4 ±61.7	425.6 ±34.3	0,1,2,3	A	Yes
318	05:18:34.288	280.2 ±36.3	0
319	05:18:35.288	458.6 ±39.1	...	248.1 ±32.4	...	0,1	...	Yes
320	05:18:38.288	7009.7 ±102.0	1824.7 ±57.0	5691.1 ±91.2	1075.2 ±46.2	0,1,2,3	A	Yes
321	05:18:39.288	39803.0 ±312.0	6864.1 ±134.0	24825.1 ±224.1	3585.0 ±90.3	0,1,2,3	A	Yes
322	05:18:41.288	1571.5 ±53.6	...	1095.6 ±45.6	...	0,1	A	Yes
323	05:18:42.288	532.8 ±40.1	...	367.4 ±34.5	...	0,1	...	Yes
324	05:18:46.288	288.1 ±36.5	0
325	05:18:47.288	280.6 ±36.3	0
326	05:18:48.288	500.5 ±39.6	...	245.2 ±32.4	...	0,1	...	Yes
327	05:19:09.288	379.9 ±37.7	...	137.4 ±30.3	...	0,1	...	Yes
328	05:19:13.288	294.3 ±36.4	0
329	05:19:29.288	634.7 ±41.6	...	358.5 ±34.2	...	0,1	...	Yes
330	05:19:58.288	551.9 ±39.9	...	324.4 ±33.4	...	0,1	...	Yes
331	05:20:18.288	175.7 ±33.9	0
332	05:20:40.288	289.6 ±35.7	0
333	05:20:43.288	189.3 ±34.1	...	141.0 ±29.9	...	0,1	...	Yes
334	05:21:14.288	498.1 ±38.8	...	276.9 ±32.2	...	0,1	...	Yes
335	05:21:20.288	206.6 ±34.1	0
336	05:21:52.288	727.2 ±41.9	...	460.5 ±35.3	...	0,1	...	Yes
337	05:21:53.288	247.6 ±34.6	...	144.3 ±29.7	...	0,1	...	Yes
338	05:22:00.288	273.5 ±34.9	0
339	05:22:15.288	663.1 ±40.7	...	315.7 ±32.8	...	0,1	...	Yes
340	05:22:37.288	213.8 ±33.6	0
341	05:22:58.288	314.2 ±35.2	...	153.6 ±29.6	...	0,1	...	Yes
342	05:23:36.288	345.5 ±35.6	...	166.8 ±29.8	...	0,1	...	Yes
343	05:23:41.288	1318.5 ±49.2	...	735.5 ±39.4	...	0,1	...	Yes
344	05:23:42.288	836.9 ±42.9	...	455.7 ±34.9	...	0,1	...	Yes
345	05:24:05.288	196.2 ±33.0	0
346	05:24:07.288	148.1 ±32.1	0
347	05:25:08.288	3215.0 ±69.0	349.8 ±33.6	2119.8 ±56.6	234.6 ±29.7	0,1,2,3	A	Yes
348	05:25:55.288	1906.5 ±55.5	151.9 ±29.3	1186.4 ±45.3	120.2 ±26.9	0,1,2	A	Yes
349	05:25:58.288	1398.4 ±49.6	117.9 ±28.4	803.3 ±39.9	...	0,1	A	Yes
350	05:26:30.288	310.0 ±34.5	...	162.1 ±29.4	...	0,1	...	Yes
351	05:26:44.288	229.4 ±33.0	0
352	05:26:52.288	6868.0 ±99.3	1274.7 ±49.1	5354.4 ±87.1	795.6 ±40.8	0,1,2,3	A	Yes
353	05:27:00.288	366.9 ±35.3	...	154.3 ±29.2	...	0,1	...	Yes

ID	Date (UT) 2009-01-22	WAM-0 (counts/1 sec)		WAM-1 (counts/1 sec)		WAM ¹	Others ¹	Incident angle ²
		70–160 keV	160–330 keV	70–160 keV	160–330 keV			
354	05:27:50.288	148.0 ±31.5	0
355	05:29:54.288	324.6 ±34.4	...	139.5 ±28.8	...	0,1	...	Yes
356	05:30:23.288	1429.8 ±49.7	...	854.5 ±40.6	...	0,1	...	Yes
357	05:31:41.288	242.1 ±33.0	...	153.0 ±29.1	...	0,1	...	Yes
358	05:31:42.288	246.0 ±33.0	...	146.5 ±29.0	...	0,1	...	Yes
359	05:31:45.288	279.7 ±33.6	0
360	05:31:46.288	152.4 ±31.4	0
361	05:31:47.288	196.9 ±32.2	0
362	05:32:03.288	635.3 ±39.2	...	366.2 ±33.0	...	0,1	...	Yes
363	05:32:13.288	147.0 ±31.3	...	185.1 ±29.7	...	0,1	...	No
364	05:32:25.288	739.9 ±40.7	...	419.1 ±33.9	...	0,1	...	Yes
365	05:32:51.288	170.8 ±31.7	0
366	05:34:28.288	129.7 ±31.0	0
367	05:34:51.288	937.8 ±43.5	...	499.6 ±35.2	...	0,1	...	Yes
368	05:34:52.288	484.1 ±36.9	...	232.7 ±30.5	...	0,1	...	Yes
369	05:34:53.288	313.1 ±34.1	0
370	05:35:30.288	159.6 ±31.5	0
371	05:35:38.288	1486.8 ±50.3	146.0 ±29.1	981.6 ±42.4	...	0,1,2	...	Yes
372	05:39:32.288	331.1 ±34.4	...	214.7 ±30.0	...	0,1	...	Yes
373	05:39:33.288	284.9 ±33.7	...	200.6 ±29.8	...	0,1	...	Yes
374	05:41:36.288	692.7 ±40.1	159.8 ±29.3	412.2 ±33.6	...	0,1	X	Yes
375	05:41:53.288	148.7 ±31.5	0	X	...
376	05:49:17.288	221.9 ±33.6	...	140.0 ±28.9	...	0,1	X,G	Yes
377	05:52:14.288	419.6 ±37.2	...	205.1 ±30.3	...	0,1	X,G	Yes
378	05:52:15.288	127.6 ±32.4	0	X,G	...
379	06:03:35.288	952.0 ±45.2	...	574.3 ±36.3	...	0,1	X	Yes
380	06:06:41.288	161.3 ±33.4	0	X	...
381	06:11:57.288	1933.4 ±57.0	153.7 ±29.0	1116.4 ±43.6	...	0,1	X	Yes
382	06:13:20.288	775.3 ±42.5	...	539.5 ±35.0	...	0,1	X	Yes
383	06:21:45.288	1784.5 ±54.7	133.7 ±28.1	1123.8 ±43.6	...	0,1,2,3	...	Yes
384	06:32:07.288	177.0 ±33.6	0
385	06:36:40.288	247.1 ±35.4	0
386	06:38:23.288	315.6 ±36.9	0
387	06:38:27.288	8706.4 ±115.5	1166.5 ±49.4	6375.1 ±97.5	627.9 ±40.1	0,1,2,3	A	Yes
388	06:38:55.288	1941.6 ±57.7	287.1 ±32.1	1143.7 ±46.4	142.7 ±29.0	0,1,2	A	Yes
389	06:40:06.288	303.4 ±37.3	...	195.5 ±32.2	...	0,1	...	Yes
390	06:40:10.288	171.2 ±35.2	...	131.5 ±31.1	...	0,1	...	Yes
391	06:40:27.288	583.0 ±41.7	...	265.7 ±33.7	...	0,1	...	Yes
392	06:41:01.288	40483.7 ±306.9	10514.2 ±159.0	33972.0 ±276.4	5675.7 ±117.5	0,1,2,3	A	Yes
393	06:41:02.288	12428.7 ±140.8	2547.0 ±68.4	10589.8 ±130.2	1665.1 ±58.1	0,1,2,3	A	Yes
394	06:41:44.288	1392.1 ±52.4	...	722.2 ±41.5	...	0,1	...	Yes
395	06:43:05.288	3717.5 ±76.9	249.1 ±33.2	2295.5 ±61.9	...	0,1,3	A	Yes
396	06:43:13.288	228.8 ±37.4	0
397	06:43:14.288	290.9 ±38.4	0
398	06:43:32.288	312.4 ±38.8	...	205.1 ±33.9	...	0,1	...	Yes
399	06:43:38.288	166.9 ±33.2	...	1
400	06:43:42.288	1789.4 ±57.7	...	957.2 ±45.7	...	0,1,3	A	Yes

ID	Date (UT) 2009-01-22	WAM-0 (counts/1 sec)		WAM-1 (counts/1 sec)		WAM ¹	Others ¹	Incident angle ²
		70–160 keV	160–330 keV	70–160 keV	160–330 keV			
401	06:43:45.288	490.6 ±41.5	...	226.6 ±34.2	...	0,1	...	Yes
402	06:43:46.288	604.3 ±43.2	...	366.2 ±36.7	...	0,1	...	Yes
403	06:43:47.288	10706.4 ±133.4	953.6 ±49.1	7041.0 ±106.0	493.9 ±39.8	0,1,2,3	A	Yes
404	06:43:49.288	1274.0 ±52.0	...	776.0 ±43.1	...	0,1	A	Yes
405	06:43:50.288	782.7 ±45.6	...	455.8 ±38.4	...	0,1	A	Yes
406	06:44:09.288	558.1 ±42.6	...	365.7 ±36.8	...	0,1	A	Yes
407	06:44:14.288	852.9 ±46.8	...	387.9 ±37.3	...	0,1	...	Yes
408	06:44:15.288	2258.5 ±63.1	214.1 ±32.2	1565.0 ±54.1	149.8 ±30.9	0,1,2,3	A	Yes
409	06:44:31.288	1063.8 ±49.8	...	596.8 ±40.8	...	0,1	A	Yes
410	06:44:32.288	604.7 ±43.6	...	344.7 ±36.8	...	0,1	...	Yes
411	06:44:35.288	12914.8 ±145.0	2791.1 ±72.0	10972.3 ±134.6	1492.2 ±56.9	0,1,2,3	A	Yes
412	06:44:36.288	93544.0 ±622.8	13603.6 ±241.7	50901.6 ±388.8	5522.2 ±133.9	0,1,2,3	A	Yes
413	06:44:37.288	9606.7 ±127.0	765.2 ±46.2	5494.2 ±94.2	516.1 ±39.9	0,1,2,3	A	Yes
414	06:44:45.288	796.5 ±46.2	...	449.9 ±38.4	...	0,1	A	Yes
415	06:44:53.288	328.0 ±39.6	0
416	06:44:54.288	848.8 ±47.0	...	420.6 ±38.0	...	0,1	...	Yes
417	06:44:58.288	782.6 ±46.3	...	405.2 ±38.1	...	0,1	...	Yes
418	06:44:59.288	7018.2 ±105.6	906.5 ±46.4	4790.1 ±87.2	478.4 ±38.5	0,1,2,3	A	Yes
419	06:45:02.288	253.8 ±38.6	0
420	06:45:09.288	249.8 ±38.6	...	154.7 ±33.4	...	0,1	...	Yes
421	06:45:10.288	949.7 ±48.6	...	430.1 ±38.3	...	0,1	...	Yes
422	06:45:11.288	5602.3 ±94.3	725.2 ±42.9	4086.6 ±81.3	431.1 ±37.6	0,1,2,3	A	Yes
423	06:45:12.288	666.1 ±44.9	158.3 ±30.8	353.7 ±36.9	...	0,1	...	Yes
424	06:45:13.288	66542.7 ±467.5	24588.1 ±285.7	55384.1 ±412.6	14181.8 ±211.7	0,1,2,3	A	Yes
425	06:45:14.288	28303.3 ±245.9	4169.7 ±99.6	19611.1 ±196.5	2337.1 ±74.7	0,1,2,3	A	Yes
426	06:45:18.288	133.5 ±37.0	0
427	06:45:24.288	800.4 ±46.9	...	499.6 ±39.6	...	0,1	...	Yes
428	06:45:35.288	2752.3 ±69.1	198.6 ±32.7	1744.5 ±56.7	157.2 ±31.3	0,1,3	A	Yes
429	06:45:36.288	977.7 ±49.1	...	584.1 ±41.0	...	0,1	A	Yes
430	06:45:39.288	1188.0 ±51.7	...	860.3 ±45.1	...	0,1	A	Yes
431	06:45:41.288	251.6 ±38.9	0
432	06:45:43.288	298.9 ±39.8	0
433	06:45:46.288	484.1 ±42.3	...	259.1 ±35.4	...	0,1	...	Yes
434	06:45:47.288	1056.2 ±50.2	...	531.9 ±40.2	...	0,1	...	Yes
435	06:45:49.288	1615.0 ±56.9	199.5 ±32.1	1099.9 ±48.4	...	0,1	A	Yes
436	06:45:51.288	1249.0 ±53.0	...	720.3 ±43.0	...	0,1	A	Yes
437	06:45:53.288	870.8 ±47.8	...	433.6 ±38.4	...	0,1	...	Yes
438	06:45:55.288	435.8 ±41.8	0
439	06:45:56.288	1006.5 ±49.9	...	398.7 ±38.2	...	0,1	A	Yes
440	06:45:57.288	4108.8 ±81.7	396.2 ±36.8	2784.3 ±68.4	255.7 ±33.7	0,1,2,3	A	Yes
441	06:46:00.288	774.7 ±46.6	...	351.3 ±37.2	...	0,1	...	Yes
442	06:46:01.288	656.1 ±44.9	...	380.3 ±37.7	...	0,1	...	Yes
443	06:46:03.288	2890.2 ±70.5	194.1 ±32.7	1685.7 ±55.9	219.8 ±32.5	0,1,3	A	Yes
444	06:46:05.288	2206.5 ±63.3	...	1240.3 ±50.1	...	0,1,3	A	Yes
445	06:46:10.288	632.1 ±44.5	...	289.3 ±36.1	...	0,1	...	Yes
446	06:46:12.288	948.2 ±48.7	...	536.5 ±40.3	...	0,1	...	Yes
447	06:46:13.288	438.6 ±41.8	0

ID	Date (UT) 2009-01-22	WAM-0 (counts/1 sec)		WAM-1 (counts/1 sec)		WAM ¹	Others ¹	Incident angle ²
		70–160 keV	160–330 keV	70–160 keV	160–330 keV			
448	06:46:14.288	4019.5 ±81.2	427.4 ±37.5	2733.9 ±67.6	281.7 ±34.1	0,1,2,3	A	Yes
449	06:46:19.288	993.2 ±49.4	...	573.4 ±40.8	...	0,1	...	Yes
450	06:46:23.288	2182.4 ±63.0	253.6 ±33.3	1468.9 ±53.2	172.6 ±31.4	0,1,3	...	Yes
451	06:46:34.288	912.4 ±48.2	...	465.2 ±39.1	...	0,1	...	Yes
452	06:46:36.288	799.7 ±46.9	...	454.1 ±38.9	...	0,1	...	Yes
453	06:46:37.288	341.0 ±40.4	...	180.1 ±34.2	...	0,1	...	Yes
454	06:46:41.288	935.6 ±48.8	...	431.2 ±38.6	...	0,1	...	Yes
455	06:46:42.288	2170.9 ±63.1	...	1335.8 ±51.5	...	0,1	...	Yes
456	06:46:43.288	551.0 ±43.6	...	330.8 ±37.0	...	0,1	...	Yes
457	06:46:47.288	245.8 ±39.1	0
458	06:46:48.288	2379.2 ±65.3	...	1266.2 ±50.6	...	0,1	...	Yes
459	06:46:52.288	401.1 ±41.3	0
460	06:46:55.288	854.4 ±47.4	...	456.0 ±38.9	...	0,1	...	Yes
461	06:46:56.288	296.3 ±39.8	0
462	06:46:57.288	473.4 ±42.4	...	239.7 ±35.3	...	0,1	...	Yes
463	06:46:58.288	592.5 ±44.1	...	229.7 ±35.0	...	0,1	...	Yes
464	06:47:06.288	900.7 ±48.1	...	472.6 ±39.3	...	0,1	...	Yes
465	06:47:07.288	2140.9 ±62.8	...	1221.1 ±50.0	...	0,1	...	Yes
466	06:47:08.288	3825.9 ±79.1	226.6 ±33.6	2287.8 ±62.7	140.9 ±31.0	0,1,2	...	Yes
467	06:47:10.288	178.8 ±37.9	0
468	06:47:13.288	178.7 ±37.9	0
469	06:47:20.288	905.2 ±48.2	...	551.6 ±40.3	...	0,1	...	Yes
470	06:47:26.288	537.3 ±43.2	...	271.0 ±35.7	...	0,1	...	Yes
471	06:47:27.288	335.9 ±40.2	...	182.5 ±34.1	...	0,1	...	Yes
472	06:47:29.288	488.3 ±42.6	...	301.8 ±36.4	...	0,1	...	Yes
473	06:47:32.288	213.9 ±38.6	0
474	06:47:33.288	274.7 ±39.4	0
475	06:47:34.288	269.4 ±39.3	0
476	06:47:35.288	2500.4 ±66.4	267.3 ±33.8	1648.7 ±55.1	139.8 ±30.7	0,1,3	A	Yes
477	06:47:42.288	637.0 ±44.7	...	384.8 ±37.6	...	0,1	...	Yes
478	06:47:44.288	398.0 ±41.2	0
479	06:47:45.288	467.5 ±42.1	0
480	06:47:47.288	3021.4 ±72.7	...	1572.5 ±54.6	...	0,1	A	Yes
481	06:47:48.288	1104.5 ±50.8	...	492.5 ±39.4	...	0,1	...	Yes
482	06:47:49.288	662.0 ±44.9	...	374.7 ±37.4	...	0,1	...	Yes
483	06:47:52.288	368.5 ±40.8	0
484	06:47:55.288	796.2 ±46.9	...	384.9 ±37.9	...	0,1	...	Yes
485	06:47:56.288	22266.5 ±213.5	7890.4 ±129.2	17107.9 ±179.7	5032.1 ±100.9	0,1,2,3	A	Yes
486	06:47:57.288	1231.3 ±52.4	...	625.8 ±41.3	...	0,1	A	Yes
487	06:47:58.288	1202.9 ±52.3	...	543.5 ±40.3	...	0,1	...	Yes
488	06:47:59.288	7906.6 ±113.1	966.7 ±48.1	5199.7 ±91.4	553.0 ±40.3	0,1,2,3	A	Yes
489	06:48:00.288	2028.2 ±61.9	...	886.9 ±45.5	...	0,1	...	Yes
490	06:48:01.288	10007.4 ±131.5	577.9 ±43.9	5405.0 ±92.8	290.5 ±35.4	0,1,2,3	A	Yes
491	06:48:02.288	7994.8 ±115.8	860.5 ±47.4	4531.4 ±85.2	409.0 ±37.3	0,1,2,3	A	Yes
492	06:48:03.288	16700.2 ±176.9	10616.5 ±140.9	16915.4 ±176.9	7202.6 ±117.6	0,1,2,3	A	Yes
493	06:48:04.288	22189.9 ±153.1	19746.3 ±143.3	162173.0 ±999.6	79554.9 ±701.1	0,1,2,3	A	No
494	06:48:05.288	24012.7 ±215.9	17199.1 ±182.1	25991.4 ±221.5	9707.6 ±137.5	0,1,2,3	A	Yes

ID	Date (UT)	WAM-0 (counts/1 sec)		WAM-1 (counts/1 sec)		WAM ¹	Others ¹	Incident angle ²
		70–160 keV	160–330 keV	70–160 keV	160–330 keV			
495	07:26:29.288	413.9 ±38.1	...	262.5 ±32.9	...	0,1	X	Yes
496	07:26:30.288	468.4 ±38.8	...	193.2 ±31.5	...	0,1	X	Yes
497	07:30:15.288	398.0 ±38.1	...	224.3 ±32.0	...	0,1	B	Yes
498	07:31:14.288	12145.0 ±139.2	1386.3 ±54.8	9110.4 ±119.0	802.6 ±44.7	0,1,2,3	B,A	Yes
499	07:31:15.288	470.8 ±39.1	...	245.9 ±32.2	...	0,1	B	Yes
500	07:36:28.287	550.5 ±39.7	121.2 ±28.2	289.3 ±31.8	...	0,1	G	Yes
501	07:37:59.287	207.5 ±34.1	...	153.0 ±29.0	...	0,1	G	Yes
502	07:40:15.287	1364.9 ±50.1	135.3 ±28.2	772.2 ±39.2	...	0,1	G	Yes
503	07:40:16.287	193.1 ±33.7	0	G	...
504	07:43:10.287	317.9 ±35.6	...	187.1 ±28.9	...	0,1	...	Yes
505	07:45:39.287	164.4 ±33.0	0
506	07:48:21.287	392.0 ±36.6	...	194.1 ±28.6	...	0,1	...	Yes
507	07:49:39.287	604.0 ±39.8	...	420.6 ±32.7	...	0,1	A	Yes
508	07:49:40.287	11470.4 ±133.9	1063.9 ±48.4	7830.5 ±106.6	618.7 ±38.6	0,1,2,3	A	Yes
509	07:52:35.287	3243.1 ±69.1	513.7 ±35.1	2592.9 ±60.5	273.9 ±29.6	0,1,2,3	...	Yes
510	07:52:36.287	1375.3 ±49.6	...	811.9 ±39.0	...	0,1	...	Yes
511	07:57:00.287	634.5 ±40.0	...	402.7 ±32.3	...	0,1	...	Yes
512	07:57:28.287	746.0 ±41.6	270.4 ±29.8	444.5 ±32.9	127.3 ±25.6	0,1	A	Yes
513	07:57:29.287	263.0 ±34.4	...	120.0 ±26.9	...	0,1	...	Yes
514	07:59:53.287	1259.6 ±48.4	...	762.5 ±38.1	...	0,1	...	Yes
515	07:59:54.287	311.8 ±35.2	...	172.4 ±28.1	...	0,1	...	Yes
516	08:13:50.287	9870.5 ±124.2	578.3 ±40.6	5834.6 ±92.8	295.4 ±33.4	0,1,2,3	A	Yes
517	08:13:51.287	183.6 ±34.2	0
518	08:17:08.287	460.4 ±39.6	...	275.9 ±34.1	...	0,1	...	Yes
519	08:17:28.287	15602.7 ±162.5	2800.5 ±73.7	11349.0 ±135.4	1551.2 ±56.9	0,1,2,3	A	Yes
520	08:17:29.287	147286.0 ±886.3	39747.5 ±462.4	108340.0 ±689.3	16659.4 ±274.1	0,1,2,3	A	Yes
521	08:17:30.287	110373.0 ±702.0	17011.9 ±279.2	67470.6 ±475.1	7265.9 ±161.1	0,1,2,3	A	Yes
522	08:17:31.287	120572.0 ±751.1	18401.6 ±297.0	73896.5 ±508.1	7462.3 ±166.8	0,1,2,3	A	Yes
523	08:17:32.287	80401.6 ±551.7	8758.0 ±187.1	42919.0 ±338.9	3848.0 ±107.9	0,1,2,3	A	Yes
524	08:17:33.287	75999.5 ±526.0	7087.5 ±166.3	40228.3 ±320.0	2880.2 ±93.0	0,1,2,3	A	Yes
525	08:17:34.287	39062.0 ±320.6	2164.0 ±84.2	18571.4 ±189.5	965.4 ±53.6	0,1,2,3	A	Yes
526	08:17:35.287	10371.3 ±130.4	402.7 ±38.8	5347.6 ±91.0	246.9 ±33.6	0,1,2,3	A	Yes
527	08:25:35.287	227.1 ±37.3	...	146.2 ±32.9	...	0,1	...	Yes
528	08:26:14.287	175.7 ±36.2	0	G	...
529	08:26:15.287	216.3 ±36.8	0	G	...
530	08:32:48.287	283.6 ±35.2	...	135.6 ±29.6	...	0,1	...	Yes
531	08:32:49.287	1127.2 ±47.0	139.7 ±29.1	593.2 ±37.4	...	0,1	...	Yes
532	08:32:51.287	299.7 ±35.4	...	177.2 ±30.3	...	0,1	...	Yes
533	08:36:30.287	1805.5 ±54.2	136.0 ±28.5	1139.3 ±44.3	...	0,1	G	Yes
534	08:36:40.287	183.5 ±31.9	0	G	...
535	08:43:30.287	1806.6 ±53.0	...	1027.5 ±42.1	...	0,1	...	Yes
536	08:52:10.287	552.1 ±36.7	...	243.8 ±29.6	...	0,1	...	Yes
537	08:52:11.287	163.5 ±30.3	0
538	08:52:24.287	1050.6 ±43.9	...	613.9 ±35.9	...	0,1	A	Yes
539	08:54:29.287	553.7 ±37.0	...	309.2 ±31.0	...	0,1	...	Yes
540	09:00:12.287	762.4 ±42.1	...	441.6 ±34.9	...	0,1	...	Yes
541	09:00:13.287	142.4 ±32.5	0

ID	Date (UT) 2009-01-22	WAM-0 (counts/1 sec)		WAM-1 (counts/1 sec)		WAM ¹	Others ¹	Incident angle ²
		70–160 keV	160–330 keV	70–160 keV	160–330 keV			
542	09:21:26.287	214.0 ±33.4	...	131.7 ±27.3	...	0,1	X,G	Yes
543	09:26:37.286	1505.5 ±51.1	...	1002.1 ±41.6	...	0,1	X,A	Yes
544	09:36:19.286	166.7 ±32.4	0
545	09:36:37.286	165.2 ±32.4	0
546	09:49:27.286	1305.3 ±49.5	...	891.8 ±41.9	...	0,1	A	Yes
547	09:49:28.286	4445.3 ±81.5	363.1 ±33.8	2833.6 ±65.2	152.1 ±28.8	0,1,2,3	A	Yes
548	09:50:22.286	297.9 ±35.8	...	144.3 ±29.9	...	0,1	...	Yes
549	09:53:37.286	309.7 ±37.0	...	240.0 ±33.0	...	0,1	...	Yes
550	09:53:38.286	915.9 ±45.7	...	542.2 ±38.5	...	0,1	...	Yes
551	10:03:04.286	1632.0 ±55.8	...	1031.5 ±47.1	...	0,1	G,A	Yes
552	10:08:01.286	667.8 ±41.8	...	321.0 ±33.9	...	0,1	G	Yes
553	10:12:39.286	392.8 ±35.5	...	218.3 ±30.1	...	0,1	...	Yes
554	10:12:40.286	174.6 ±31.9	0
555	10:16:40.286	306.0 ±32.8	...	155.7 ±27.9	...	0,1	...	Yes
556	10:30:36.286	1000.0 ±42.9	...	581.8 ±35.2	...	0,1	X	Yes
557	10:30:37.286	1790.0 ±52.7	151.5 ±27.7	1033.8 ±41.9	...	0,1	X	Yes
558	10:49:29.286	202.7 ±36.4	0	X,G	...
559	11:04:02.286	226.6 ±33.2	0	X	...
560	11:06:04.286	223.3 ±33.1	0	X	...
561	11:09:08.286	261.5 ±33.8	...	161.5 ±27.6	...	0,1	...	Yes
562	11:20:56.285	2112.8 ±57.8	242.4 ±29.4	1673.3 ±51.0	149.2 ±27.1	0,1,2,3	A	Yes
563	11:30:51.285	415.5 ±38.5	...	232.5 ±32.8	...	0,1	...	Yes
564	11:52:55.285	152.8 ±29.8	0
565	12:00:48.285	328.2 ±32.1	...	158.5 ±27.3	...	0,1	G	Yes
566	12:05:39.285	293.6 ±31.7	...	144.0 ±27.0	...	0,1	X	Yes
567	12:19:28.285	168.4 ±33.6	...	1
568	12:40:09.285	797.0 ±41.6	...	478.4 ±33.3	...	0,1	X	Yes
569	12:40:30.285	417.1 ±36.0	...	213.5 ±28.4	...	0,1	X	Yes
570	12:42:16.285	550.9 ±38.0	...	236.5 ±28.8	...	0,1	X	Yes
571	14:57:52.284	185.1 ±33.7	...	139.5 ±29.8	...	0,1	...	Yes
572	14:57:57.284	143.3 ±33.0	0
573	15:02:15.284	831.2 ±41.7	...	573.2 ±36.0	...	0,1	...	Yes
574	15:10:34.284	696.7 ±38.0	...	369.5 ±31.4	...	0,1	...	Yes
575	15:10:35.284	204.2 ±29.8	...	139.5 ±26.9	...	0,1	...	Yes
576	15:35:53.284	2974.5 ±67.4	284.4 ±31.7	2196.1 ±57.8	115.0 ±27.7	0,1,2,3	X,A	Yes
577	16:39:26.283	157.0 ±33.6	0	G	...
578	17:02:56.283	1979.9 ±56.7	479.0 ±36.1	960.2 ±41.9	364.8 ±32.7	0,1	X,A	Yes

¹: Detecting instruments. 0:WAM-0, 1:WAM-1, 2:WAM-2, 3:WAM-3, B:BAT, X:XRT, G:GBM and A:ACS.

²: (In §5.1.3) Yes: defined events as from AXP 1E 1547.0–5408. No: defined as background components and/or contamination from other unknown astronomical events.

Appendix C

Spectral Parameters

We show yielded parameters in §5.3, using the pile-up simulator.

Table C.1: Spectral parameters of acceptable BB fitting

ID	kT (keV)	R^1 (km)	F ($\times 10^{-6} \text{erg cm}^{-2} \text{s}^{-1}$) ²	$\chi^2/\text{d.o.f}$ ³
45	13.9 $^{+19.2}_{-15.2}$	<2.4	< 2.55	1.6/4
59	14.7 $^{+2.2}_{-14.8}$	1.2 $^{0.6}_{-1.1}$	< 0.34	4.6/4
63	16.3 $^{+1.2}_{-1.4}$	0.9 $^{+0.6}_{-0.3}$	0.12 $^{+0.16}_{-0.07}$	11.9/9
72	16.1 $^{+0.5}_{-1.4}$	2.7 $^{+1.0}_{-0.5}$	1.04 $^{+0.41}_{-0.48}$	19.1/9
83	17.0 $^{+6.4}_{-2.5}$	1.0 $^{+1.2}_{-0.6}$	0.22 $^{+1.05}_{-0.14}$	6.9/9
84	14.1 $^{+1.2}_{-0.7}$	3.2 $^{+0.9}_{-0.9}$	0.40 $^{+0.29}_{-0.17}$	12.0/9
88	18.1 $^{+0.7}_{-4.1}$	2.2 $^{+2.6}_{-0.4}$	1.90 $^{+0.90}_{-1.38}$	15.1/9
113	17.9 $^{+0.1}_{-5.2}$	2.2 $^{+4.0}_{-0.3}$	1.66 $^{+0.72}_{-1.38}$	14.1/9
114	16.3 $^{+0.3}_{-0.7}$	2.1 $^{+0.5}_{-0.3}$	0.70 $^{+0.25}_{-0.25}$	12.8/8
144	16.9 $^{+3.3}_{-7.7}$	0.6 $^{5.8}_{-0.3}$	< 0.45	2.2/4
154	14.6 $^{+4.7}_{-3.1}$	1.6 $^{+2.3}_{-1.0}$	0.14 $^{+0.48}_{-0.12}$	11.2/9
155	11.5 $^{+3.4}_{-6.4}$	3.4 $^{+97.4}_{-2.6}$	<0.21	2.6/9
157	17.3 $^{+2.3}_{-3.2}$	0.8 $^{+1.1}_{-0.3}$	0.16 $^{+0.34}_{-0.12}$	4.6/9
166	20.2 $^{+11.2}_{-8.9}$	<3.0	< 1.14	1.9/4
168	13.8 ± 3.4	3.2 $^{1.2}_{-3.0}$	< 1.27	5.9/4
181	13.3 $^{+6.6}_{-5.6}$	<17.9	< 0.87	4.0/4

ID	kT (keV)	R^1 (km)	F ($\times 10^{-6}$ erg cm $^{-2}$ s $^{-1}$) 2	$\chi^2/\text{d.o.f}^3$
205	18.5 $^{+4.2}_{-3.2}$	0.5 $^{+0.8}_{-0.2}$	0.13 $^{+0.43}_{-0.09}$	7.1/9
210	16.4 $^{+5.3}_{-11.0}$	<73.9	< 0.71	3.3/4
212	16.0 $^{+4.5}_{-8.1}$	1.0 $^{14.3}_{-0.7}$	< 0.81	0.6/4
233	17.8 $^{+0.9}_{-3.6}$	1.3 $^{+1.5}_{-0.3}$	0.51 $^{+0.40}_{-0.36}$	16.2/9
234	18.8 $^{+3.7}_{-6.7}$	0.8 $^{+3.1}_{-0.4}$	0.35 $^{+0.94}_{-0.32}$	5.3/9
235	15.3 $^{+6.8}_{-13.6}$	<1.9	< 1.04	2.2/4
242	14.7 $^{+2.5}_{-2.6}$	2.0 $^{+1.7}_{-0.8}$	0.24 $^{+0.29}_{-0.17}$	8.0/9
243	14.0 $^{+2.2}_{-0.7}$	4.0 $^{+0.9}_{-1.8}$	0.61 $^{+0.63}_{-0.32}$	15.1/9
244	14.1 $^{+2.5}_{-3.2}$	2.9 $^{+3.6}_{-1.2}$	0.34 $^{+0.43}_{-0.28}$	12.5/9
257	2.4 $^{+34.3}_{-1.1}$	<2631.4	<4.67	1.3/4
270	13.7 $^{+2.5}_{-2.2}$	3.3 $^{+2.4}_{-1.5}$	0.31 $^{+0.38}_{-0.23}$	8.4/9
280	14.3 $^{+1.8}_{-2.4}$	3.9 $^{+2.9}_{-1.4}$	0.69 $^{+0.56}_{-0.49}$	14.8/9
282	16.4 $^{+0.8}_{-4.1}$	1.1 $^{+2.0}_{-0.3}$	0.20 $^{+0.19}_{-0.17}$	4.1/9
284	17.4 $^{+0.7}_{-3.4}$	2.3 $^{+2.2}_{-0.4}$	1.44 $^{+0.71}_{-0.97}$	9.8/9
286	14.3 $^{+0.6}_{-1.9}$	2.7 $^{+1.8}_{-0.5}$	0.31 $^{+0.17}_{-0.19}$	22.9/19
292	13.1 $^{+5.0}_{-3.7}$	2.5 $^{+5.0}_{-2.0}$	<0.50	6.9/9
296	11.7 $^{+1.1}_{-9.4}$	3.6 $^{+3709.6}_{-3.6}$	<0.13	11.6/9
298	12.5 $^{+2.5}_{-2.1}$	5.1 $^{+4.3}_{-2.7}$	0.29 $^{+0.47}_{-0.24}$	7.2/9
299	13.2 $^{+10.1}_{-0.6}$	3.9 $^{+0.9}_{-3.4}$	0.30 $^{+2.26}_{-0.25}$	11.2/9
312	16.0 $^{+0.7}_{-3.3}$	1.9 $^{+2.2}_{-0.4}$	0.46 $^{+0.29}_{-0.33}$	15.5/9
313	13.9 $^{+1.8}_{-3.7}$	2.9 $^{+4.6}_{-1.1}$	0.28 $^{+0.23}_{-0.25}$	11.6/9
317	11.6 $^{+4.6}_{-10.0}$	5.1 $^{+0.8}_{-4.4}$	0.13 $^{+0.53}_{-0.13}$	4.9/9
320	19.9 $^{+0.7}_{-4.7}$	1.3 $^{+1.8}_{-0.4}$	1.48 $^{+0.93}_{-1.18}$	15.8/9
347	17.0 $^{+2.7}_{-5.4}$	1.0 $^{+2.5}_{-0.9}$	< 0.56	3.4/9
348	15.2 $^{+6.6}_{-2.1}$	1.1 $^{+0.8}_{-0.7}$	0.10 $^{+0.37}_{-0.07}$	13.5/9
349	15.5 $^{+16.9}_{-10.4}$	<89.7	< 1.32	6.7/4
352	17.2 $^{+0.4}_{-2.4}$	1.8 $^{+1.4}_{-0.4}$	0.80 $^{+0.47}_{-0.52}$	3.6/9
374	9.2 $^{+4.1}_{-6.1}$	7.6 $^{3920.5}_{-6.3}$	<0.12	2.2/4
381	14.6 $^{+10.6}_{-12.9}$	1.1 $^{1.7}_{-1.0}$	< 2.47	7.6/4
387	13.7 $^{+1.1}_{-2.8}$	3.6 $^{+3.8}_{-0.9}$	0.38 $^{+0.21}_{-0.30}$	11.0/9
388	16.8 $^{+8.5}_{-2.8}$	1.0 $^{+1.0}_{-0.7}$	0.19 $^{+0.85}_{-0.16}$	5.7/9

ID	kT (keV)	R^1 (km)	F ($\times 10^{-6}$ erg cm $^{-2}$ s $^{-1}$) 2	$\chi^2/\text{d.o.f}^3$
395	11.6 $^{+8.3}_{-8.5}$	<3571.1	< 0.71	1.5/4
403	12.6 $^{+0.9}_{-2.6}$	4.4 $^{+5.2}_{-1.4}$	0.24 $^{+0.16}_{-0.20}$	16.8/9
411	18.1 $^{+0.4}_{-4.5}$	2.1 $^{+3.7}_{-0.3}$	1.66 $^{+1.43}_{-1.26}$	7.7/9
413	14.8 $^{+0.7}_{-1.5}$	2.2 $^{+1.2}_{-0.5}$	0.32 $^{+0.20}_{-0.18}$	7.2/9
418	15.3 $^{+2.1}_{-3.7}$	2.2 $^{+3.8}_{-0.9}$	0.4 $^{+0.62}_{-0.34}$	3.7/9
422	6.4 $^{+3.8}_{-0.2}$	39.2 $^{+11.3}_{-33.2}$	<0.05	14.6/9
428	9.2 $^{+14.5}_{-3.7}$	6.9 $^{+58.4}_{-6.6}$	<0.96	7.6/9
435	9.8 $^{+25.6}_{-6.8}$	<3474.7	< 1.85	3.4/4
440	10.2 $^{+5.6}_{-0.5}$	6.4 $^{+1.6}_{-5.0}$	0.04 $^{+0.34}_{-0.02}$	2.1/9
443	12.5 $^{+1.4}_{-2.9}$	2.5 $^{+4.2}_{-1.0}$	0.07 $^{+0.09}_{-0.06}$	6.7/9
448	11.6 $^{+2.0}_{-6.6}$	4.1 $^{+144.2}_{-1.8}$	<0.19	6.9/9
476	15.4 $^{+1.8}_{-3.3}$	1.2 $^{+1.8}_{-0.5}$	0.14 $^{+0.21}_{-0.11}$	5.6/9
488	14.6 $^{+1.2}_{-11.5}$	2.6 $^{+6789.1}_{-0.7}$	< 0.83	11.8/9
490	12.8 $^{+0.5}_{-1.1}$	3.4 $^{+1.3}_{-0.8}$	0.17 $^{+0.08}_{-0.09}$	14.5/9
491	11.1 $^{+1.7}_{-1.7}$	6.2 $^{+5.3}_{-3.1}$	0.11 $^{+0.15}_{-0.09}$	15.8/9
498	16.1 $^{+0.7}_{-2.8}$	2.3 $^{+1.9}_{-0.5}$	0.71 $^{+0.37}_{-0.48}$	14.8/9
500	8.6 $^{+3.0}_{-7.4}$	8.5 $^{1.3}_{-7.6}$	<0.053	1.0/4
502	17.9 $^{+10.2}_{-12.2}$	0.5 $^{55.5}_{-0.4}$	< 1.39	3.3/4
508	15.0 $^{+1.0}_{-4.1}$	2.6 $^{+4.2}_{-0.7}$	0.47 $^{+0.24}_{-0.42}$	7.2/9
512	27.6 $^{+3.4}_{-10.4}$	0.2 $^{+1.4}_{-0.1}$	0.20 $^{+2.77}_{-0.19}$	17.8/9
516	14.7 $^{+4.3}_{-0.8}$	2.1 $^{+0.7}_{-1.2}$	0.27 $^{+0.59}_{-0.13}$	5.4/9
524	18.0 $^{+0.2}_{-1.4}$	2.4 $^{+0.8}_{-0.4}$	2.14 $^{+0.74}_{-0.88}$	17.1/9
525	13.7 $^{+2.3}_{-0.7}$	4.1 $^{+0.9}_{-1.6}$	0.48 $^{+0.52}_{-0.20}$	8.0/9
526	14.1 $^{+0.9}_{-2.6}$	2.1 $^{+2.4}_{-0.5}$	0.18 $^{+0.16}_{-0.13}$	9.8/9
533	8.4 $^{+20.3}_{-1.3}$	<19.4	<1.41	2.8/4
547	14.9 $^{+2.6}_{-4.8}$	1.6 $^{+4.6}_{-0.8}$	0.17 $^{+0.32}_{-0.16}$	8.2/9
557	17.4 $^{+14.5}_{-8.7}$	<8.3	<1.41	2.2/4
562	16.9 $^{+2.4}_{-3.6}$	0.8 $^{+1.2}_{-0.3}$	0.14 $^{+0.26}_{-0.11}$	11.4/9
576	13.7 $^{+2.1}_{-3.4}$	2.0 $^{+3.5}_{-1.1}$	<0.30	5.4/9
578	22.8 $^{+2.1}_{-5.5}$	0.4 $^{+0.7}_{-0.1}$	0.33 $^{+0.65}_{-0.24}$	18.0/9

¹: BB radius assuming a distance 4 kpc. Uncertainty of absolute flux in the response matrix of 30% is included.

²: Soft gamma-ray flux in the range of the 160 keV–6.2 MeV. Uncertainty of absolute flux in the reponse matrix of 30% is included.

³: d.o.f: degree of freedom.

Table C.2: Spectral parameters of acceptable OTTB fitting

ID	kT (keV)	F ($\times 10^{-6}$ erg cm $^{-2}$ s $^{-1}$) ¹	χ^2 /d.o.f ²
45	60.0 $^{+15.2}_{-46.7}$	<0.62	1.3/4
59	44.5 $^{+17.2}_{-24.8}$	<0.57	4.3/4
63	44.9 $^{+2.5}_{-10.4}$	0.16 $^{+0.16}_{-0.10}$	12.4/9
72	43.8 $^{+2.9}_{-5.5}$	1.37 $^{+0.56}_{-0.57}$	17.4/9
81	39.9 $^{+1.1}_{-6.1}$	0.16 $^{+0.11}_{-0.08}$	11.9/9
83	42.7 $^{+35.6}_{-5.2}$	0.27 $^{+0.56}_{-0.13}$	6.5/9
84	36.8 $^{+14.3}_{-5.0}$	0.65 $^{+0.57}_{-0.33}$	12.3/9
88	55.7 $^{+6.6}_{-4.8}$	2.68 $^{+1.06}_{-0.97}$	9.3/9
113	43.9 $^{+3.9}_{-9.0}$	1.76 $^{+0.85}_{-0.94}$	12.9/9
144	48.5 $^{+5.5}_{-29.2}$	<0.26	2.4/4
154	40.5 $^{+10.9}_{-8.5}$	0.22 $^{+0.29}_{-0.14}$	10.7/9
155	29.8 $^{+14.4}_{-17.7}$	< 0.49	2.7/9
157	49.5 $^{+7.8}_{-6.7}$	0.21 $^{+0.16}_{-0.13}$	4.1/9
166	50.7 $^{+76.3}_{-28.8}$	<1.06	1.9/4
168	29.9 $^{+13.5}_{-26.6}$	0.07 $^{+0.13}_{-0.05}$	5.2/4
181	32.4 $^{+13.4}_{-12.5}$	0.12 $^{+0.18}_{-0.11}$	3.9/4
182	42.0 $^{+49.5}_{-22.3}$	<0.74	10.6/4
205	50.5 $^{+18.5}_{-10.1}$	0.13 $^{+0.47}_{-0.06}$	7.1/9
210	41.2 $^{+14.6}_{-14.2}$	<0.54	3.4/4
212	38.7 $^{+20.8}_{-12.3}$	<0.56	0.6/4
233	60.2 $^{+1.7}_{-3.7}$	0.66 $^{+0.45}_{-0.22}$	10.9/9
234	61.8 $^{+4.7}_{-16.2}$	0.42 $^{+0.44}_{-0.26}$	6.2/9
235	47.9 $^{+7.7}_{-45.3}$	<0.62	2.3/4
242	42.9 $^{+4.8}_{-19.8}$	0.35 $^{+0.42}_{-0.33}$	7.6/9
243	42.0 $^{+18.2}_{-8.6}$	1.14 $^{+1.42}_{-0.62}$	10.0/9
244	40.9 $^{+2.7}_{-12.9}$	0.65 $^{+0.33}_{-0.48}$	10.8/9
257	35.3 $^{+9.3}_{-23.4}$	<0.48	1.4/4

ID	kT (keV)	F ($\times 10^{-6}$ erg cm $^{-2}$ s $^{-1}$) ¹	$\chi^2/\text{d.o.f}^2$
270	37.2 ^{+4.4} _{-8.6}	0.58 ^{+0.41} _{-0.38}	9.3/9
280	44.9 ^{+9.0} _{-6.8}	1.55 ^{+0.94} _{-0.83}	12.3/9
282	40.3 ^{+14.5} _{-2.6}	0.21 ^{+0.33} _{-0.16}	3.9/9
284	54.0 ^{+10.3} _{-11.6}	2.09 ^{+1.53} _{-1.04}	4.9/9
292	38.9 ^{+6.9} _{-33.7}	< 0.51	6.6/9
296	19.4 ^{+12.5} _{-1.0}	0.04 ^{+0.19} _{-0.02}	12.4/9
298	31.9 ^{+8.2} _{-5.6}	0.59 ^{+0.52} _{-0.32}	8.2/9
299	36.7 ^{+18.6} _{-12.0}	0.55 ^{+1.06} _{-0.43}	12.2/9
312	49.2 ^{+6.7} _{-4.3}	0.67 ^{+0.34} _{-0.34}	13.2/9
313	37.9 ^{+9.8} _{-2.1}	0.52 ^{+0.39} _{-0.26}	9.5/9
317	43.9 ^{+21.2} _{-7.2}	0.68 ^{+0.82} _{-0.43}	4.0/9
320	71.6 ^{+3.5} _{-14.0}	2.14 ^{+0.95} _{-0.95}	3.4/9
347	41.0 ^{+32.9} _{-3.4}	0.24 ^{+0.61} _{-0.22}	3.3/9
348	36.9 ^{+15.0} _{-5.2}	0.11 ^{+0.22} _{-0.06}	11.8/9
349	42.8 ^{+3.2} _{-20.1}	0.09 ^{+0.14} _{-0.08}	6.5/4
352	50.6 ^{+20.8} _{-1.8}	1.15 ^{+0.99} _{-0.52}	2.9/9
374	11.2 ^{+23.6} _{-2.9}	<0.26	2.6/4
381	47.2 ^{+9.3} _{-35.1}	<0.58	7.8/4
387	45.0 ^{+4.2} _{-14.6}	0.92 ^{+0.53} _{-0.65}	10.4/9
388	39.6 ^{+40.1} _{-18.7}	0.20 ^{+0.77} _{-0.19}	6.4/9
395	26.5 ^{+37.7} _{-12.0}	<0.98	1.5/4
403	33.4 ^{+7.9} _{-9.3}	0.48 ^{+0.44} _{-0.35}	16.1/9
411	40.7 ^{+8.0} _{-4.1}	1.67 ^{+1.03} _{-0.74}	7.3/9
413	44.9 ^{+3.0} _{-18.3}	0.48 ^{+0.37} _{-0.38}	5.4/9
418	38.6 ^{+4.8} _{-4.1}	0.55 ^{+0.29} _{-0.25}	3.7/9
422	25.3 ^{+2.2} _{-0.3}	0.18 ^{+0.08} _{-0.06}	18.5/9
425	55.3 ^{+1.4} _{-5.6}	2.69 ^{+1.00} _{-0.96}	16.3/9
428	24.2 ^{+12.6} _{-5.6}	<0.25	7.2/9
435	45.5 ^{+4.3} _{-32.7}	<0.73	3.1/4
440	26.9 ^{+4.4} _{-14.0}	<0.26	2.8/9
443	28.6 ^{+13.1} _{-7.5}	0.11 ^{+0.21} _{-0.10}	6.5/9

ID	kT (keV)	F ($\times 10^{-6}$ erg cm $^{-2}$ s $^{-1}$) ¹	$\chi^2/\text{d.o.f.}$ ²
448	26.4 ^{+10.0} _{-1.4}	0.15 ^{+0.23} _{-0.06}	7.1/9
476	39.8 ^{+6.2} _{-14.3}	0.17 ^{+0.18} _{-0.14}	5.2/9
485	63.9 ^{+3.9} _{-1.7}	10.10 ^{+3.28} _{-3.16}	51.6/9
488	36.3 ^{+3.7} _{-11.2}	0.56 ^{+0.26} _{-0.41}	10.3/9
490	27.9 ^{+9.6} _{-1.7}	0.21 ^{+0.35} _{-0.15}	14.4/9
491	30.1 ^{+2.5} _{-24.7}	< 0.49	14.9/9
498	43.2 ^{+3.5} _{-4.2}	0.94 ^{+0.43} _{-0.38}	13.7/9
500	28.5 ^{+11.8} _{-10.3}	<0.18	1.6/4
502	57.5 ^{+44.1} _{-29.0}	<0.66	3.1/4
508	38.5 ^{+4.5} _{-10.3}	0.67 ^{+0.45} _{-0.49}	8.3/9
512	113.8 ^{+9.1} _{-91.2}	<1.03	15.1/9
516	36.0 ^{+7.7} _{-2.3}	0.31 ^{+0.25} _{-0.12}	5.5/9
519	55.2 ^{+4.4} _{-19.1}	2.21 ^{+1.27} _{-1.48}	14.2/9
524	48.9 ^{+2.0} _{-10.3}	2.52 ^{+1.01} _{-1.27}	36.3/9
525	33.8 ^{+11.8} _{-2.2}	0.71 ^{+0.77} _{-0.32}	6.7/9
526	35.8 ^{+1.5} _{-8.7}	0.24 ^{+0.20} _{-0.15}	8.4/9
533	42.0 ^{+52.8} _{-27.8}	<0.59	2.6/4
547	39.3 ^{+1.9} _{-8.7}	0.23 ^{+0.12} _{-0.14}	8.0/9
557	48.1 ^{+34.8} _{-33.6}	<0.87	2.0/4
562	50.2 ^{+6.0} _{-14.2}	0.19 ^{+0.27} _{-0.13}	10.0/9
576	30.4 ^{+10.6} _{-3.8}	0.15 ^{+0.22} _{-0.10}	5.5/9
578	99.3 ^{+11.6} _{-9.1}	0.4 ^{+0.19} _{-0.14}	10.6/9

¹: Soft gamma-ray flux in the range of the 160 keV–6.2 MeV. Uncertainty of absolute flux in the reponse matrix of 30% is included.

²: d.o.f: degree of freedom.

Table C.3: Spectral parameters of acceptable PL fitting

ID	Photon index	F ($\times 10^{-6}$ erg cm $^{-2}$ s $^{-1}$) ¹	$\chi^2/\text{d.o.f.}$ ²
45	3.4 ^{+3.4} _{-2.5}	<4.95	1.2/4
59	3.6 ^{+1.7} _{-0.9}	0.18 ^{+0.78} _{-0.17}	4.9/4
63	3.6 \pm 0.5	0.19 ^{+0.50} _{-0.13}	11.6/9
81	3.7 ^{+0.6} _{-0.8}	0.27 ^{+0.79} _{-0.19}	12.4/9

ID	Photon index	F ($\times 10^{-6} \text{erg cm}^{-2} \text{s}^{-1}$) ¹	$\chi^2/\text{d.o.f}^2$
83	3.4 ± 0.3	0.49 $^{+0.45}_{-0.30}$	9.6/9
88	4.3 $^{+0.1}_{-0.2}$	1.69 $^{+0.70}_{-0.60}$	15.2/9
144	3.7 $^{+2.0}_{-0.6}$	<0.92	3.3/4
154	3.4 $^{+0.5}_{-0.3}$	0.38 $^{+0.53}_{-0.26}$	9.7/9
155	4.6 $^{+0.8}_{-0.9}$	0.18 $^{+0.43}_{-0.16}$	2.9/9
157	3.4 ± 0.8	0.28 $^{+1.34}_{-0.22}$	5.2/9
166	3.3 $^{+2.9}_{-0.6}$	<1.26	3.3/4
168	5.4 $^{+1.2}_{-1.3}$	<0.57	4.0/4
181	<1.2	<10.50	4.4/4
182	3.2 $^{+0.4}_{-6.7}$	0.27 $^{+4.84}_{-0.21}$	6.0/4
205	3.3 $^{+0.5}_{-0.3}$	0.22 $^{+0.60}_{-0.13}$	8.3/9
210	6.1 $^{+1.0}_{-5.2}$	<3.55	4.2/4
212	3.8 $^{+3.2}_{-0.8}$	<2.15	1.5/4
233	3.5 $^{+1.3}_{-0.2}$	0.99 $^{+0.55}_{-0.84}$	15.7/9
234	4.7 $^{+0.1}_{-0.6}$	0.29 $^{+0.34}_{-0.14}$	14.6/9
235	3.6 $^{+1.9}_{-0.9}$	<1.64	2.1/4
242	3.9 $^{+1.4}_{-0.4}$	0.54 $^{+0.57}_{-0.48}$	11.0/9
244	3.7 ± 0.2	1.1 $^{+0.67}_{-0.49}$	13.0/9
257	<3.2	<0.82	1.4/4
270	4.0 $^{+0.3}_{-0.2}$	0.94 $^{+0.42}_{-0.43}$	19.5/9
280	4.4 $^{+0.7}_{-0.6}$	1.03 $^{+1.21}_{-0.74}$	14.4/9
282	3.7 ± 0.4	0.33 $^{+0.59}_{-0.22}$	9.1/9
288	3.8 ± 0.1	5.02 $^{+1.86}_{-1.60}$	8.2/9
292	3.7 $^{+0.4}_{-0.5}$	0.45 $^{+0.53}_{-0.28}$	5.3/9
296	5.6 $^{+0.2}_{-1.1}$	0.05 $^{+0.22}_{-0.02}$	13.1/9
298	4.9 $^{+0.2}_{-0.5}$	0.41 $^{+0.44}_{-0.18}$	8.2/9
313	3.8 $^{+0.9}_{-0.3}$	0.96 ± 0.7	6.2/9
317	4.1 $^{+0.8}_{-0.4}$	0.74 $^{+0.80}_{-0.52}$	4.2/9
320	3.7 ± 0.1	2.19 $^{+0.85}_{-0.71}$	9.4/9
347	3.7 $^{+0.2}_{-0.5}$	0.43 $^{+0.50}_{-0.25}$	9.3/9
348	3.7 ± 0.4	0.18 $^{+0.27}_{-0.11}$	13.6/9

ID	Photon index	F ($\times 10^{-6}$ erg cm $^{-2}$ s $^{-1}$) 1	$\chi^2/\text{d.o.f}^2$
349	<2.8	<0.66	7.3/4
374	5.6 $^{+1.2}_{-1.9}$	<0.49	2.2/4
381	3.5 $^{+1.4}_{-1.3}$	<1.04	4.3/4
387	3.9 $^{+0.1}_{-0.2}$	1.14 $^{+0.50}_{-0.41}$	15.3/9
388	4.6 $^{+2.1}_{-1.4}$	< 1.13	6.2/9
393	4.0 $^{+0.4}_{-0.1}$	2.02 $^{+0.72}_{-0.96}$	10.9/9
395	5.5 $^{+3.3}_{-1.1}$	<0.24	1.9/4
403	3.9 $^{+0.3}_{-0.2}$	0.92 $^{+0.42}_{-0.41}$	17.2/9
408	3.0 $^{+0.6}_{-0.2}$	<0.52	7.6/9
413	4.0 $^{+0.2}_{-0.4}$	0.66 $^{+0.46}_{-0.35}$	14.1/9
418	3.9 $^{+0.2}_{-0.3}$	0.88 $^{+0.46}_{-0.39}$	7.6/9
422	4.2 $^{+0.1}_{-0.2}$	0.43 $^{+0.17}_{-0.18}$	15.8/9
425	3.9 ± 0.1	2.93 $^{+0.97}_{-0.92}$	17.5/9
428	4.2 $^{+0.5}_{-1.3}$	0.19 $^{+0.95}_{-0.13}$	7.2/9
435	3.6 $^{+1.1}_{-1.9}$	0.26 $^{+2.40}_{-0.22}$	1.7/4
440	4.1 $^{+0.5}_{-0.2}$	0.37 $^{+0.26}_{-0.22}$	3.4/9
443	4.3 $^{+0.3}_{-1.2}$	0.20 $^{+0.65}_{-0.16}$	8.4/9
448	4.2 $^{+0.6}_{-0.3}$	0.37 $^{+0.25}_{-0.23}$	6.9/9
476	3.7 $^{+0.9}_{-0.4}$	0.28 $^{+0.58}_{-0.22}$	9.3/9
485	3.6 ± 0.1	10.50 $^{+3.46}_{-3.58}$	14.4/9
488	4.3 $^{+0.1}_{-0.4}$	0.68 $^{+0.48}_{-0.24}$	8.6/9
490	4.1 $^{+0.6}_{-0.4}$	0.48 $^{+0.54}_{-0.37}$	13.4/9
491	4.1 $^{+0.5}_{-1.3}$	0.71 $^{+2.75}_{-0.41}$	9.4/9
498	3.8 ± 0.1	1.39 $^{+0.52}_{-0.51}$	34.4/9
500	6.2 $^{+0.7}_{-4.8}$	<3.10	0.6/4
502	3.3 $^{+1.9}_{-0.6}$	<0.95	3.6/4
508	4.2 ± 0.2	0.85 $^{+0.38}_{-0.34}$	14.5/9
512	3.7 $^{+3.0}_{-1.0}$	< 1.65	18.3/9
516	3.8 $^{+0.5}_{-0.8}$	0.54 $^{+1.74}_{-0.33}$	10.6/9
526	3.8 $^{+0.4}_{-0.3}$	0.38 $^{+0.45}_{-0.22}$	9.5/9
533	3.2 $^{+2.4}_{-0.3}$	<0.79	1.6/4

ID	Photon index	F ($\times 10^{-6}$ erg cm $^{-2}$ s $^{-1}$) ¹	χ^2 /d.o.f ²
547	3.6 ^{+1.4} _{-0.3}	0.41 ^{+0.5} _{-0.37}	9.6/9
557	3.2 ^{+3.4} _{-0.7}	<0.82	2.4/4
562	3.4 ^{+0.5} _{-0.9}	0.32 ^{+1.12} _{-0.21}	7.9/9
576	4.1 ^{+0.4} _{-0.4}	0.31 ^{+0.34} _{-0.18}	4.7/9
578	2.7 ^{+0.3} _{-0.2}	0.73 ^{+0.34} _{-0.35}	11.6/9

¹: Soft gamma-ray flux in the range of the 160 keV–6.2 MeV. Uncertainty of absolute flux in the reponse matrix of 30% is included.

¹: d.o.f: degree of freedom.

Table C.4: Spectral parameters of acceptable BBBB fitting

ID	kT_{BB} (keV)	R_{BB} ¹ (km)	kT_{BBhigh} (keV)	R_{BBhigh} ¹ (km)	F ($\times 10^{-6}$ erg cm $^{-2}$ s $^{-1}$) ²	χ^2 /d.o.f ³
287	13.6 ^{+1.9} _{-1.6}	1.7 ^{+1.3} _{-0.6}	75.2 ^{+4.2} _{-3.7}	0.05 \pm 0.01	3.66 ^{+1.57} _{-1.21}	56.5/27
321	9.7 ^{+2.7} _{-0.7}	14.0 ^{+5.7} _{-8.3}	32.2 ^{+1.4} _{-2.2}	0.41 ^{+0.13} _{-0.07}	4.06 ^{+2.05} _{-1.37}	52.2/27
520	18.2 ^{+0.8} _{-6.5}	3.2 ^{+9.0} _{-0.8}	21.4 ^{+1.0} _{-2.3}	1.68 ^{+1.11} _{-0.31}	8.22 ^{+5.83} _{-5.59}	34.3/17
521	16.2 ^{+1.1} _{-5.5}	3.2 ^{+7.3} _{-0.9}	27.2 ^{+0.4} _{-3.1}	0.68 ^{+0.44} _{-0.10}	5.17 ^{+3.05} _{-2.78}	41.8/19

¹: BB radius assuming a distance 4 kpc. Uncertainty of absolute flux in the reponse matrix of 30% is included.

²: Soft gamma-ray flux in the range of the 160 keV–6.2 MeV. Uncertainty of absolute flux in the reponse matrix of 30% is included.

³: d.o.f: degree of freedom.

Table C.5: Spectral parameters of acceptable BBOTTB fitting

ID	kT_{BB} (keV)	R_{BB} ¹ (km)	kT_{OTTB} (keV)	F ($\times 10^{-6}$ erg cm $^{-2}$ s $^{-1}$) ²	χ^2 /d.o.f ³
167	15.5 ^{+1.6} _{-2.1}	3.1 ^{+1.7} _{-0.9}	58.1 ^{+5.7} _{-4.8}	2.60 ^{+1.03} _{-0.97}	51.8/27
321	14.3 ^{+1.6} _{-2.7}	3.6 ^{+3.7} _{-1.4}	74.8 ^{+7.0} _{-3.5}	2.31 ^{+0.99} _{-0.88}	44.6/27
392	17.7 ^{+1.1} _{-0.7}	2.9 ^{+0.9} _{-0.7}	109.6 ^{+4.1} _{-38.2}	3.76 ^{+2.29} _{-1.36}	51.4/27
412	17.1 \pm 0.7	2.7 ^{+0.7} _{-0.6}	80.1 ^{+6.0} _{-5.4}	3.11 ^{+1.40} _{-1.21}	53.9/27
424	18.9 ^{+3.8} _{-7.4}	3.4 ^{+2.9} _{-2.1}	346.1 ^{+36.2} _{-27.1}	9.38 ^{+9.58} _{-6.48}	79.2/46
520	15.6 ^{+1.2} _{-0.5}	4.8 ^{+1.0} _{-1.5}	51.8 ^{+4.7} _{-8.4}	5.96 ^{+3.00} _{-2.16}	30.9/17
521	15.4 ^{+2.2} _{-0.8}	4.3 ^{+1.0} _{-1.7}	75.8 ^{+3.9} _{-9.5}	2.90 ^{+1.63} _{-1.18}	40.2/19

ID	kT_{BB} (keV)	R_{BB}^1 (km)	kT_{OTTB} (keV)	F ($\times 10^{-6}$ erg cm $^{-2}$ s $^{-1}$) 2	$\chi^2/\text{d.o.f}^3$
522	15.6 $^{+1.8}_{-1.9}$	3.8 $^{+1.8}_{-1.2}$	42.1 $^{+2.6}_{-6.3}$	3.85 $^{+2.24}_{-1.53}$	14.0/7

¹: BB radius assuming a distance 4 kpc. Uncertainty of absolute flux in the reponse matrix of 30% is included.

²: Soft gamma-ray flux in the range of the 160 keV–6.2 MeV. Uncertainty of absolute flux in the reponse matrix of 30% is included.

³: d.o.f: degree of freedom.

Table C.6: Spectral parameters of acceptable BBPL fitting

ID	kT_{BB} (keV)	R_{BB}^1 (km)	Photon index	F ($\times 10^{-6}$ erg cm $^{-2}$ s $^{-1}$) 2	$\chi^2/\text{d.o.f}^3$
167	16.0 $^{+3.0}_{-1.3}$	3.2 $^{+1.1}_{-1.4}$	3.7 $^{+0.7}_{-0.2}$	2.77 $^{+2.82}_{-1.57}$	50.2/27
321	22.0 $^{+1.5}_{-2.0}$	1.1 $^{+0.5}_{-0.3}$	3.8 $^{+0.3}_{-0.2}$	4.40 $^{+3.03}_{-2.19}$	58.9/27
520	17.7 $^{+2.8}_{-0.6}$	3.8 $^{+0.7}_{-1.5}$	4.1 $^{+0.5}_{-0.1}$	6.24 $^{+4.77}_{-2.95}$	25.2/17

¹: BB radius assuming a distance 4 kpc. Uncertainty of absolute flux in the reponse matrix of 30% is included.

²: Soft gamma-ray flux in the range of the 160 keV–6.2 MeV. Uncertainty of absolute flux in the reponse matrix of 30% is included.

³: d.o.f: degree of freedom.

Table C.7: Spectral parameters of acceptable BBPLE fitting

ID	kT_{BB} (keV)	R_{BB}^1 (km)	Photon index	E_{cut} (keV)	F ($\times 10^{-6}$ erg cm $^{-2}$ s $^{-1}$) 2	$\chi^2/\text{d.o.f}^3$
167	17.1 $^{+1.0}_{-1.3}$	3.0 $^{+1.2}_{-0.7}$	2.3 $^{+0.3}_{-0.2}$	409 $^{+294}_{-256}$	3.54 $^{+2.24}_{-2.19}$	46.1/26
321	16.6 $^{+3.5}_{-0.3}$	2.8 $^{+0.5}_{-1.4}$	1.8 $^{+0.3}_{-0.2}$	128 $^{+18}_{-40}$	3.68 $^{+3.32}_{-1.95}$	55.1/26
392	19.2 $^{+1.9}_{-0.3}$	1.4 \pm 0.3	1.0 \pm 0.1	61 $^{+76}_{-60}$	>0.78	56.5/26
424	19.7 $^{+0.8}_{-7.4}$	3.3 $^{+2.9}_{-2.2}$	0.9 \pm 0.4	270 $^{+88}_{-65}$	24.3 $^{+23.6}_{-14.9}$	83.9/45
492	17.5 $^{+1.1}_{-1.7}$	4.1 $^{+1.5}_{-0.9}$	0.8 $^{+0.1}_{-0.2}$	176 $^{+51}_{-35}$	21.6 $^{+9.6}_{-9.0}$	69.6/36
520	16.0 $^{+1.6}_{-0.8}$	5.5 $^{+1.1}_{-1.7}$	2.6 $^{+0.9}_{-0.1}$	134 $^{+49}_{-21}$	5.44 $^{+4.51}_{-2.91}$	28.8/16
521	17.6 $^{+0.9}_{-1.3}$	3.0 $^{+1.1}_{-0.7}$	2.4 $^{+0.3}_{-1.1}$	165 $^{+207}_{-54}$	4.48 $^{+6.81}_{-2.7}$	34.2/18
523	15.7 $^{+1.0}_{-1.3}$	3.4 $^{+1.2}_{-0.9}$	1.9 $^{+0.6}_{-0.5}$	136 $^{+18}_{-36}$	2.64 $^{+2.07}_{-1.63}$	27.0/14

¹: BB radius assuming a distance 4 kpc. Uncertainty of absolute flux in the reponse matrix of 30% is included.

²: Soft gamma-ray flux in the range of the 160 keV–6.2 MeV. Uncertainty of absolute flux in the response matrix of 30% is included.

³: d.o.f: degree of freedom.

Acknowledgements

First of all, I would like to express my gratitude to my supervisor associate professor Yukikatsu Terada. I also have had the support and guidance of Prof. Makoto S. Tashiro. These advices on research have been invaluable. Above all, they invited me to wonderful X-ray astronomy. They said to me “Are you interested in magnetars?” which boot my all works five years ago.

I would like to express the appreciation to Dr. Teruaki Enoto, Dr. Yujin E. Nakagawa, and associate professor Aya Bamba. They showed me an interest in my works, and that motivates me to research into AXP 1E 1547.0–5408. The techniques of data analysis of *Swift* were obtained by joint research about classical GRB with Dr. Yuji Urata in Taiwan. The author has benefited from member of the *Suzaku* WAM team. Dr. Kazutaka Yamaoka and Dr. Masanori Ohno provided detailed information of the WAM, and it is important to develop the pile-up simulator and perform spectral analysis. Without their supports and advices, I could not complete this thesis.

I want to thank my colleague Koyama-kun. I think that he is the best comrade and rival, and discussions with him were a lot of fun. I was happy to study with him in our group for five years. I also thank all my colleagues, especially older members Akira-san, Onda-san, Seta-san, Iwakiri-san, Harayama-san, Kouzu-san, Shimoda-san, and the others. They gave me enormous advises and guidance not only in the research but also in my life. In addition, the author had a great time at Saitama University with many fine classmates.

Finally, I would like to show my greatest appreciation to my families for supporting and understanding me.

Tetsuya Yasuda
Saitama University
2015 March

